INFORMATION TO USERS

This manuscript has been reproduced from the microfilm master. UMI films the text directly from the original or copy submitted. Thus, some thesis and dissertation copies are in typewriter face, while others may be from any type of computer printer.

The quality of this reproduction is dependent upon the quality of the copy submitted. Broken or indistinct print, colored or poor quality illustrations and photographs, print bleedthrough, substandard margins, and improper alignment can adversely affect reproduction.

In the unlikely event that the author did not send UMI a complete manuscript and there are missing pages, these will be noted. Also, if unauthorized copyright material had to be removed, a note will indicate the deletion.

Oversize materials (e.g., maps, drawings, charts) are reproduced by sectioning the original, beginning at the upper left-hand corner and continuing from left to right in equal sections with small overlaps. Each original is also photographed in one exposure and is included in reduced form at the back of the book.

Photographs included in the original manuscript have been reproduced xerographically in this copy. Higher quality 6" x 9" black and white photographic prints are available for any photographs or illustrations appearing in this copy for an additional charge. Contact UMI directly to order.

UMI

A Bell & Howell Information Company
300 North Zeeb Road, Ann Arbor MI 48106-1346 USA
313/761-4700 800/521-0600

The Perturbative and Non-Perturbative QCD Effects in the Azimuthal Distribution of Hadron Jets Observed in Muon Deep Inelastic Scattering

by

Zhong Jin

A dissertation submitted in partial fulfillment
of the requirements for the degree of

Doctor of Philosophy

University of Washington

1997

Approved by _____
(Chairperson of Supervisory Committee)

_____

_____

Program Authorized
to Offer Degree Physics

Date June 13, 1997

In presenting this dissertation in partial fulfillment of the requirements for the Doctoral degree at the University of Washington, I agree that the Library shall make its copies freely available for inspection. I further agree that extensive copying of this dissertation is allowable only for scholarly purposes, consistent with "fair use" as prescribed in the U.S. Copyright Law. Requests for copying or reproduction of this dissertation may be referred to University Microfilms, 1490 Eisenhower Place, P.O. Box 975, Ann Arbor, MI 48106, to whom the author has granted "the right to reproduce and sell (a) copies of the manuscript in microform and/or (b) printed copies of the manuscript made from microform."

Signature 

Date June 11. 1997

University of Washington

Abstract

The Perturbative and Non-Perturbative QCD Effects in the Azimuthal Distribution of Hadron Jets Observed in Muon Deep Inelastic Scattering

by Zhong Jin

Chairperson of Supervisory Committee: *Professor Henry J. Lubatti*
Department of Physics

Azimuthal asymmetry of hadron jets produced in deep inelastic muon scattering is studied for the first time. The data were collected at the experiment E665 at Fermilab during 1991-1992 using liquid hydrogen and deuterium targets. The muon beam had a mean energy of 500 GeV. A detailed study of various popular algorithms for identifying jets within an event leads us to choose the modified JADE algorithm and the Ellis-Soper algorithm for the energy range of this experiment. A total of 148639 events with $Q^2 > 3\,GeV^2$ and $W^2 > 25\,GeV^2$ are used in this analysis. Using the identified 2-jet events we studied the azimuthal distributions of the jets in the center of mass frame of the target and virtual photon. Comparison with the perturbative QCD prediction is made.

TABLE OF CONTENTS

LIST OF FIGURES

LIST OF TABLES

ACKNOWLEDGEMENTS

I have enjoyed my six years as Prof. Henry Lubatti's graduate student in the Visual Technique Lab (VTL) at the University of Washington. I am especially grateful to him for giving me the opportunity to participate in the E665 experiment at Fermi lab and for the freedom he gave me to pursue my research interests. I would also like to thank him for his patience, advise, and encouragement.

As the last member of E665, I would like to thank all of the E665 participants for answering my questions and helping me out in the lab: Guang Fang, Janet Conrad, Ashutosh Kotwal, Harry Melanson, Steve Wolbers, Carlos salgado, Pangiotis Spentzouris, Guo and Harsh Venkataramania. My special thanks go to Tim Carroll, who for three years was so patiently and thoroughly answering my endless questions and to our spokesperson Heidi Schellman for her useful suggestions. I also want to thank these senior physicists: W. Witteck, D. Geesaman, R. Wilson and N. Schmitz for their helpful advise.

Thanks to Tianchi Zhao who proof-read the whole thesis and was always available to help. I also enjoyed his Thanksgiving parties and his wife's cooking. My former colleagues and friends at Seattle: William Dougherty, Uwe Bratzler and Lian He, Chengxing Zhai and Yan Zhang were also very helpful. Roger Lord's constant reminder: "have you finished your thesis yet?" - motivated me a great deal. VTL's other professors and members, J. Wilkes, J. Lord, R. Davisson, C. Daly, H. Berns, Linda and Nicole were always very kind and make me feel home during all these years. I also very much appreciate the interesting discussions with Steve Ellis on jet algorithms and azimuthal asymmetry and the email discussions on jet selection with Hermann Hessling from DESY. Finally I would like to thank Anatole Sagal for his encouragement and his statistics expertise.

DEDICATION

For my parents who lead me to physics,

Jianxing and Yuanwang Jin.

Chapter 1

INTRODUCTION

1.1 Deep Inelastic Scattering

A very powerful way of experimentally investigating the strongly interacting particles (hadrons) is to probe them with high energy leptons. The interactions between leptons and hadrons are mediated by virtual photons which have completely known properties. This permits a fine control of variables, and decreases the theoretical complexity of the interactions. Deep Inelastic Scattering (DIS) is such a method and has been proved to be very effective in investigating the structure of the nucleus, and even the nucleon.

The lepton-nucleus scattering experiment is shown schematically in Figure 1.1. A lepton with four-momentum $k = (E, \vec{k})$ scatters off the nucleus and emerges at an angle θ with momentum $k' = (E', \vec{k'})$.

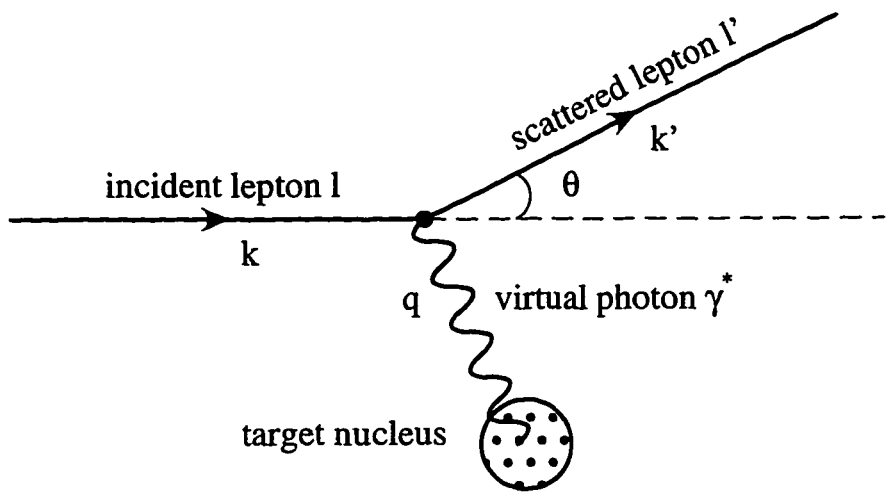

Figure 1.1: Schematic view of lepton nucleus scattering.

The effective probe of the structure within the nucleus is the exchanged virtual photon with momentum $q = k - k'$ and $q^2 = -Q^2$ where $Q^2 > 0$. The resolving power of this probe is the "wavelength" $\hbar/Q$ and so the degree of structure revealed increases with Q^2. The energy of the virtual photon is $\nu = E - E'$ in the lab frame. For low values of Q^2 ($\sim 0.01\,GeV^2$) the nucleus recoils as a whole with $\nu = \nu_{el} = Q^2/2M_A$ where M_A is the nuclear mass, and can move into an excited state with $\nu = \nu_{el} + (M_{A^*}^2 - M_A^2)/2M_A$. If we use the variable $x = Q^2/2M_A\nu$, elastic scattering corresponds to $x = 1$. As Q^2 increases, the elastic cross-section decreases. When Q^2 reaches about $0.1\,GeV^2$, the photon is scattering off the constituent nucleons with $\nu = Q^2/2M$. Here M is the nucleon mass. x is now redefined as $x = Q^2/2M\nu$. As Q^2 increases more, the structure of the nucleon is being probed. This is the region called deep inelastic scattering (DIS). If we interpret a nucleon (for example proton) as consisting of three point-like quarks (uud), we might expect that this quark structure would produce peaks around $x = \frac{1}{3}$ because x is approximately the momentum fraction of each constituent. In practice, we see a smooth continuum rising toward $x = 0$ as Q^2 increases, which we attribute to sea quarks or gluons.

By studying the behavior of the outgoing particles resulting from the nucleon breakup, information about the structure of the nucleon can be extracted.

The electromagnetic coupling between the photon and the lepton (α_{EM}) is small according to the well understood Quantum ElectroDynamics (QED). In other words, perturbative techniques of QED can be applied and the radiative corrections to the Born diagram can be calculated to a satisfying precision. Using the single photon exchange approximation allows the diagram to be factorized into the leptonic part and the hadronic part as in Figure 1.2. Thus one can study in general the hadron vertex while the probing energy Q^2 can be determined by the scattering angle θ and the energy E'.

This thesis deals with the single photon exchange approximation unless otherwise indicated. The definitions of the commonly used kinematic variables in DIS are given

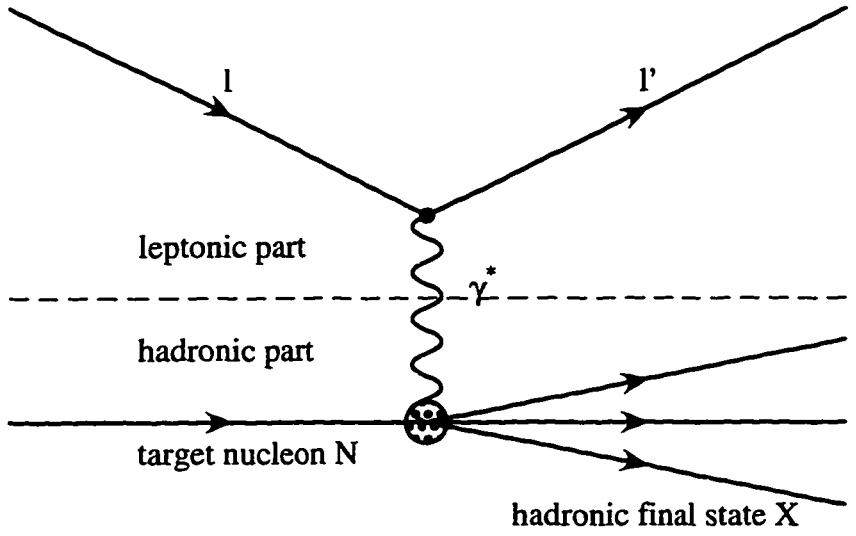

Figure 1.2: The Feynman diagram for one photon exchange DIS event $l + N \rightarrow l' + X$

below:

$$\begin{aligned} Q^2 &= -q^2 = -(k-k')^2 > 0, \\ s &= (P+k)^2, \\ W^2 &= P_X^2, \\ \nu &= (P\cdot q)/M = (W^2+Q^2-M^2)/2M \xrightarrow{\text{lab}} E - E', \\ x &= Q^2/(2p\cdot q) = Q^2/2M\nu, \\ y &= (P\cdot q)/(P\cdot k) \xrightarrow{\text{lab}} \nu/E. \end{aligned} \tag{1.1}$$

Target nucleon has momentum P. P_X is the momentum of the hadronic system X. Here we neglect the mass of the leptons.

1.2 Muon Source

The first muon inelastic scattering experiment was carried out at the Brookhaven National Laboratory (BNL March 1969) [1] using carbon as target. The first muon hydrogen inelastic scattering experiment was conducted in the Stanford Linear Accelerator (SLAC November 1969) [2]. Compared to the electron-hadron inelastic scattering, a muon source is favored due to the following reasons:

1) *Small radiative corrections.*

Radiative corrections are the higher order perturbative QED calculations. The real photon emission from the lepton and the leptonic vertex account for the bulk of

all radiative corrections. Large logarithmic terms of the form $(\alpha_{EM}/\pi)ln(Q^2/m^2)$ are typically associated with the radiation of collinear photons. Also, the polarization of the vacuum alters the Coulomb field of a point charge in a region $r \sim 1/m$. Outside this region, the change decreases exponentially [3]. Muons, with a mass of $105.658389 \pm 0.000034\, MeV$[1][5], are 206.768 times as heavy as electrons. This makes the radiative corrections much smaller than that of electrons.

2) *Readily produced.*

Muon beams can be obtained from the decay of charged pions, which can be easily obtained from the interaction of protons extracted from the proton accelerators like the Tevatron at Fermilab. However, high energy electron beams are difficult to produce, due to the synchrotron radiation. Under the circular acceleration or in storage ring, the energy radiated per particle per turn is [4]

$$\Delta E = \frac{4\pi}{3}\frac{e^2\beta^2\gamma^4}{\rho}, \tag{1.2}$$

where ρ is the bending radius, β is the particle velocity and $\gamma = \frac{1}{\sqrt{1-\beta^2}}$. $\beta\gamma = P/m$. For a relativistic electron and muon of the same momentum the energy loss is in the ratio of $(m_e/m_\mu)^4$, or 10^9 times smaller for a muon compared to an electron. Therefore, for electrons linear accelerator is used.[2] SLAC, using a linear accelerator, can only obtain electron beams up to about $50\, GeV$ compared to the average 500 GeV muon beam at Fermilab. Naturally muons became high-energy, charged-lepton probes.

3) *Easy to detect and identify.*

In muon-nucleon DIS experiments, electroweak interactions dominate. In these experiments, muons are identified as the only only particle that can penetrate the iron absorber with enough energy to create signals in the detectors.

The muon lifetime is about $\tau = 2.2 \times 10^{-6}\, sec$. For relativistic muons, this corresponds to a distance of $\beta\gamma c\tau$, about 6.24 Km per GeV, considerably longer than the size of any laboratory. Therefore, we can consider that muons do not decay before they reach our detectors.

---

[1] The mass is known more precisely in u (atomic mass units): $m_\mu = 0.113428913 \pm 0.000000017\, u$. $1\, u = 931.49432 \pm 0.00028\, MeV$, involves the relatively poorly known electronic charge[5].

[2] At LEP, cynchrotron is used to accelerate electrons and positrons. Nevertheless, even with a boost, the highest beam energy that can be achieved is around $93\, GeV$.

1.3 E665 Convention

E665 is a fixed target muon scattering experiment at Fermilab. The average beam energy is 500 GeV. The analysis in this thesis is based on the E665 data which were taken in 1991. We use the standard E665 coordinate system which is right-handed with the X-axis along the norminal beam direction and the vertical Z-axis pointing up. In the center of mass frame of the virtual photon and the target, the X-axis is the direction of the virtual photon. We will be working in the units where the speed of light $c = 1$.

Chapter 2

QCD & AZIMUTHAL ASYMMETRY

2.1 Quark Parton Model

In the late 1960s, a series of deep inelastic scattering experiments were carried out at SLAC using electron scattering off proton and deuterium targets. They found that the q^2 dependence of the deep continuum is considerably weaker than expected [6], which implied that the nucleons are made of hard point-like constituents, or *partons*, and for the first time the variable q^2/ν was used to make "a fairly universal representation".

In the single photon exchange approximation, the inelastic cross-section for unpolarized target can be written down in general as:

$$\frac{d^2\sigma}{d\nu dQ^2} = \frac{4\pi\alpha_{em}^2 E'}{Q^4 E}\left[2W_1(\nu,Q^2)sin^2\frac{\theta}{2} + W_2(\nu,Q^2)cos^2\frac{\theta}{2}\right] \tag{2.1}$$

where $Q^2 = -q^2$, W_1 and W_2 are the structure functions characterize the features of the scattering other than the photon propagator,

In 1969, the famous *scaling* of the structure functions predicted by Bjorken [8] was observed in *ep* scattering [7]. These structure functions W_1 and W_2, which characterize the features of the scattering, were observed to depend only on one scaling variable, $x = Q^2/M\nu$. Bjorken calculated that, for the single photon exchange approximation, in the limit of $\nu, Q^2 \to \infty$ and Q^2/ν fixed,

$$\begin{aligned} MW_1(\nu,Q^2) &\longrightarrow F_1(Q^2/M\nu) \\ \nu W_2(\nu,Q^2) &\longrightarrow F_2(Q^2/M\nu) \end{aligned}$$

In 1969, Feynman [9] proposed the intuitive parton picture to understand Bjorken scaling, which was formalized later. A formal derivation can be found in reference [10] for example.

In the parton model, the proton is regarded as a collection of partons. So deep inelastic scattering is just a incoherent sum of the individual elastic scattering of

virtual photon on the partons. In the impulse approximation, DIS can be described by Figure 2.1, where the partons do not interact with each other. In the high proton

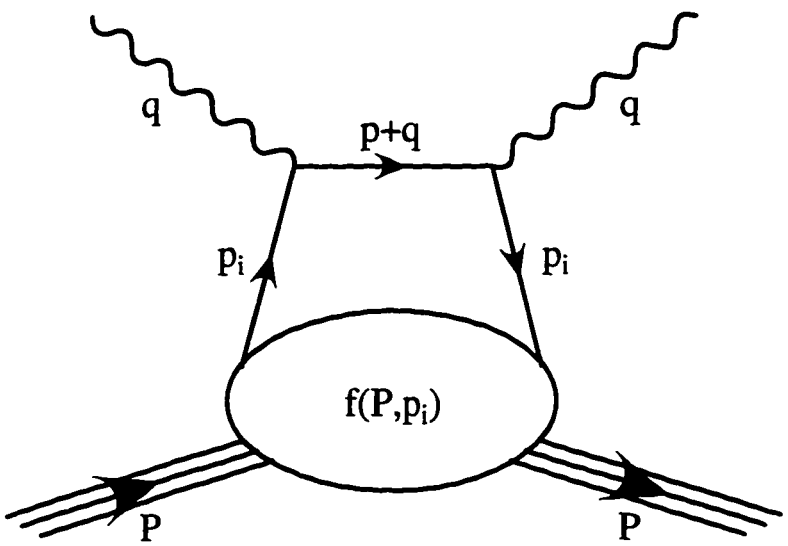

Figure 2.1: The impulse diagram of the Parton Model

momentum limit, the cross-section is proportional to the probability $f_i(x)$ of finding a parton of of type i carrying a fraction x of the momentum of the proton P, or momentum xP.

According to the quark model, all hadrons are made of a small variety of quarks. This led to the hypothesis that quarks were the partons [11]. In the Quark Parton Model, the baryons (mesons) are composed of three (two) valence quarks and a core of an indefinite number of quark-antiquark pairs, and

$$\begin{aligned} F_1(x) &= \sum_i e_i^2 f_i(x), \\ F_2(x) &= \sum_i e_i^2 2x f_i(x), \end{aligned}$$

where e_i is the charge of quark i in unit of e. There are also gluons among the constituents, because the quarks do not account for all of the momentum of the nucleon.

The spin $\frac{1}{2}$ nature of the quarks is reflected in the Callan and Gross relation [12]:

$$F_2(x) = 2xF_1(x)$$

from which it follows that the coupling of the longitudinal part of the quark must vanish. This is consistent with the small values of $R = \sigma_L/\sigma_T \lesssim 0.2$ [13] measured at SLAC.

2.2 Quantum Chromo-Dynamics

The success of the Quark parton model in explaining all "hard" processes, i.e. reactions with large momentum transfer, relies on the assumption of the impulse approximation. Following the new renormalization of gauge fields by G. 't Hooft in 1971 [14], [15] and 1972 [16], Gross and Wilczek [17] and Politzer [18] showed that non-Abelian gauge theories have, up to calculable logarithmic corrections, free-field asymptotic behavior and suggested that Bjorken scaling is obtained from strong-interaction dynamics based on non-Abelian gauge symmetry. As a result, Quantum Chromo-dynamics (QCD) became the accepted quark field theory and the general theory for strong interactions.

The basic idea of QCD is that each flavor of quark appears in any of three colors which generate an SU(3) group; in addition the gauge bosons (gluons) also carry color "charge". So gluons can interact with each other directly. As in Quantum Electro-Dynamics (QED), in the QCD Lagrangian, the effective quark gluon coupling α_s depends on the probing energy Q^2 ("runs"). The fermion loops in the gauge boson propagator have a "screening" effect which reduces the effective strong coupling at large distances. However, the gluon loops have an anti-screening effect. Figure 2.2 shows the one loop correction for both QED and QCD.

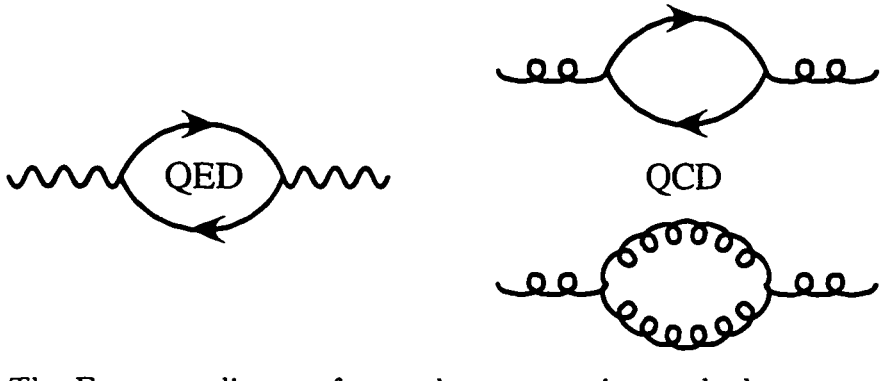

Figure 2.2: The Feynman diagram for one-loop correction to the boson propagator

To leading order the effective coupling is given by

$$\alpha_s(Q^2) = \frac{4\pi}{\beta_0 \ln(Q^2/\Lambda^2)} \tag{2.2}$$

where $\beta_0 = 11 - \frac{2}{3}N_f$, N_f is the number of quark flavors and Λ is the natural momentum scale of QCD. As long as there are less than 16 quark flavors $\beta_0 > 0$, consequently $\alpha_s(Q^2) \to 0$ as $Q^2 \to \infty$, making the quarks asymptotically free.

The Quark Parton Model with exact scaling and $\sigma_L = 0$ can be regarded as the zeroth order approximation of perturbative QCD.

2.2.1 Leading order QCD in DIS

The first order QCD processes that occur in DIS are shown in Figure 2.3. The photon-gluon fusion processes and gluon bremsstrahlung processes contribute to scaling violations of the structure functions and will be manifest in many variables. DIS has been a testing ground for perturbative QCD. Measurement of the azimuthal asymmetry of the final hadronic system was suggested as one of ways to study the perturbative corrections [19].

2.3 Azimuthal Distribution

The relevant hadron azimuthal angle, ϕ, in semi-inclusive leptoproduction $l + p \to l' + h + X$ is the angle of the hadron momentum projected on the plane that is perpendicular to the lepton scattering plane (formed by the virtual photon and the leptons in the center of mass frame), as shown in Figure 2.4.

2.3.1 Perturbative QCD Effect

Georgi and Politzer [19] computed to first order in α_s, the expectation value

$$\langle cos\phi \rangle = \frac{2\alpha^2}{Q^2}\frac{4\alpha_s}{3y}(2-y)\sqrt{1-y}\int_{x_{Bj}}^1 \frac{dx}{x}\int_{z_H}^1 \frac{dz}{z}\sum_j e_j^2[A_j + B_j + C_j], \tag{2.3}$$

where $x = Q^2/2p \cdot q$ and $z = p \cdot p'/p.q$ are the scaling variables. Here p is the momentum of either the struck quark in the gluon bremsstrahlung or the gluon in the photon-gluon fusion, and p' is one of the two outgoing quarks (or gluons) in the

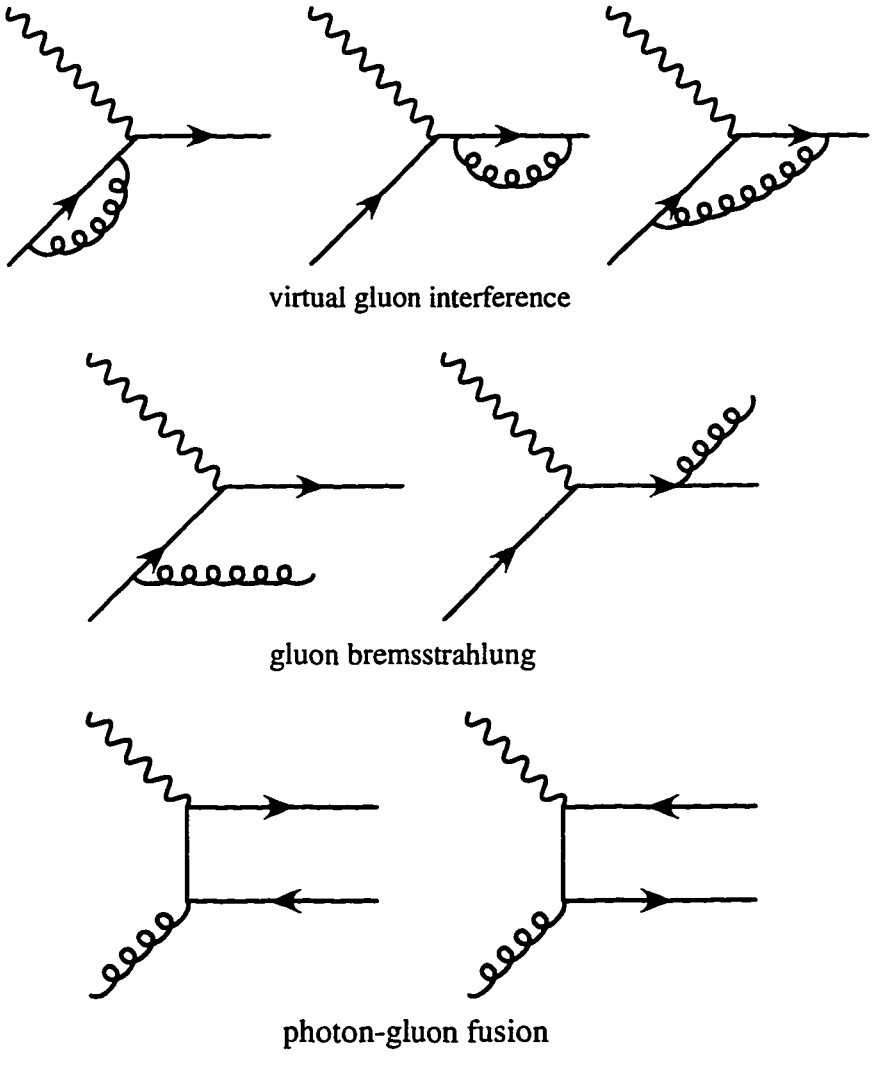

Figure 2.3: Feynman diagrams of the first order QCD processes in DIS.

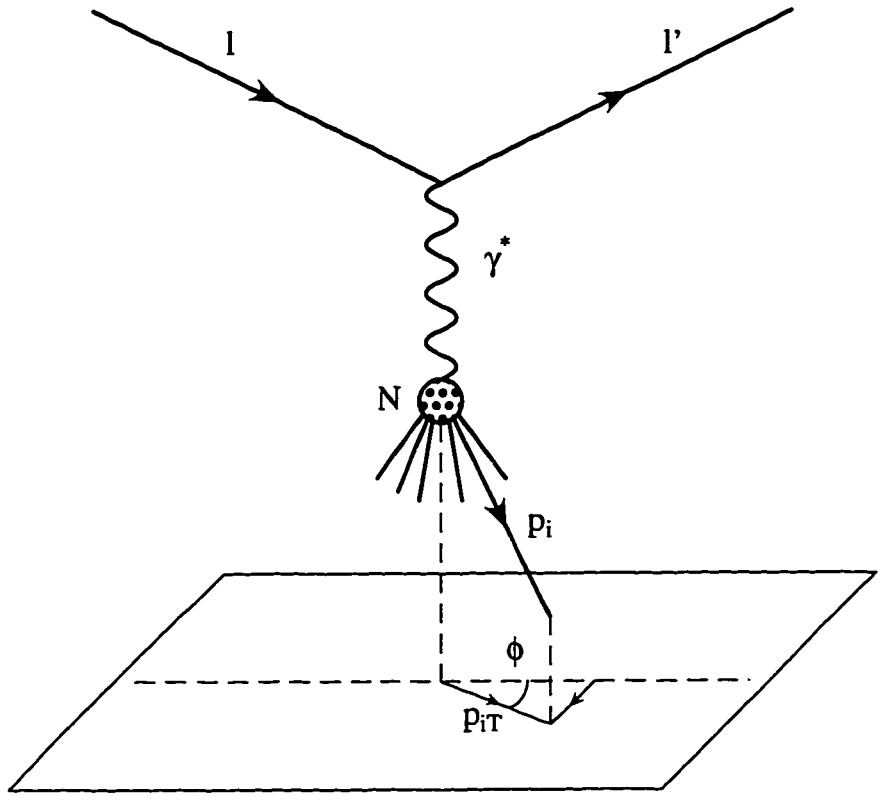

Figure 2.4: Definition of the azimuthal angle ϕ.

first order QCD process. A_j and B_j come from gluon-bremsstrahlung while C_j arises from photon-gluon fusion (see in Figure 2.3). The individual contributions are

$$\begin{aligned} A_j &= -\sqrt{\frac{xz}{(1-x)(1-z)}}[xz+(1-x)(1-z)]F_j(\frac{x_{Bj}}{x},Q^2)D_j(\frac{z_H}{z},Q^2), \\ B_j &= \sqrt{\frac{x(1-z)}{(1-x)z}}[x(1-z)+(1-x)z]F_j(\frac{x_{Bj}}{x},Q^2)D_G(\frac{z_H}{z},Q^2), \\ C_j &= -\frac{3}{8}\sqrt{\frac{x(1-x)}{z(1-z)}}(1-2x)(1-2z)F_G(\frac{x_{Bj}}{x},Q^2)D_j(\frac{z_H}{z},Q^2), \end{aligned} \tag{2.4}$$

where j labels the quark or antiquark coupled to the electromagnetic current, and G labels a gluon distribution (F_G) or a decay function (D_G). They argued that at large z_H, it is reasonable to assume that the gluon decay function is smaller than the quark decay function. Therefore, $A_j \gg B_j$ and the struck quarks tend to produce hadrons with negative $\langle cos\phi \rangle$. The contribution from gluons in the target, C, can have either sign. But at small x_{Bj}, if $f_G(\xi) \to k/\xi$ as $\xi \to 0$, where k is a constant, C_j integrates to zero (the quark-antiquark pair is produced symmetrically). Furthermore, if $F_j(\xi) \to k_j/\xi$ as $\xi \to 0$, they derived that as $x_{Bj} \to 0$ for large z_H,

$$\langle cos\phi \rangle = -\frac{\alpha_s}{2}\frac{(2-y)\sqrt{1-y}}{1+(1-y)^2}\kappa\sqrt{1-z_H}, \tag{2.5}$$

where $\kappa \simeq 1$ depends only weakly on the shape of the decay functions. They also concluded that this asymmetry is large enough to be detected and nonperturbative effects resulting from the quark confinement should not produce this kind of asymmetry at $x_{Bj} \simeq 0$. Hence the measurement of $\langle cos\phi \rangle$ provides a clean test of the perturbative QCD.

2.3.2 Non-Perturbative QCD Effect - Intrinsic K_T

In contrast, Cahn cast doubt on the utility of azimuthal asymmetry as a clean perturbative QCD test [20]. Using the simple quark parton model, he calculated, for electroproduction, in the deep inelastic limit ($\nu \gg Q$, and $cos(\theta/2) \approx 1$), to lowest order in K_T/Q, the cross-section

$$\sigma \propto A + Bcos\phi + Ccos2\phi \tag{2.6}$$

with [1]

$$\begin{aligned} A &= 1+(1-y)^2, \\ B &= -\frac{4K_T}{Q}(2-y)\sqrt{1-y}, \\ C &= \frac{4K_T^2}{Q^2}(1-y). \end{aligned} \tag{2.7}$$

Therefore, we have

$$\langle cos\phi \rangle = -\left(\frac{2K_T}{Q}\right)\frac{(2-y)\sqrt{1-y}}{1+(1-y)^2}, \tag{2.8a}$$

$$\langle cos2\phi \rangle = -\left(\frac{2K_T^2}{Q^2}\right)\frac{1-y}{1+(1-y)^2}, \tag{2.8b}$$

where $y = \nu/E$ and K_T is the intrinsic transverse momentum of the struck parton defined by

$$\begin{aligned} p &= \xi P + K_T \\ K_T &= (0,\ K_T cos\phi,\ K_T sin\phi,\ 0) \end{aligned} \tag{2.9}$$

and p and P are the momenta of the struck parton and the target proton, respectively. In his later paper [21], he further argued that the proper sum of cross-sections contributed by individual partons does not introduce an extra $cos\phi$ dependence, and the integration over final hadrons or hadron jets does not result in more azimuthal dependence. Thus Eq. 2.8 deduced from the simple single quark calculation remains correct for measuring the azimuthal asymmetry of ep scattering.

It is worth emphasizing that Cahn's ϕ is defined as the azimuthal angle between the intrinsic K_T and the leptonic plane as in Figure 2.5, not the individual hadron azimuthal angle as in Figure 2.4. He also concluded that this ϕ dependence is reflected in the final hadron distribution, but the observed hadron transverse momentum should be replaced by p_{T_H}/z_H before being interpreted as the parton transverse momentum K_T.

---

[1] The coefficients of B and C are twice as what appeared in Cahn's first paper [20], because Eq. 11 of [20] should be

$$s \approx 2xME(1-2(K_T/Q)\sqrt{1-y}\,cos\phi),$$

$$-u \approx 2xME'(1-2(K_T/Q\sqrt{1-y})\,cos\phi).$$

Cahn's next paper [21] did correct this.

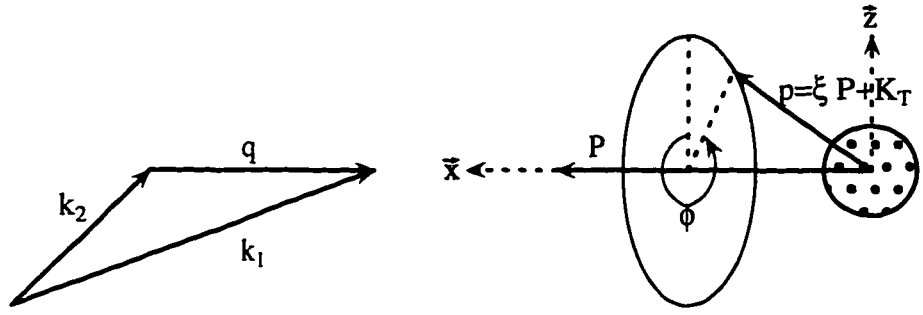

Figure 2.5: Cahn's definition of ϕ.

Considering the hadronization, if the decay or fragmentation function introduces transverse momentum, the magnitude of the azimuthal asymmetry will be reduced. But still, the asymmetry varies as Q^{-1} at fixed p_{T_H}/z_H while the perturbative QCD result varies slowly with Q^2 at high z_H due to the logarithmic dependence of α_s. In the limit $z_H \to 1$, the perturbative QCD prediction vanishes, but the parton model predicts the largest asymmetry.

2.3.3 Effect of p_{Tcut}

J. Chay, S. Ellis and W. Stirling [22] introduced another factor in the hadron azimuthal asymmetry: the experimental cut-off of the hadron transverse momentum, p_c. They discussed in detail how the combination of the intrinsic K_T and the first order QCD contributions to the azimuthal asymmetry of final hadrons depend on this p_c by using a simple mathematic model.

They assumed that the parton distribution function as a function of the intrinsic parton transverse momentum is a product of

$$F \to F(\xi, Q^2)\, f(\vec{K}_T)\, d^2\vec{K}_T. \tag{2.10}$$

Further more, they assumed that $f(K_T)$ can be parametrized as a Gaussian with width a,

$$f(\vec{K}_T) = f(|\vec{K}_T| = \rho) = \frac{1}{a^2\pi} e^{-\rho^2/a^2}, \tag{2.11}$$

which is normalized to unity.

$$\int d^2\rho f(\rho) = 1.$$

The average intrinsic transverse momentum is then

$$\langle K_T \rangle = a\sqrt{\pi}/2.$$

They accounted for the transverse momentum introduced by the fragmentation process in a similar fashion. They assumed that the final hadron is given by $p_H = \xi' p_p + \vec{p}_\perp$, with $z_H = \xi' z$ and the fragmentation function

$$D \rightarrow D(\xi', Q^2)\, d(\vec{p}_\perp)\, d^2\vec{p}_\perp, \tag{2.12}$$

where

$$d(\vec{p}_\perp) = d(|\vec{p}_\perp| = \rho') = \frac{1}{b^2\pi} e^{-\rho'^2/b^2} \tag{2.13}$$

is a simple Gaussian of width b normalized to unity.

The measured average value of $cos\phi$ is given by

$$\langle cos\phi \rangle = \frac{\int d\sigma^{(0)} cos\phi + \int d\sigma^{(1)} cos\phi}{\int d\sigma^{(0)} + \int d\sigma^{(1)}} \tag{2.14}$$

where we ignore the higher order terms.

To the lowest order, in the limit $M^2/Q^2 \ll 1$ and neglecting higher order in ρ^2/Q^2, they obtained

$$\begin{aligned} \int d\sigma^{(0)} cos\phi &= -\frac{8\pi\alpha^2}{Q^2} \frac{(2-y)\sqrt{1-y}}{y} \sum_j Q_j^2 F_j(x_{Bj}) D_j(z_H) \\ &\quad \frac{a^2 z_H}{Q\sqrt{b^2 + a^2 z_H^2}} \int_{\frac{p_c}{\sqrt{b^2+a^2 z_H^2}}}^{\infty} dx\, x^2 e^{-x^2}, \end{aligned} \tag{2.15a}$$

$$\begin{aligned} \int d\sigma^{(0)} &= \frac{2\pi\alpha^2}{Q^2} \sum_j Q_j^2 F_j(x_{Bj}) D_j(z_H) e^{-\frac{p_c^2}{b^2 + z_H^2 a^2}} \left\{ \frac{1+(1-y)^2}{y} \right. \\ &+ \left. 4\frac{1-y}{yQ^2} \left[\frac{a^2 b^2}{b^2 + z_H^2 a^2} + \left(\frac{z_H a^2}{b^2 + z_H^2 a^2} \right)^2 (p_c^2 + b^2 + z_H^2 a^2) \right] \right\} \end{aligned} \tag{2.15b}$$

Including intrinsic transverse momentum leads to a nonzero, negative $\langle cos\phi \rangle$ for the zeroth-order cross section in perturbative QCD. This asymmetry also depends explicitly on the cut-off p_c.

The first order QCD calculation of $\langle cos\phi \rangle$ for final hadrons with $p_c > 2\,GeV$ is, to a good approximation,

$$\langle cos\phi \rangle \approx \frac{\int d\sigma^{(1)} cos\phi}{\int d\sigma^{(1)}},$$

where

$$\int d\sigma^{(1)} cos\phi = \frac{8\alpha_s\alpha^2}{3Q^2} \frac{(2-y)\sqrt{1-y}}{y} \int_{x_{Bj}}^1 \frac{dx}{x} \int_{z_H}^1 \frac{dz}{z} \sum_j Q_j^2 (A_j + B_j + C_j), \tag{2.16a}$$

$$\int d\sigma^{(1)} = \frac{4\alpha_s\alpha^2}{3Q^2} \frac{1}{y} \int_{x_{Bj}}^1 \frac{dx}{x} \int_{z_H}^1 \frac{dz}{z} \sum_j Q_j^2 (A'_j + B'_j + C'_j). \tag{2.16b}$$

Here A_j, B_j and C_j are the same as in Eq. 2.4 derived by Georgi and Politzer. A'_j, B'_j and C'_j are[2]

$$
\begin{aligned}
A'_j &= \left([1+(1-y)^2]\frac{x^2+z^2}{(1-x)(1-z)} + 2y^2(1+xz) + 4(1-y)(1+3xz)\right) \\
&\quad F_j(\frac{x_{Bj}}{x}, Q^2) D_j(\frac{z_H}{z}, Q^2), \\
B'_j &= \left([1+(1-y)^2]\frac{x^2+(1-z)^2}{z(1-z)} + 2y^2(1+x-xz) + 4(1-y)(1+3x(1-z))\right) \\
&\quad F_j(\frac{x_{Bj}}{x}, Q^2) D_G(\frac{z_H}{z}, Q^2), \qquad (2.17) \\
C'_j &= \frac{3}{8}\left([1+(1-y)^2][x^2+(1-x)^2]\frac{z^2+(1-z)^2}{z(1-z)} + 16(1-y)x(1-x)\right) \\
&\quad F_G(\frac{x_{Bj}}{x}, Q^2) D_j(\frac{z_H}{z}, Q^2).
\end{aligned}
$$

Chay, Ellis and Stirling also used a numerical program to calculate the $\langle cos\phi \rangle$ dependence on p_c with different values of a and b. It can be compared with experiment results directly as shown in Figure 2.6. At small Q^2, for small p_c, the K_T effect dominates. The value of the asymmetry depends on a and b. For larger Q^2 or with large p_c, the details of the nonperturbative contributions are suppressed. However $\langle cos\phi \rangle$ still displays nontrivial dependence on the momentum cutoff p_c. See Figure 2.7

2.3.4 Experimental Verification

The European Muon Collaboration made one of the first measurements [23] of hadron azimuthal distribution and concluded that the hard QCD contribution is relatively minor and indicated the value of $\langle abs(K_T) \rangle \geq 0.44\, GeV$. They also formed a strong dependence of $\langle cos\phi \rangle$ on x_F, where $x_F = 2p_{||}/W$ is the often used Feynman x.

E665 members D. Jansen [24] and M. Baker [25] have also studied this hadron azimuthal asymmetry. They both concluded that the asymmetry does not depend on Q^2, but on z_H or x_F. Apart from that, Jansen had compared his data with Chay, Ellis and Stirling's numerical results, and concluded that a and b are both around 0.5 GeV. Baker also derived higher order corrections to the asymmetry coming from the K_T effect and concluded that Cahn's lowest order prediction is only good when $K_T/Q < 0.2$.

---

[2] The sign of x in A'_j and B'_j has been corrected from the original paper.

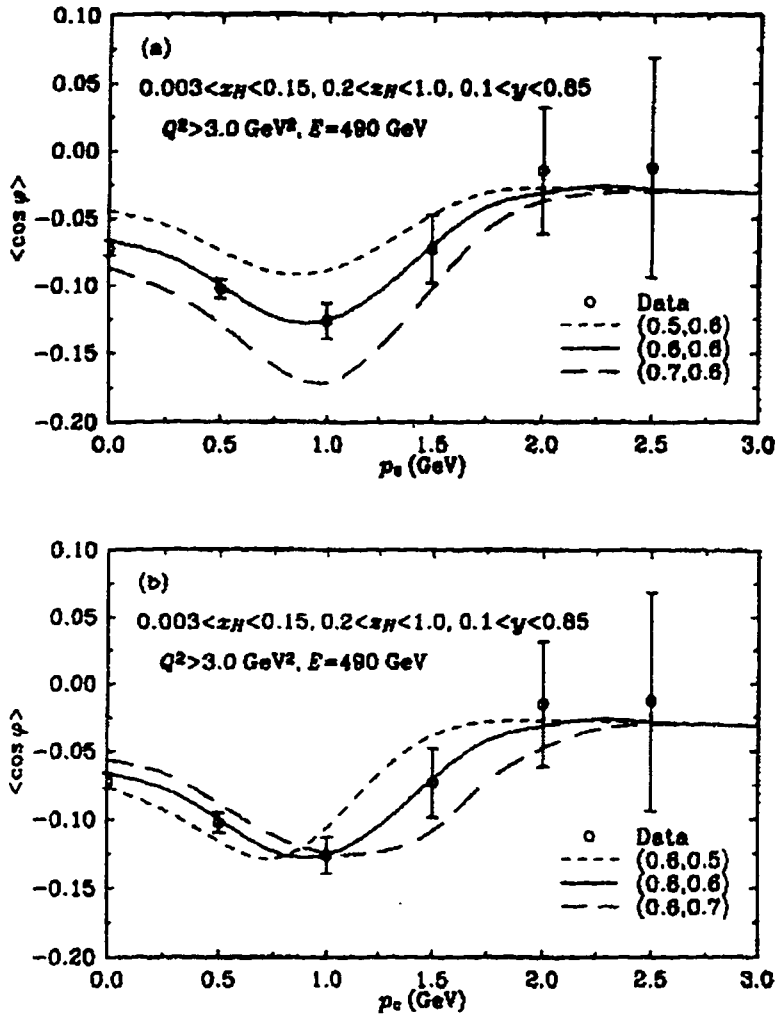

Figure 2.6: The p_c dependence of $\langle cos\phi \rangle$ of Jansen's data [24] fit to Chay, Ellis and Stirling's numerical calculation in Chay, Ellis and Stirling's paper [22]. (a) various values of a with $b = 0.6\,GeV$ and (b) various values of b with $a = 0.6\,GeV$.

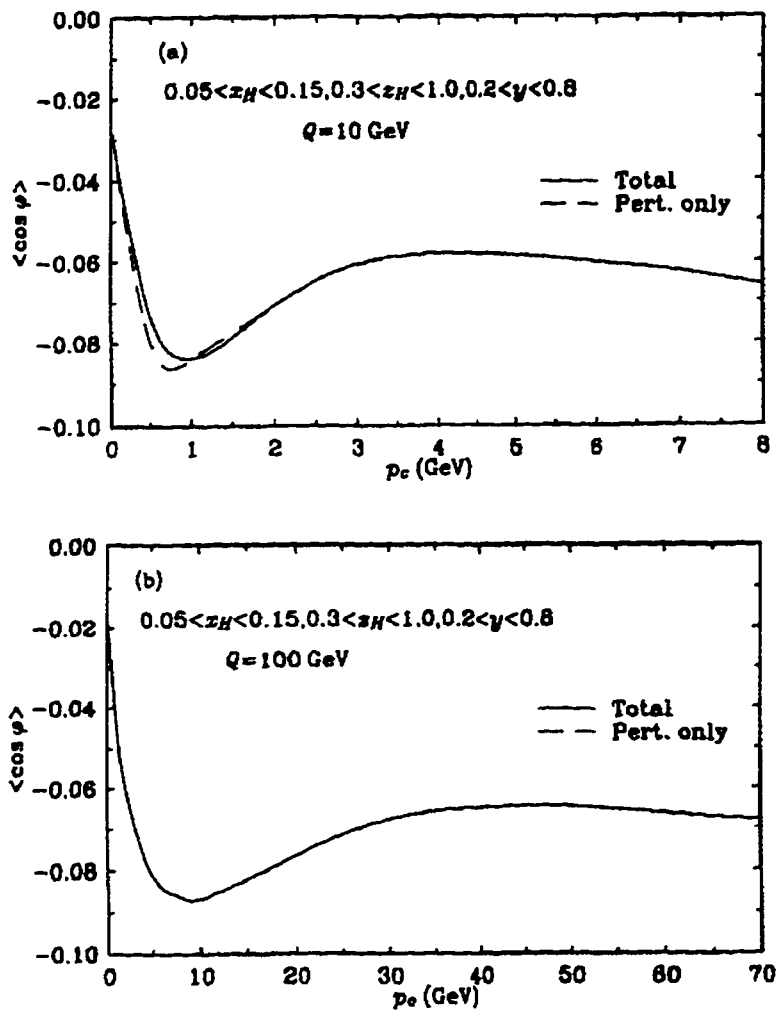

Figure 2.7: Calculated p_c dependence $\langle cos\phi \rangle$ for larger Q according in Chay, Ellis and Stirling's model.

Chapter 3

JETS

3.1 Partons and Jets

The distribution of the outgoing partons resulting from the nucleon breakup carries information about the momentum distribution of partons inside the nucleon. Therefore by studying the parton kinematics after the scattering, one can infer properties of partons and structure of nucleons.

When a quark or gluon leaves the site of a hard scattering, it does not remain free due to the color confinement in QCD. Instead, it hadronizes, or fragments onto a collection of colorless hadronic particles. Although the complex hadronization process is not fully understood, this collection, which is called a jet, often contains kinematic properties strongly correlated with the partons [27]. In 1969, Georgi and Sheiman [31] had argued that, assuming the collinear decay of partons, the transverse momentum distribution of the final hadrons is analogous to the distribution of the produced partons.

The jet structure in hadronic final states was first experimentally observed in e^+e^- annihilation [32] in 1975. Ever since then different jet-finding algorithms have been developed in order to better reveal the underlying parton structure from the observed jet momenta and their distributions. The choice of an optimal algorithm to reconstruct jets from the measured hadrons is not a simple matter, however. For example, Hedberg, Ingelman, Jacobsson and Jonsson at HERA [27] have discussed five algorithms for jet reconstruction: JADE, Luclus, Lucell, Arclus and $k_\perp$. In their experiment 26.7 GeV electrons collide with 820 GeV protons with a center of mass energy of 296 GeV. The JADE [33] algorithm developed for the e^+e^- annihilation experiment JADE performed consistently worse than the other four algorithms. This is understandable since the JADE algorithm was not designed for initial hadron states. In e^+e^- collisions the initial state is purely electromagnetic and the entire final state can be considered as one arising from the hard scattering of a virtual photon with quarks. However, for ep or μp scattering experiments, there is a backward spectator

jet which must be taken into account. The spectator jet, or beam jet, consists of particles associated with the the proton target beam, which does not take part in the hard scattering process. It travels in the opposite direction to the virtual photon and is of no interest to most analysis including this thesis.

An E665 thesis (J. Conrad [45]) made use of a modified JADE algorithm to identify jets and measure the strong coupling constant α_s from the distribution of the jet transverse momentum. The modification was based on the work of Graudenz and Magnussen[1]. A pseudo-backward parton is added as the spectator jet to correct for the poor particle measurements in the backward hemisphere (CMS) of the virtual photon and the target. These are low energy particles in the lab frame. E665 is a fixed target μp scattering experiment. Its spectrometer does not have as good efficiency in the backward semisphere as it does in the forward region (CMS). On the other hand, the hadrons in the spectator jet mostly travel backwards in the CMS. Adding a pseudo particle not only conserves the momentum but also helps to merge low-energy particles to the spectator jet.

Another approach called the $k_\perp$ algorithm[2] [36] also deals with the spectator jet problem by explicitly collecting the particles associated with the target before resolving the final jet structure. As pointed out by Catani [35] this algorithm also ensures soft gluon exponentiation and therefore is infrared and collinear safe. This and the modified JADE algorithms will be studied in this chapter.

A relatively new algorithm [37] proposed by Ellis and Soper is also examined and compared with Monte Carlo data. It deals with the spectator jet problem by neglecting particles or jets with small transverse momenta, which the authors assume are mainly random and are associated with the beam or target. The drawback of this approach is that it introduces a cutoff threshold on the transverse momenta of the jets. The algorithm was intended for high-energy ep or pp colliding experiments to replace the cone style algorithms[3]. The possibility of adopting this algorithm to lower

---

[1] HERA workshop 1991

[2] $k_\perp$ algorithm first proposed in reference [35] for e^+e^- annihilation is also known as the Durham algorithm, because it arose from discussions at the Durham Workshop on Jet Studies at LEP and HERA, December 1990.

[3] A jet from the cone style algorithms is typically defined in terms of some n particles whose momenta lie within a cone centered at the jet axis in pseudo-rapidity η and azimuthal angle ϕ. A more detailed discussion can be found in reference [38].

energy experiments or fixed target experiments will be investigated in this chapter.

As part of the LUND Monte Carlo QCD simulation package, the program ARIADNE has implemented a jet clustering algorithm Arclus [39] which is closely related to the Color Dipole Model (CDM). CDM treats each gluon emitted from a $q\bar{q}$ pair as radiation from the color dipole between the q and $\bar{q}$. This unique algorithm considers any combinations of three particles or particle clusters as two quark clusters forming a dipole and radiating a third gluon cluster. In the end, none of the particles is associated with only one jet. This also fits well into the LUND string fragmentation picture [42] where a hadron is not produced just by one parton but rather in the string between two partons. This chapter will also explore the feasibility of using Arclus as the jet clustering algorithm for E665 data.

3.2 Definition of The Jet Algorithms

3.2.1 The Modified JADE Algorithm

The original JADE algorithm is summarized as the following:

1. Define a resolution parameter Y_{cut} and an energy scaling variable Y_{scale}.

2. For any particle or cluster compute

$$Y_{ij}^2 = \frac{2E_iE_j(1-\cos\theta_{ij})}{Y_{scale}^2}. \tag{3.1}$$

3. If the smallest value $Y_{ij} < Y_{cut}$, combine i and j into a single cluster k with

$$p_k^\mu = p_i^\mu + p_j^\mu. \tag{3.2}$$

4. Repeat this procedure from step 2 until all pairs of particles or clusters have $Y_{ij} > Y_{cut}$. At this stage the remaining clusters are called jets.

As mentioned above, the only modification to the original JADE algorithm in this analysis is the addition of a backward pseudo-particle with

$$\begin{aligned} \vec{p} &= -\textstyle\sum_i \vec{p}_{Li} \\ E &= |\vec{p}|, \end{aligned} \tag{3.3}$$

where $\vec{p}_{Li}$ is the longitudinal momentum of particle i in the center of mass frame and the summation is performed over all the detected particles. In this thesis, the modified JADE algorithm will be referred to as JADE from now on unless otherwise specified.

JADE is applied in the center-of-mass frame of the reconstructed virtual photon and the target. The jet that contains the pseudo backward particle is removed from the final analysis. The Y_{scale} used is $W/2$, where W is the momentum of the hadronic system[4].

3.2.2 The $k_\perp$ Algorithm

There are two major steps in the $k_\perp$ algorithm [36]: *(A)* preclustering the hadrons into a "beam jet" and "final-state macro-jets" and *(B)* resolving final-state jets within the macro-jets.

(A) Preclustering

1. Define a hard scattering scale Y_{scale} ($Q^2 \geq Y^2_{scale} \gg \Lambda^2$, where Λ is the QCD scale[5]).

2. For every final state particle (or particle cluster) i, calculate in the Breit frame[6]

$$Y^2_{ij} = \frac{2\,min(E_i^2, E_j^2)\,(1 - cos\,\theta_{ij})}{Y^2_{scale}}, \tag{3.4a}$$

$$Y^2_{ip} = \frac{2\,E_i^2\,(1 - cos\,\theta_{ip})}{Y^2_{scale}}, \tag{3.4b}$$

where θ_{ij} and θ_{ip} are the angles between the momentum vectors of i and j (another particle or cluster) and between i and the proton p. E_i and E_j are the corresponding energies of i and j.

---

[4] In the original JADE algorithm, the invariant mass for any pair of particles in an event is scaled by the total energy W in the CMS. But for a fixed target experiment $W/2$ is a reasonable approximation for the CMS energy. On the other hand, Y_{scale} is just a scaling variable. When we compare Y_{cut} with those from other experiments, we need to bare in mind that our scaling is $W/2$.

[5] The common choice of Λ_{QCD} is 0.28 GeV [49],

[6] In Breit frame, if we define $\hat{x}$ as the longitudinal direction, the virtual photon carries momentum $q = (0, -2xP, 0_\perp)$ and the struck quark's momentum is $p = (xP, -xP, 0_\perp)$. Here P is the momentum of the target nucleus.

3. Take the smallest value among Y_{ij}, Y_{ip}. If Y_{ij} is the smallest and $Y_{ij} < 1$, combine i and j into a single cluster. If Y_{ip} is the smallest and $Y_{ip} < 1$, i is included in the "beam jet" and will be discarded from further clustering.

4. Repeat this procedure from step 2 for all particles and clusters until there exists no more Y_{ij} or $Y_{ip} < 1$.

The preclustering procedure removes the particles associated with the target, or the so-called spectator jet.

(B) Resolving jet structure

1. Define a resolution parameter $Y_{cut} < 1$.

2. For any hadron in the final-state macro-jets, compute

$$Y_{ij}^2 = \frac{2\,min(E_i^2, E_j^2)\,(1 - cos\,\theta_{ij})}{Y_{scale}^2}. \tag{3.5}$$

3. Take the smallest value among the Y_{ij}. If it is smaller than Y_{cut}, combine i and j into a single cluster.

4. Repeat this procedure from step 2 until all pairs of particles or clusters have $Y_{ij} > Y_{cut}$. At this stage the remaining clusters are called jets.

The result of the full procedure consists of jets with relative transverse momenta $\Delta k_\perp$, where $Y_{scale} > \Delta k_\perp \geq \sqrt{Y_{cut}} Y_{scale}$. These jets are produced with large transverse momenta $p_\perp \geq Y_{scale}$ relative to the incoming target beam.

Breit Frame

The $k_\perp$-clustering procedure is not explicitly Lorentz-invariant. The frame of reference in which it is performed has to be specified. Catani [36] has pointed out that the Breit frame is preferred for DIS experiments. In this frame the jet-rate coefficient functions do not depend explicitly on the DIS kinematic variables x and y. In the Breit frame the four-vector momentum of the exchanged virtual photon is $(0, Q, 0, 0)$ in an (E, p_x, p_y, p_z) convention. In the E665 coordinates, the virtual photon points

to the $\hat{x}$ direction. The exchanged boson and proton lie along a common axis ($\hat{x}$), but longitudinally boosted backwards relative to their CMS frame. Most tracks in an event ended up backwards in the Breit frame. The defect, at least for fixed-target experiments, is that sometimes a very energetic forward particle in the CMS frame when boosted to the Breit frame has very low momentum and is then added to the spectator jet. As pointed out in reference [28], any errors on the measured (x, Q^2) values will propagate to large and correlated errors on track positions in the Breit frame and affect their probability of subsequent merging.

3.2.3 The Ellis-Soper Jet Algorithm

In lepton-hadron or hadron-hadron collisions only one "active parton" from each incident hadron participates in the hard collision. Therefore, only a fraction of the final state hadrons are to be associated with the hard scattering process. The remainder, ascribed to soft interactions of the remaining partons in the incident hadron and/or to the initial state bremsstrahlung radiation of the active parton, give a characteristic signature to the spectator jets: these particles carry small transverse momenta (relative to the beam axis) but possibly large longitudinal momenta. This feature inspired the Ellis-Soper algorithm. An additional benefit of this algorithm is that it does not require knowledge of the particles' mass.

Each particle in the Ellis-Soper algorithm is characterized by its transverse energy $E_T = |\vec{p}_T|$, its pseudorapidity $\eta = -ln[tan(\theta/2)]$ and its azimuthal angle ϕ. The procedure is summarized as the following:

0. Define a transverse energy scaling variable R, which should be of order 1.

1. For any pair of particles or clusters i and j, compute

$$D_{ij}^2 = \min(E_{Ti}^2, E_{Tj}^2)\frac{(\eta_i - \eta_j)^2 + (\phi_i - \phi_j)^2}{R^2}. \tag{3.6}$$

2. Find the smallest value among D_{ij} and E_{Ti}. If the smallest is a D_{ij}, combine i and j into a single cluster k with

$$E_{Tk} = E_{Ti} + E_{Tj}, \tag{3.7a}$$

$$\eta_k = (E_{Ti}\eta_i + E_{Tj}\eta_j)/E_{Tk}, \tag{3.7b}$$

$$\phi_k = (E_{Ti}\phi_i + E_{Tj}\phi_j)/E_{Tk}. \tag{3.7}$$

If it is an E_{Ti}, the corresponding cluster i is not "mergeable". Remove it from the list of particles or clusters and add to the list of final jets.

3. Repeat this procedure from step 2 until no more particles or clusters are left.

4. Define a transverse energy cutoff E_{Tcut} so that jets with $E_T < E_{Tcut}$ are considered to be random debris from the target remnant.

This algorithm was designed to detect hard scattering jets in non-zeroth order of QCD process. It removes soft jets together with the target remnant. Therefore many zeroth-order events that have only particles with small transverse momentum could result in zero final jet.

3.2.4 Arclus Algorithm

Arclus is inspired by the Color Dipole Model. It is different from the conventional algorithms discussed previously. In this analysis it is applied in the center of mass frame of the virtual photon and the target. The Arclus algorithm is summarized as the following:

1. Define a resolution cut p_{Tcut}.

2. A Lorentz invariant parameter p_T is calculated from any combination of three particles or clusters, i, j and k as

$$p_{Tk}^2 = m_{ijk}^2(1 - x_i + \frac{m_i^2 - (m_j + m_k)^2}{m_{ijk}^2})(1 - x_j + \frac{m_j^2 - (m_i + m_k)^2}{m_{ijk}^2}), \quad (3.8)$$

where $x_i = 2E_i/m_{ijk}$, E_i is the energy of i in the center of mass frame of i, j and k, and m_{ijk} is the invariant mass. For simplicity, we set the mass of the individual particles to zero in the equation and obtain

$$p_{Tk}^2 = m_{ijk}^2(1 - x_i)(1 - x_j) = \frac{m_{ik}^2 m_{jk}^2}{m_{ijk}^2}, \quad (3.9)$$

where m_{ik} (or m_{jk}) is the invariant mass of cluster i (or j) and k.

3. If the smallest p_T is smaller than p_{Tcut}, combine i, j and k into two new massless clusters a and b so that the center of mass frame and the invariant mass do not change, i.e., in the center of mass frame of i, j and k,

$$\begin{aligned} \vec{p}_a + \vec{p}_b = &\quad \vec{p}_i + \vec{p}_j + \vec{p}_k &= 0, \\ E_a + E_b = &\quad E_i + E_j + E_k &= m_{ijk}. \end{aligned}$$

   The two new clusters are then boosted back to the original working frame.

4. Repeat this procedure from step 2 until all combinations have p_T greater than the jet resolution cut p_{Tcut}.

The minimum number of jets found by Arclus is two, of which one is considered as the spectator jet and will be discarded before any jet analysis. A pseudo backward particle (see Eq. 3.3) is added before step 2 in order to compensate for particles in the backward hemisphere of the E665 spectrometer.

3.2.5 Final Clustering of the Particles in a Jet

Once a particle is determined to be a member of a jet by one of the algorithms above (except Arclus), we use Eq. 3.2 to group together the particles belonging to one jet and give a jet momentum based on momentum conservation.

3.3 Performance of the Jet Algorithms

3.3.1 Monte Carlo Data

In order to study the performance of the various jet algorithms and the jet characteristics we use Monte Carlo simulation to generate tracks and process the tracks through the E665 analysis chain. We compare the generated partons based on the exact matrix elements perturbative QCD calculation with the jets obtained from the reconstructed final tracks using various jet algorithms.

The E665 Monte Carlo simulation has two steps: the LUND event generation and E665 detector simulation. LUND Monte Carlo is a software package that simulates high energy physics interactions.

E665 uses Lepto 5.2 [29] to simulate deep inelastic scattering and Jetset 6.3 [30] to simulate fragmentation, hadronization, secondary interactions and decay. In

Lepto, the matrix elements corresponding to the lowest order QCD processes, gluon bremsstrahlung and photon-gluon fusion, are calculated. The output of Lepto's matrix elements calculation is the foundation for our algorithm comparison. The matrix elements are divergent in the limit when the gluon energy or the opening angle between the partons vanishes. A cutoff is used in the MC simulation to avoid these singular regions. This cutoff is implemented by requiring a minimum invariant mass $m_{ij} > 0.0025W^2$ (PARL(8) in Lepto) between any pair of partons in the final state, including the target remnant system. In order to take higher than first order QCD effects into account, the parton shower approach has been implemented as described in detail in reference [40]. In Jetset, a string model is used to convert the generated partons to hadrons. The resulting particles, before decay, will be called the "Truth" data. Acceptance corrections discussed later are to the referenced "Truth" data in this analysis.

E665's detector simulation models the response of all detector elements and provides hits. These MC hits are treated like real data, processed through our pattern recognition, track fitting, muon matching and vertex finding programs. In the end, the event is reconstructed. More detailed discussion on how to select final tracks and calorimeter clusters is presented in Chapter 5.

The jet algorithms are applied to the final reconstructed tracks and energies.

3.3.2 Selecting Extra Adjusting Parameters for the $k_\perp$ and Ellis-Soper Algorithms

The $k_\perp$ and Ellis-Soper algorithms have two adjustable parameters while the modified JADE and Arclus algorithms each has only one adjustable parameter. This section discusses how to choose one of the parameters in the $k_\perp$ and Ellis-Soper algorithms.

In the preclustering procedure for the $k_\perp$ algorithm, we have to select Y_{scale} so that $\Lambda_{QCD} \ll Y_{scale} \leq Q$. Monte Carlo data samples with a cut of $Q^2 \geq 3\,GeV^2$ yields $0.28\,GeV \ll Y_{scale} \leq \sqrt{3}\,GeV$. We found that for smaller values of Y_{scale}, the fraction of reconstructed multiple jet events increases. When $Y^2_{scale} = 0.5\,GeV^2$, the number of reconstructed three or more jet events reaches 41% for the maximum allowed $Y_{cut}(1)$. This is not acceptable, because the MC does not generate so many higher order QCD events. Therefore, three preliminary Y^2_{scale} values — 1, 2, 3 GeV^2 — are used for comparison.

The original paper on the Ellis-Soper algorithm suggests that the parameter R should be close to one. In this analysis we can choose R to be greater than one. The

reason for it is that E665 has relatively low Q^2 compared to collider experiments. The multiplicity is lower and particles are further apart in the η, ϕ space. Larger R results in combining particles that are further apart. Three preliminary choices of $R = 1, \sqrt{2}$ and 2 will be compared.

3.3.3 Jet Rate and the Purity of Reconstructed 2-jet Events

In this thesis we define an event with n forward jets plus the remnant as an n-jet event. The 2-jet event rate obtained from the reconstructed final states by using the different jet algorithms discussed in this chapter are plotted in Figure 3.1.

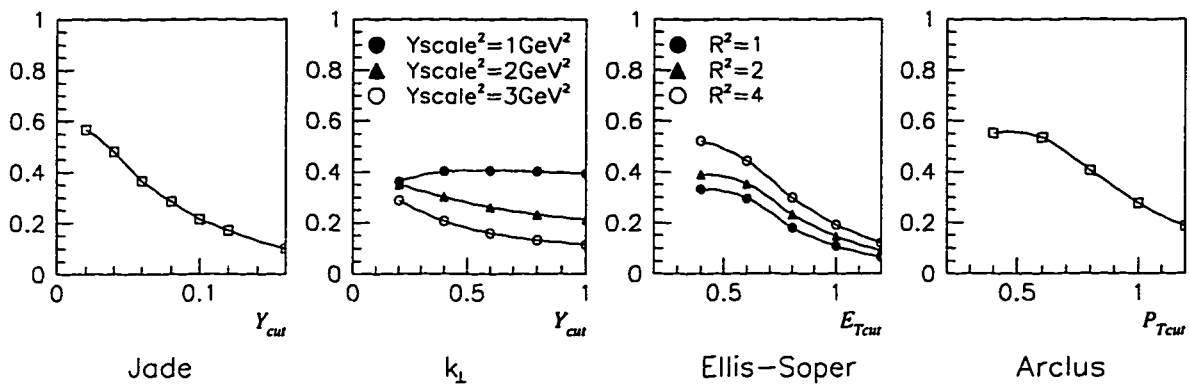

Figure 3.1: Reconstructed 2-jet event rate vs. relevant cuts.

The fraction of these 2-jet events that are associated with original 2-parton events are plotted in Figure 3.2. This fraction of 2-jet events is a measure of the so-called purity of 2-jet events.

Using larger cuts results in fewer 2-jet events but with improved purity. However, we still cannot achieve more than 60% in purity without losing too many events. In other words, over 40% of the reconstructed 2-jet events are incorrectly identified by the algorithms. They are really 1-parton events. A combined picture is plotted in Figure 3.3.

The contamination introduced by misidentifying 1-parton events as 2-jet events can be minimized by using more severe cuts, such as requiring the reconstructed center of mass energy $\sqrt{s}$ greater than 15 GeV and the polar angle of the jets to be greater than 10 degrees, as discussed in reference [27]. Unfortunately, E665 data have moderate energy and will not survive these cuts.

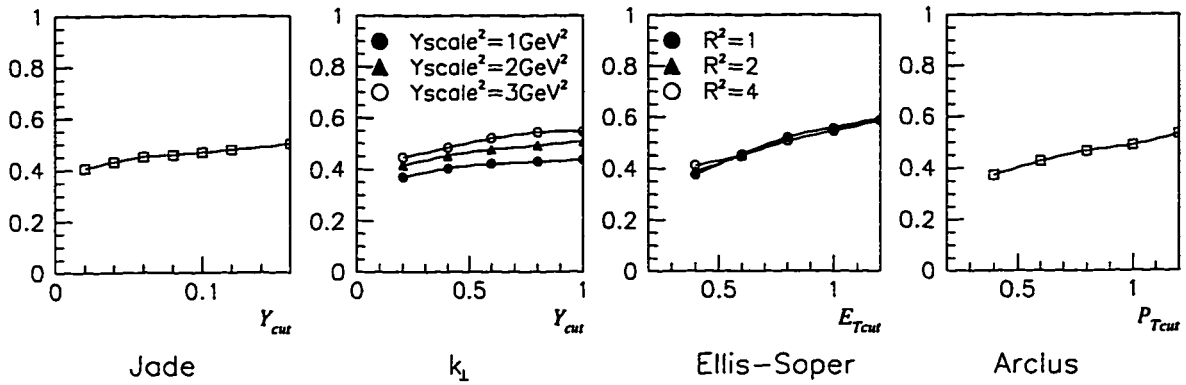

Figure 3.2: Purity of 2-jet events vs. relevant cuts.

At the parton level, not all the 1-parton events are true zeroth order QCD events (see reference [45] for more detailed discussion). The parton shower adds soft radiations which could introduce a second or even third parton. Those two or more parton events which are highly collinear or have a soft second parton are classified as 1-parton events. In other words, these 1-parton events have actually gone through none-zeroth order QCD processes. Therefore, even if an algorithm does not achieve 100% purity in its 2-jet event sample, it can still be used to analyze the first order perturbative QCD process.

Figures 3.4 to 3.7 show how well these algorithms agree with each other. At lower thresholds, these algorithms select different sets of events as 2-jet events. At similar jet rates, all algorithms overlap at about the 70% level except for the $k_\perp$ algorithm which overlaps with others only about 50% of the time.

3.3.4 Characteristics of 2-jet Events

Misassigning particles from one jet to another, misidentifying 1-parton events as 2-jet events or 2-parton events as 1-jet events introduces errors in the jet analysis. Therefore, it is important to choose an algorithm that has good agreement between the jet and parton characteristics.

Misassigning particles in jet 1 to jet 2 is called "cross talk" between the jets. Cross talk not only decreases the magnitude of the transverse momenta of the jets, but also shifts their directions. Due to the color confinement, at least one particle must be shared between the two partons. Therefore, cross talk always exists. In order to reduce misassignment, larger values of the jet resolution cuts are preferred in order to

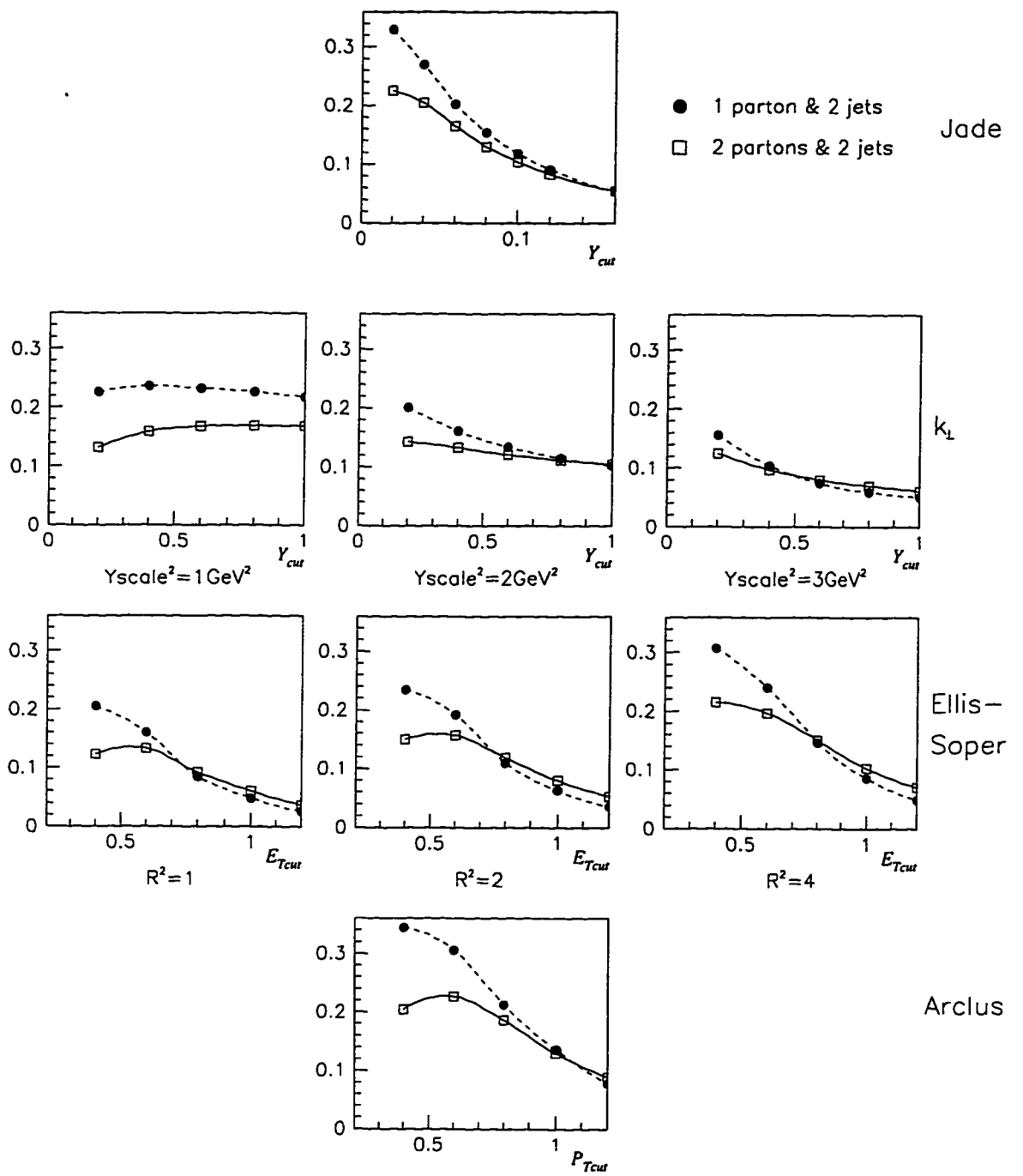

Figure 3.3: Fraction of the pure 2-jet events and the misidentified 2-jet events.

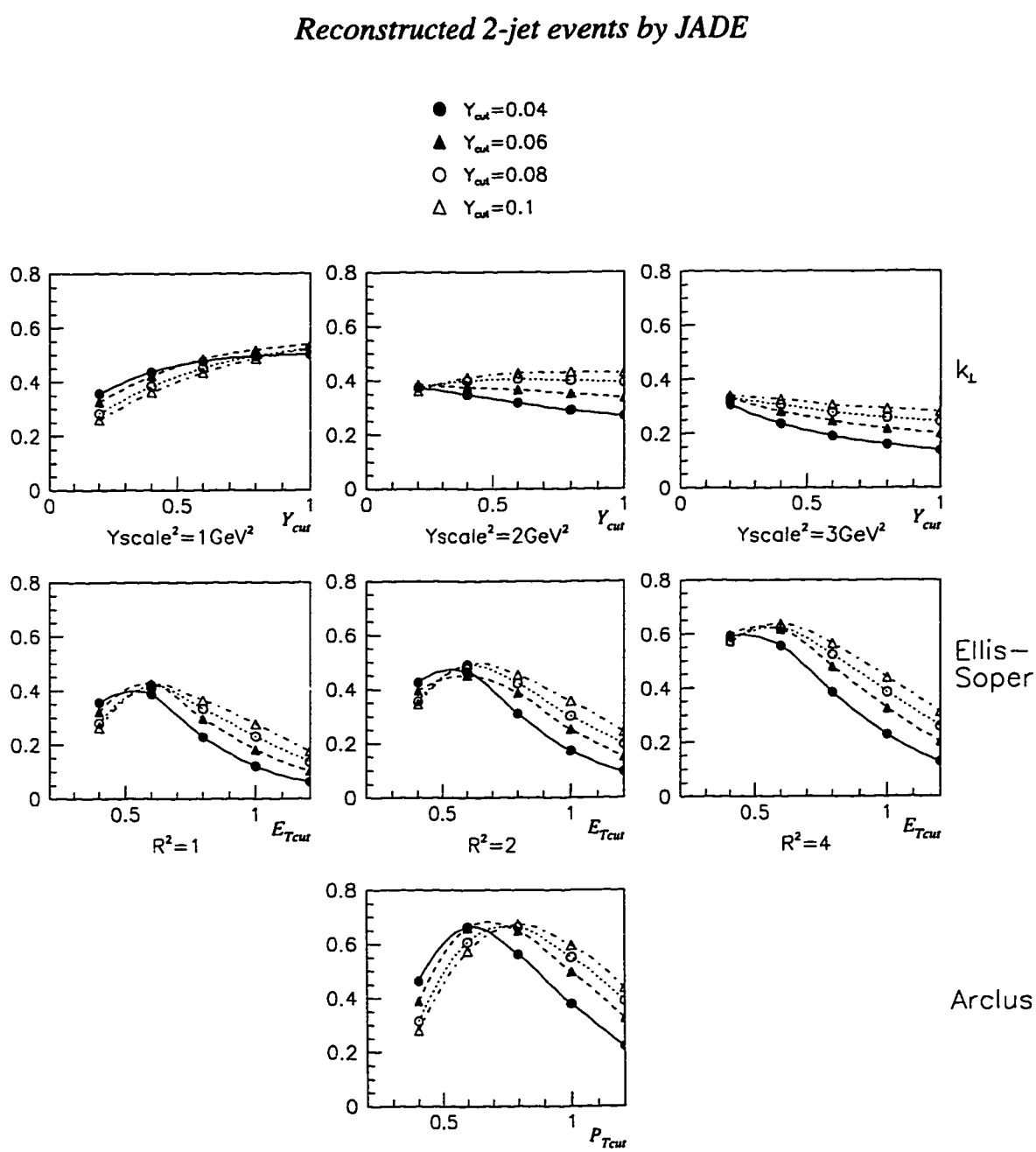

Figure 3.4: Fraction of JADE 2-jet events that are also reconstructed as 2-jet events by using other algorithms.

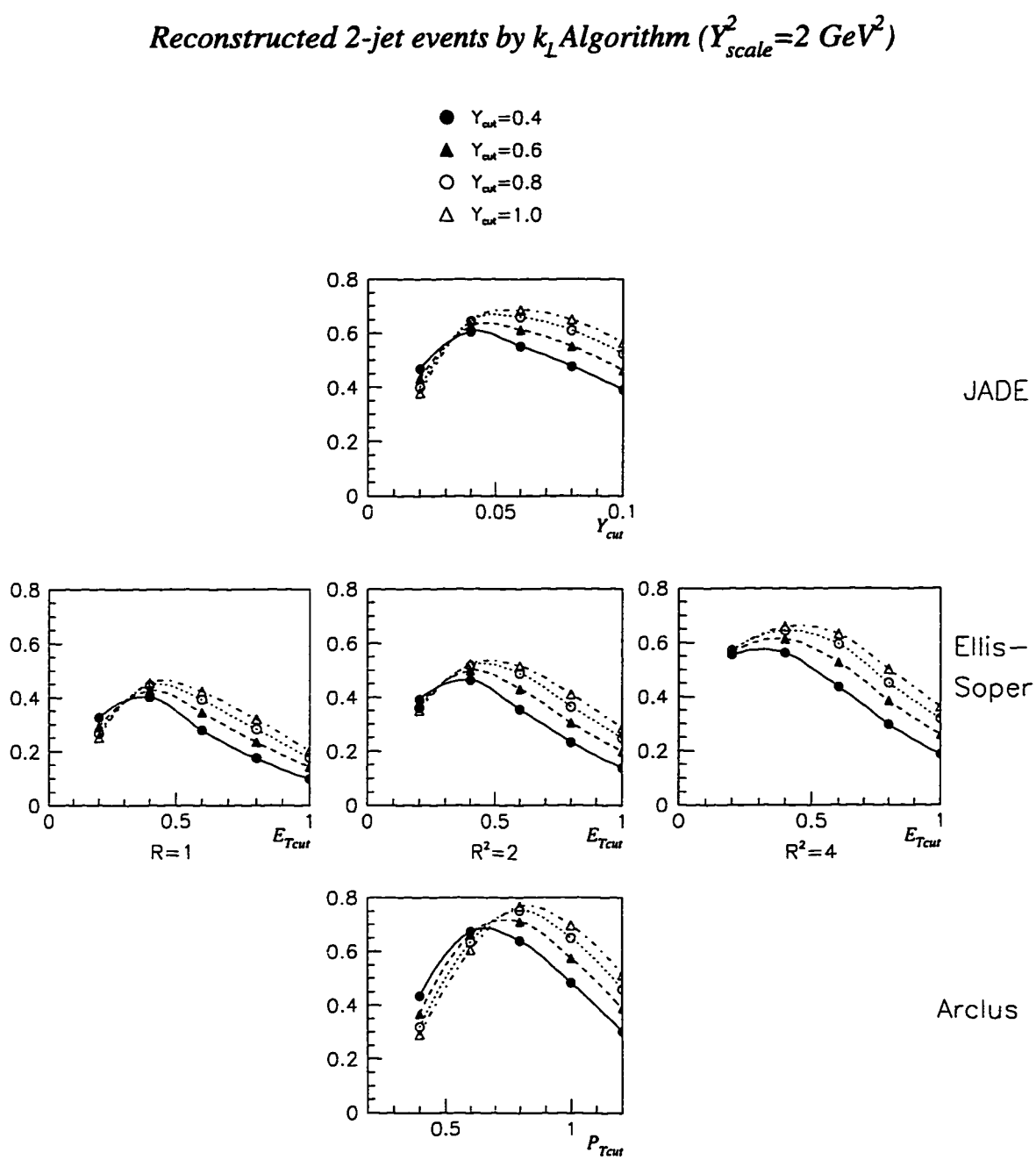

Figure 3.5: Fraction of the $k_\perp$ 2-jet events that are also reconstructed as 2-jet events by using other algorithms.

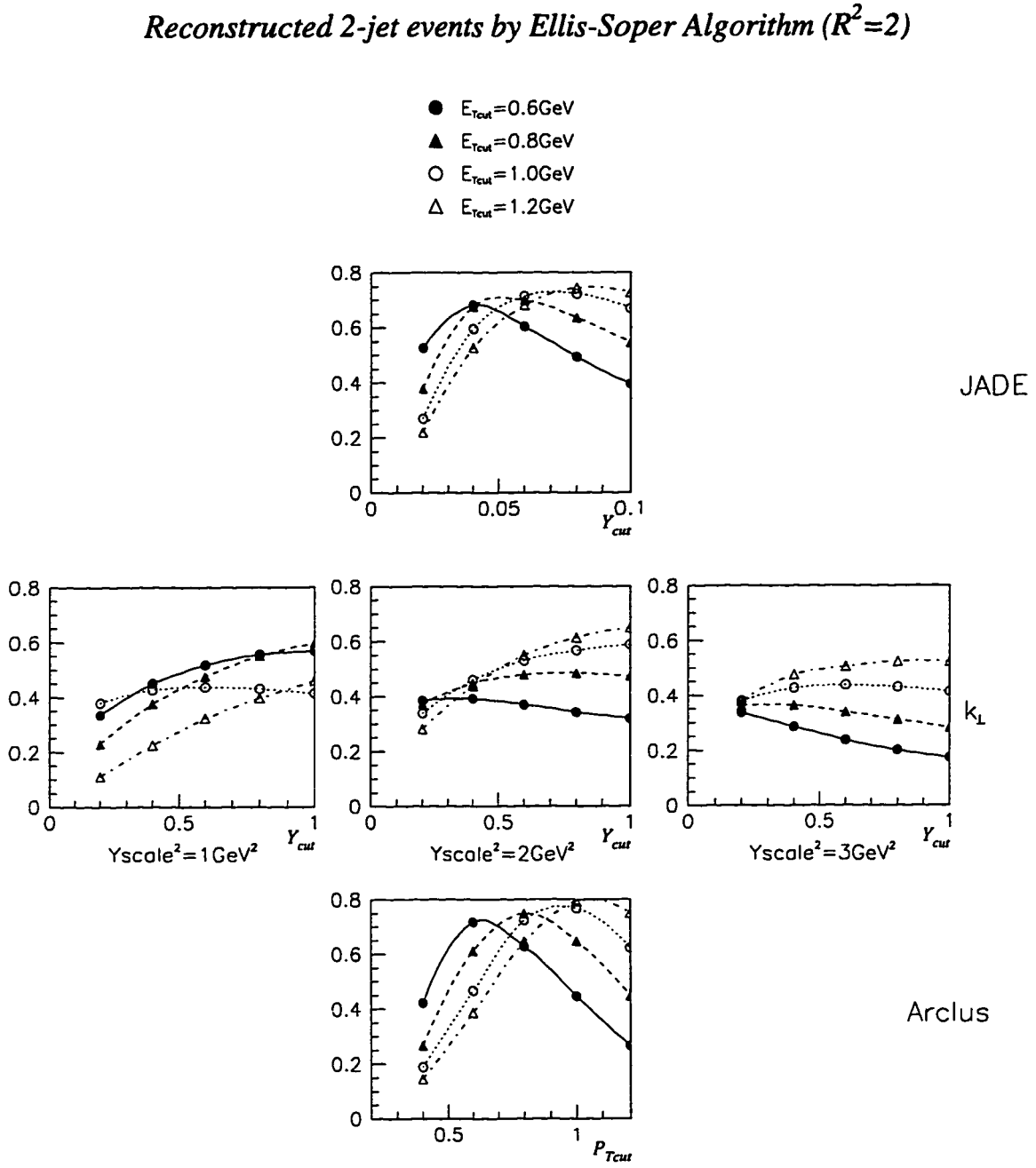

Figure 3.6: Fraction of Ellis-Soper 2-jet events (using $R^2 = 2$) that are also reconstructed as 2-jet events by using other algorithms.

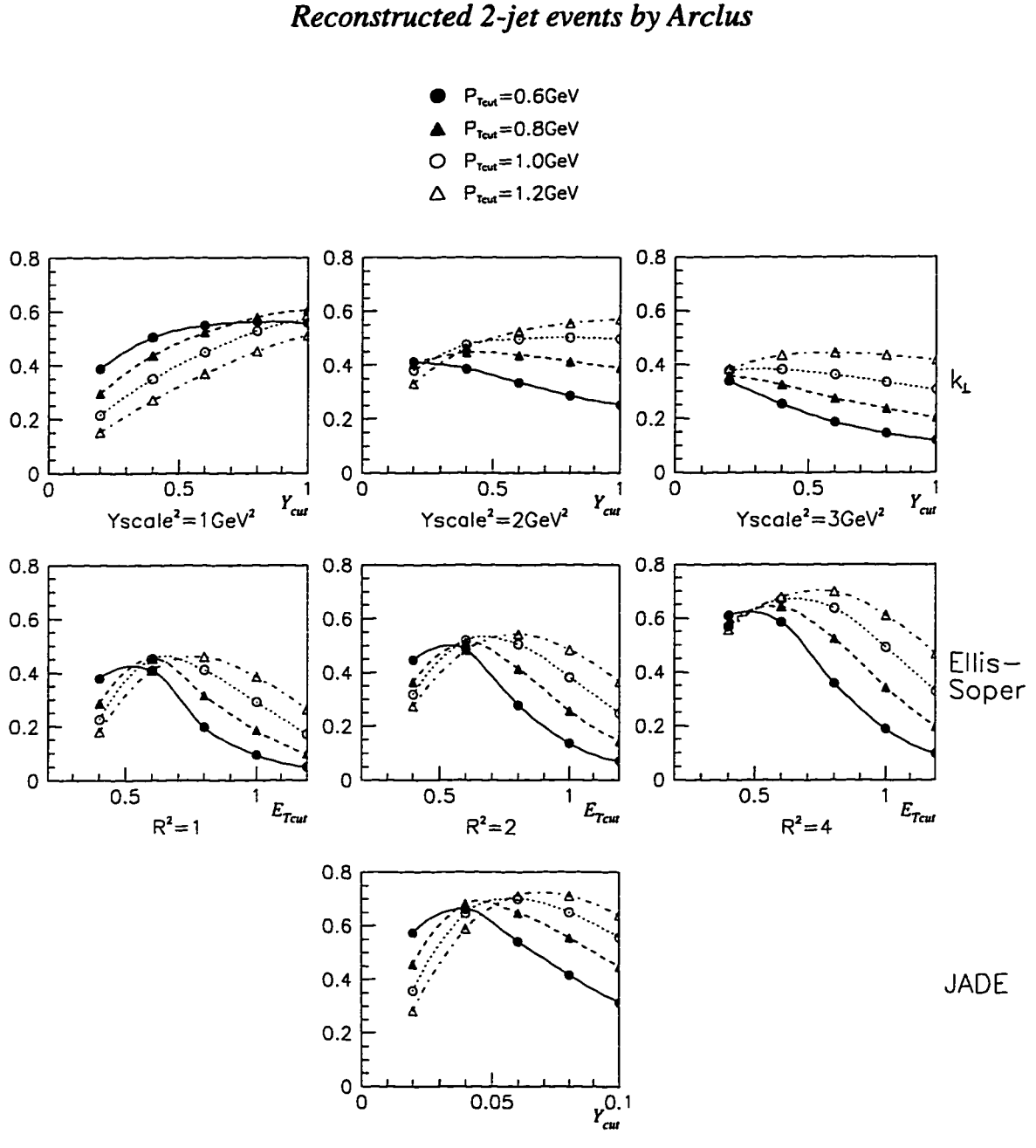

Figure 3.7: Fraction of Arclus 2-jet events that are also reconstructed as 2-jet events by using other algorithms.

produce well separated jets. If this cross talk adds a random shift to its momentum direction, the angular distribution should not change statistically.

Jet Invariant Mass

The invariant mass distributions of the two forward jets in 2-jet events (apart from the remnant jets) obtained by using different jet algorithms are compared in Figure 3.8 with the invariant mass of the two forward partons in the MC generated 2-parton events. The invariant mass of the jets in a 2-forward-jet event using the $k_\perp$ algorithm tends to be much smaller, while the invariant mass reconstructed by JADE tends to be larger. Arclus and the Ellis-Soper algorithms reconstruct the invariant mass fairly well.

Recall that in the Monte Carlo event generation, a lower limit was imposed to the invariant mass to avoid the divergences in the matrix elements calculation. This limit is the reason for the threshold in the parton invariant mass in Figure 3.8.

Separation Angle between the Jet Axes

Figure 3.9 shows the jet separation angle in 2-jet events reconstructed by various algorithms. The angle between the two generated partons is also shown for all 2-parton events. Again, the separation angle reconstructed by the $k_\perp$ algorithm is too small compared to the angle between the original partons. All other algorithms perform fairly well, especially JADE with $Y_{cut} = 0.04$ and the Ellis-Soper algorithm with $E_{Tcut} = 0.6\,GeV$.

Jet Momentum

Figure 3.10 to 3.12 show the momentum of the two forward jets and the momentum ratio of these two jets. The corresponding parton distributions are also plotted for comparison. The reconstructed momentum of the more energetic jet is lower than that of the parton, especially for the $k_\perp$ and Ellis-Soper algorithms. This is due to the fact that these two algorithms discard some of the final particle as the target remnant, so the remaining total momentum of an event is reduced. The reconstructed momentum of the less energetic jet in the Ellis-Soper and Arclus algorithms have a lower threshold because the algorithms impose transverse momentum cuts.

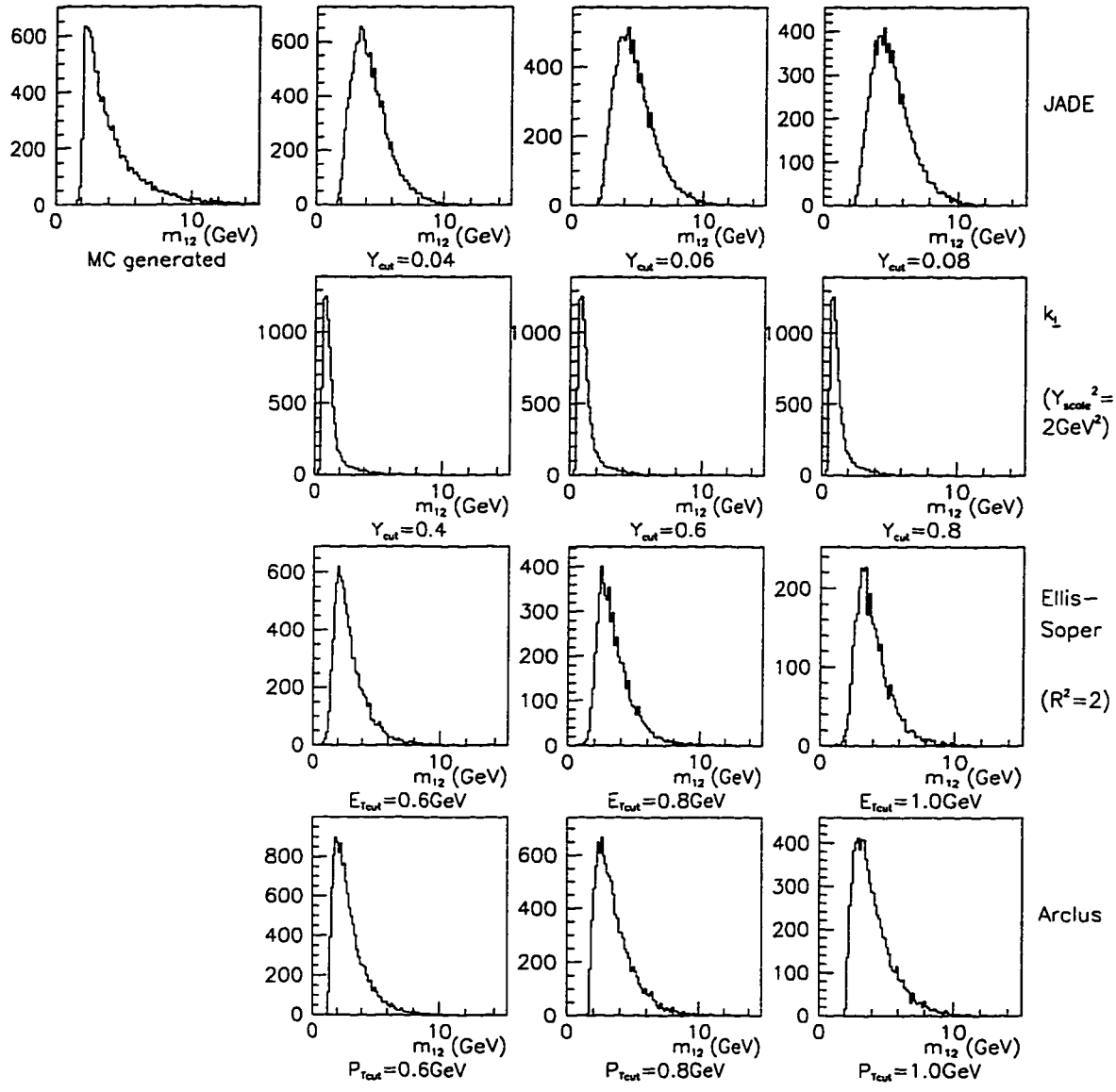

Figure 3.8: The invariant mass reconstructed in 2-jet events by different algorithms. The graph on the upper-left corner shows the invariant mass of the two generated partons in 2-parton events.

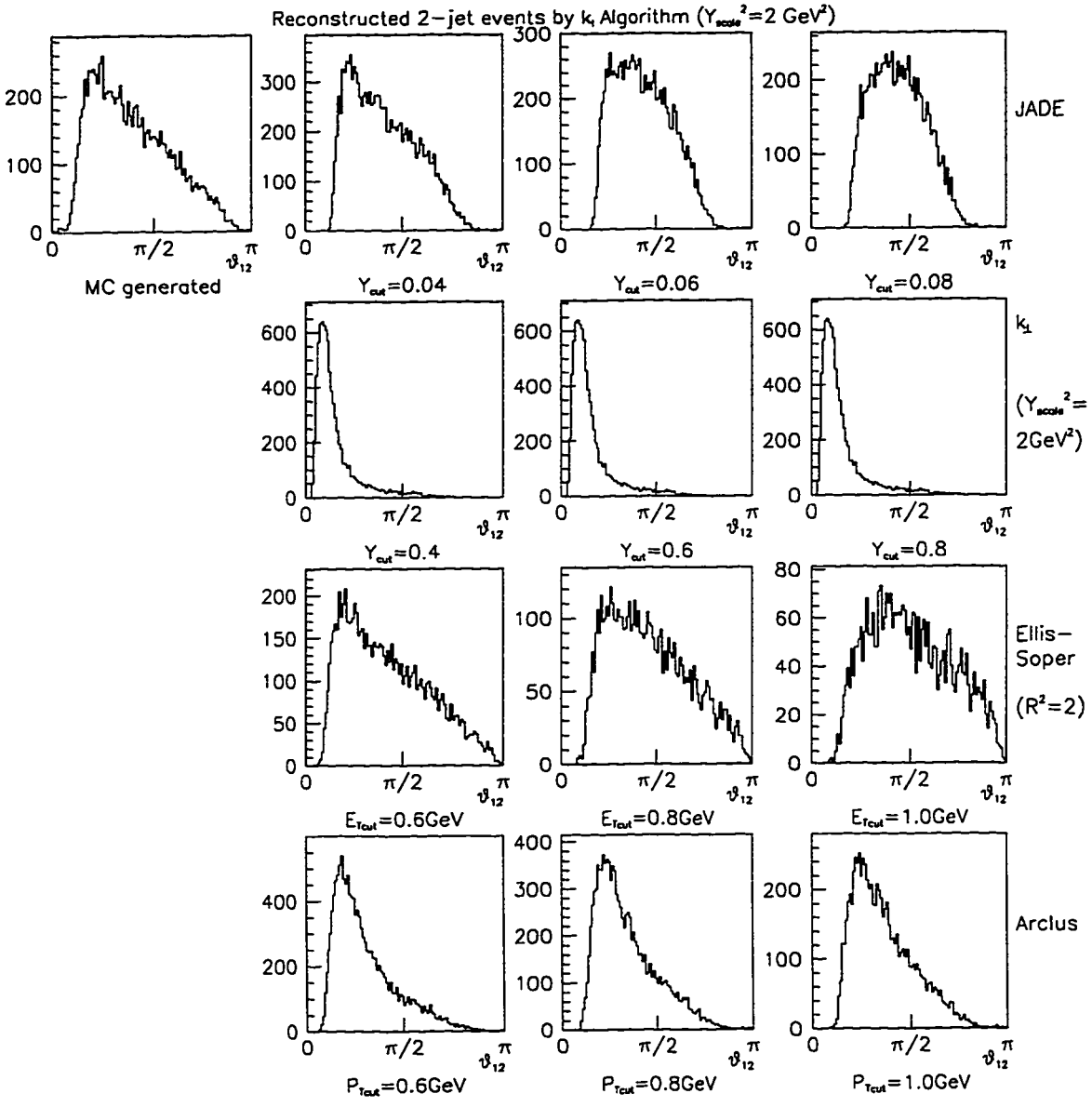

Figure 3.9: The separation angle between the two jet axes in 2-jet events.

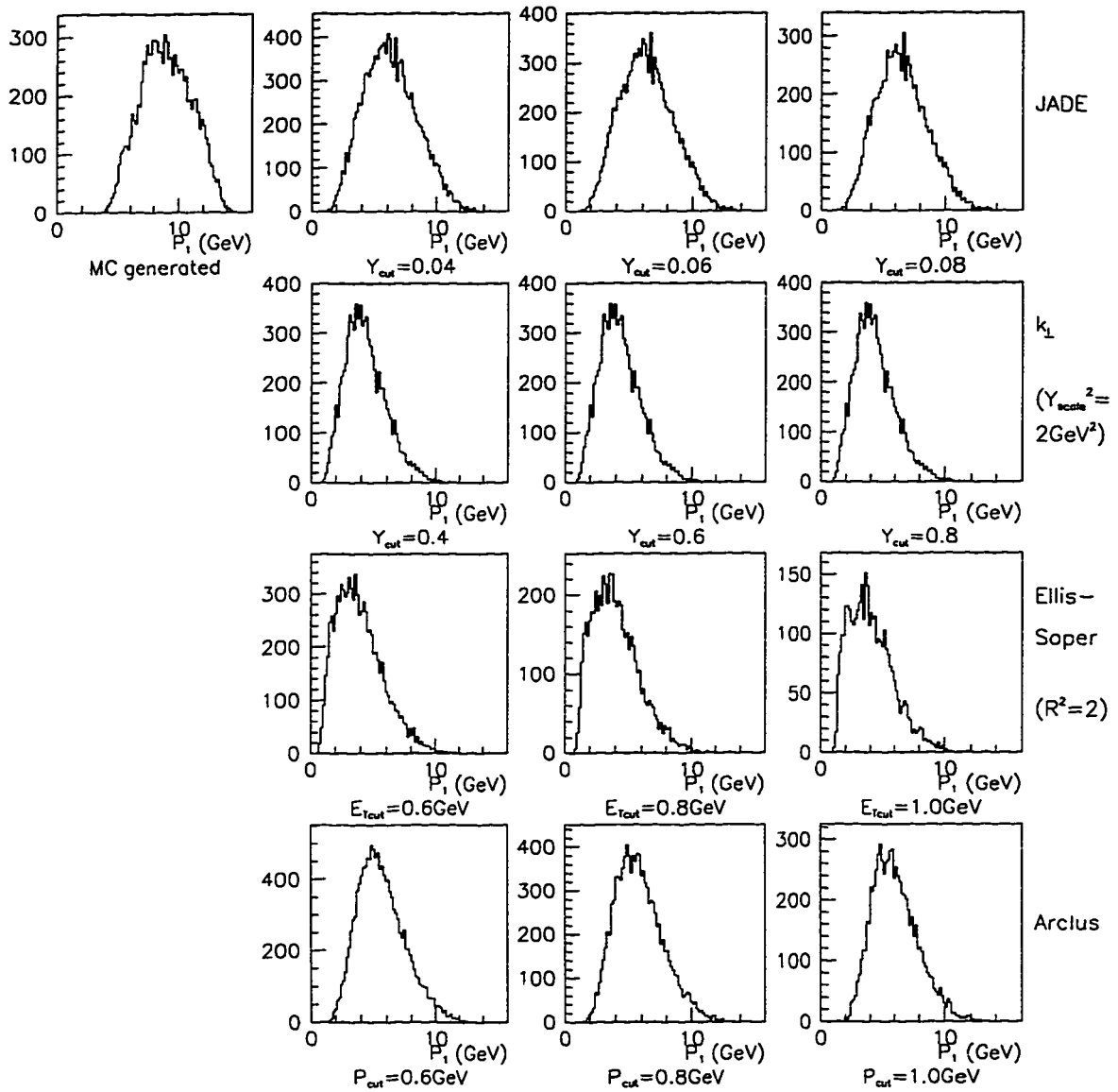

Figure 3.10: The momentum of the more energetic jet P_1 in 2-jet events.

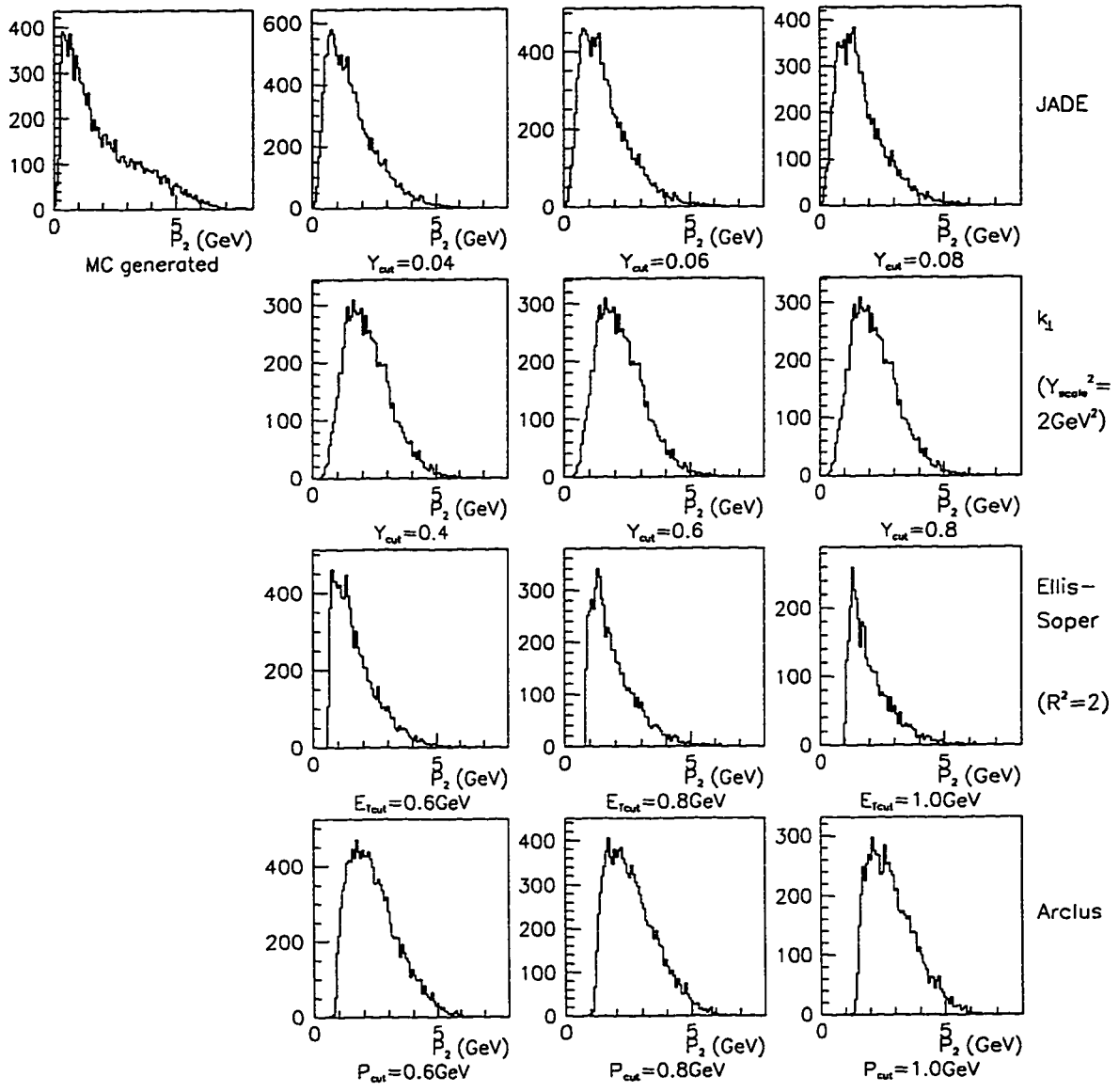

Figure 3.11: The momentum of the less energetic jet P_2 in 2-jet events.

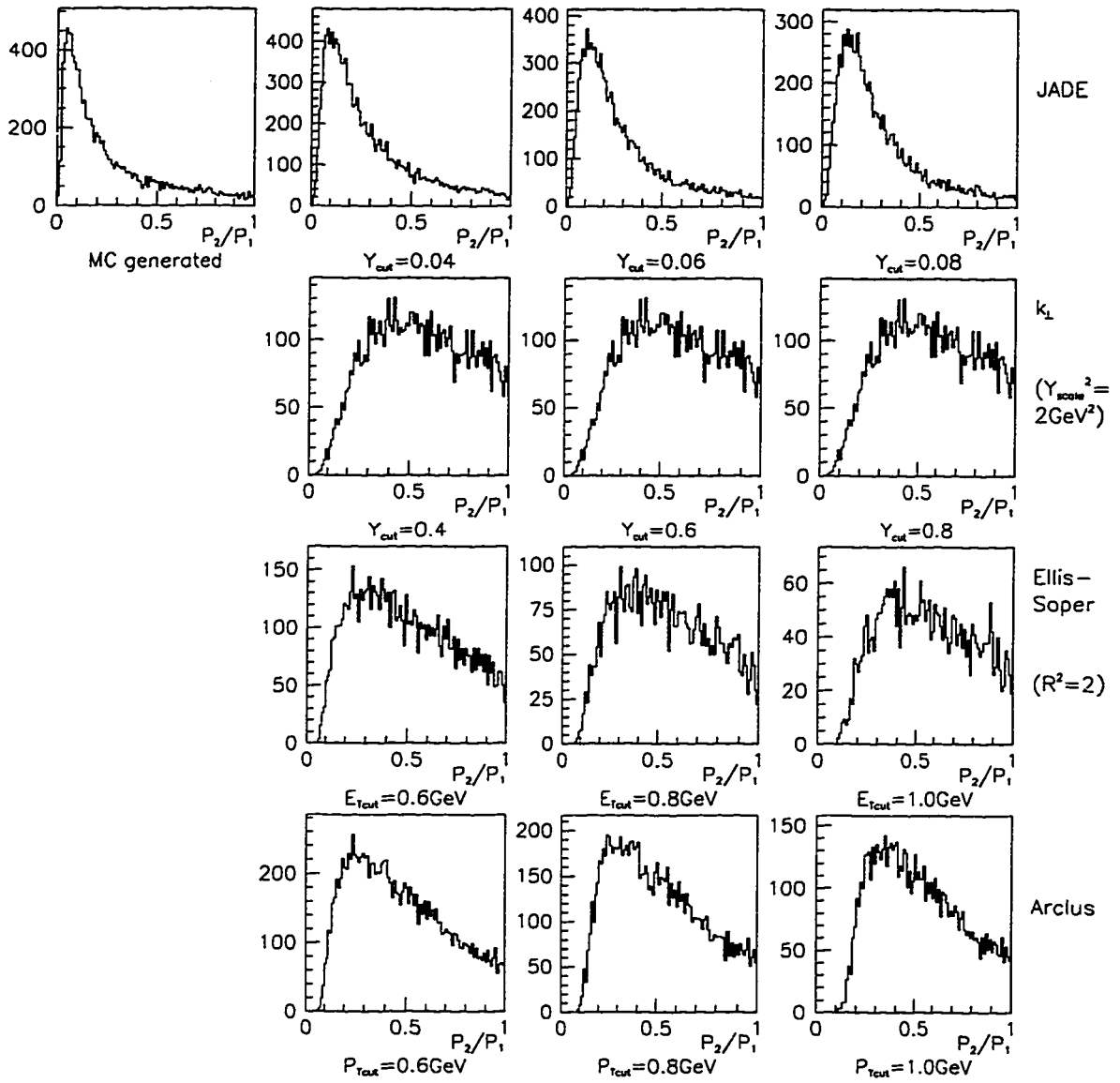

Figure 3.12: The momentum ratio P_2/P_1 of the two jets.

In the matrix elements calculation for the first order QCD cross section, one divergence is due to the 2-parton events having one parton with very low energy compared to the other. (Recall that an invariant mass cut was used at the parton level to regulate such divergences.) The result is that production of 2-parton events with highly asymmetric momenta is favored. Apparently, only JADE which also uses an invariant mass cut to reconstruct jets successfully reproduces this feature. All other algorithms also show an asymmetry in momentum, but not as extreme.

Jet Transverse Momentum and its Azimuthal Angle

Figure 3.13 and 3.14 show the transverse momentum distributions of the two forward jets in 2-jet events. The MC generated transverse momenta of the partons in 2-parton events are also plotted for comparison. Figure 3.15 and 3.16 show their azimuthal distributions.

The transverse momenta of the jets identified by the $k_\perp$ algorithm is smaller than those of the partons. The jet transverse momenta are bigger in both the Ellis-Soper and Arclus algorithms. This is because that there is a transverse momentum cutoff in these two algorithms as we mentioned earlier.

The reconstructed jets obtained by the $k_\perp$ algorithm do not reproduce the azimuthal distribution of the parton transverse momentum. All other three algorithms successfully reproduce this azimuthal distribution. The difference between the parton ϕ and the reconstructed jet ϕ is plotted in Figure 3.17. It is much smaller for the modified JADE and Ellis-Soper algorithms than the other two algorithms. The Ellis-Soper algorithm has the best agreement for ϕ distributions, although the number of events surviving the cuts is much smaller than using JADE. The small peak at about $\delta\phi = \pi$ is due to the large error in the momentum direction of the softer parton, especially when its momentum is less than 1 GeV.

3.4 Conclusion

For E665 and other fixed-target experiments with moderate center of mass energy, the various jet algorithms are not able to select pure first order QCD events. Nevertheless, the algorithms studied in this chapter, except for the $k_\perp$ algorithm which is also not very consistent with all other algorithms, are able to reproduce the QCD transverse momentum distributions and the azimuthal asymmetry. This is especially the case

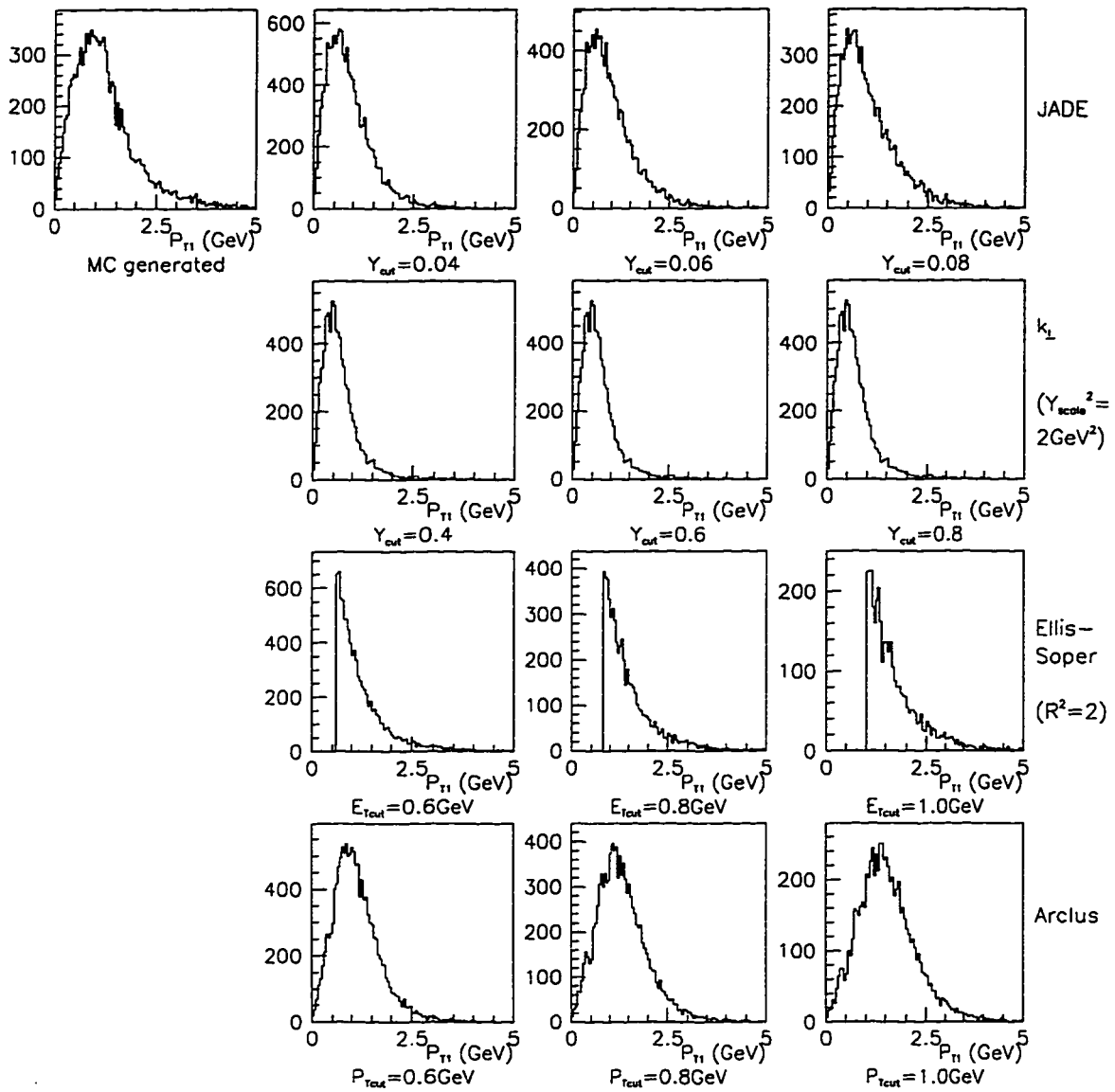

Figure 3.13: The transverse momentum of the more energetic jet in a 2-jet event.

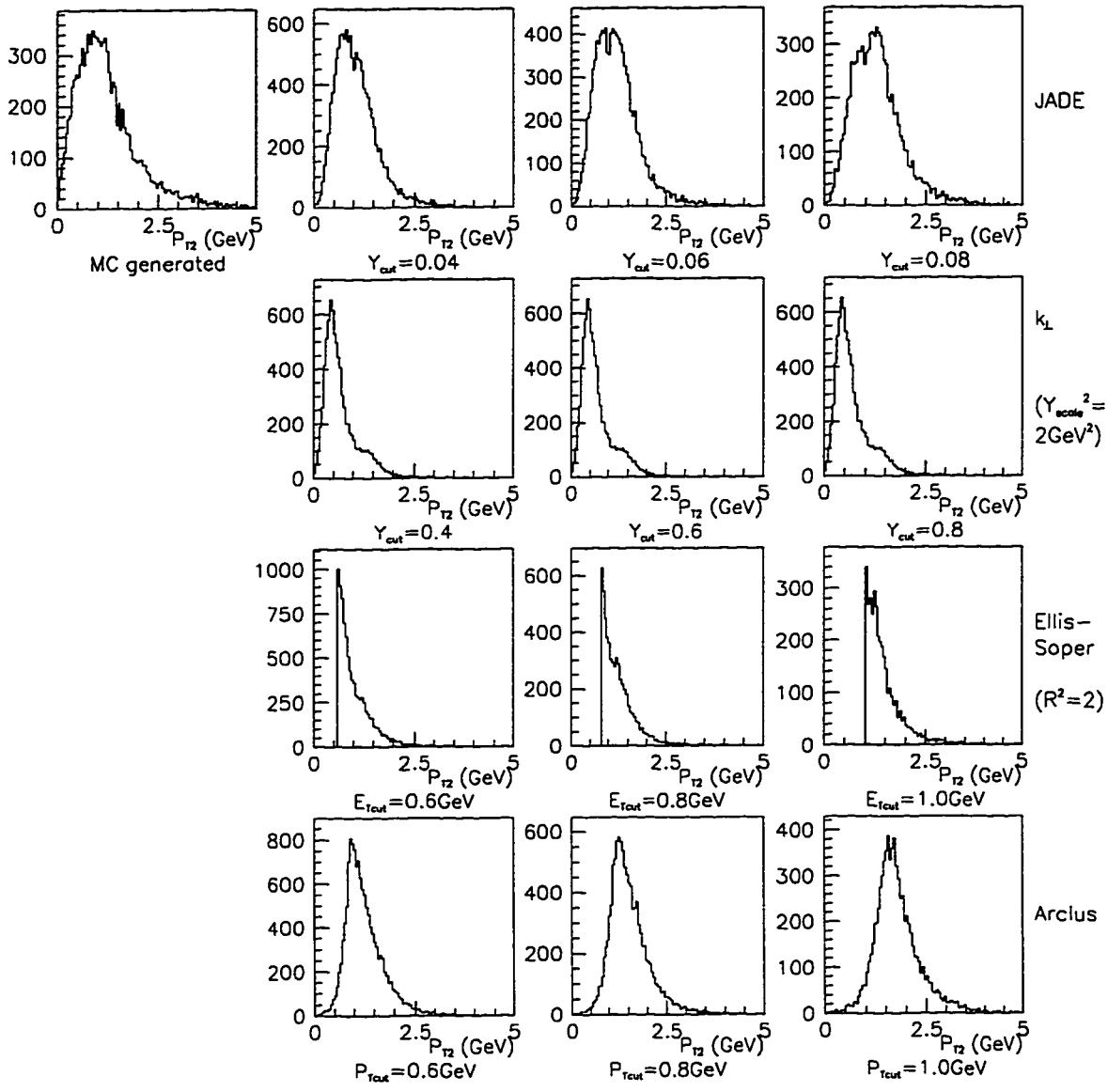

Figure 3.14: The transverse momentum of the less energetic jet in a 2-jet event.

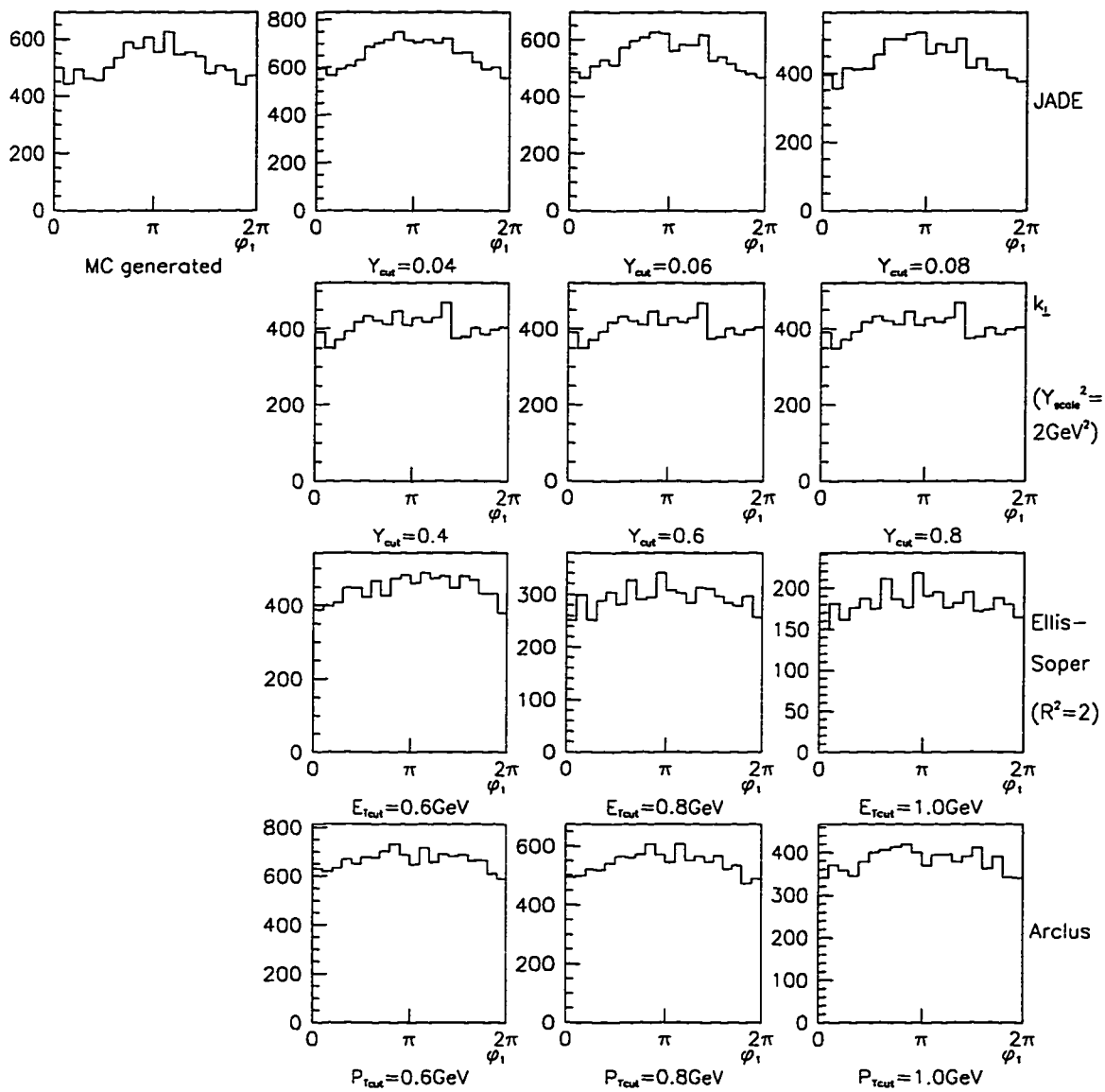

Figure 3.15: The azimuthal distributions of the transverse momentum of the more energetic jet.

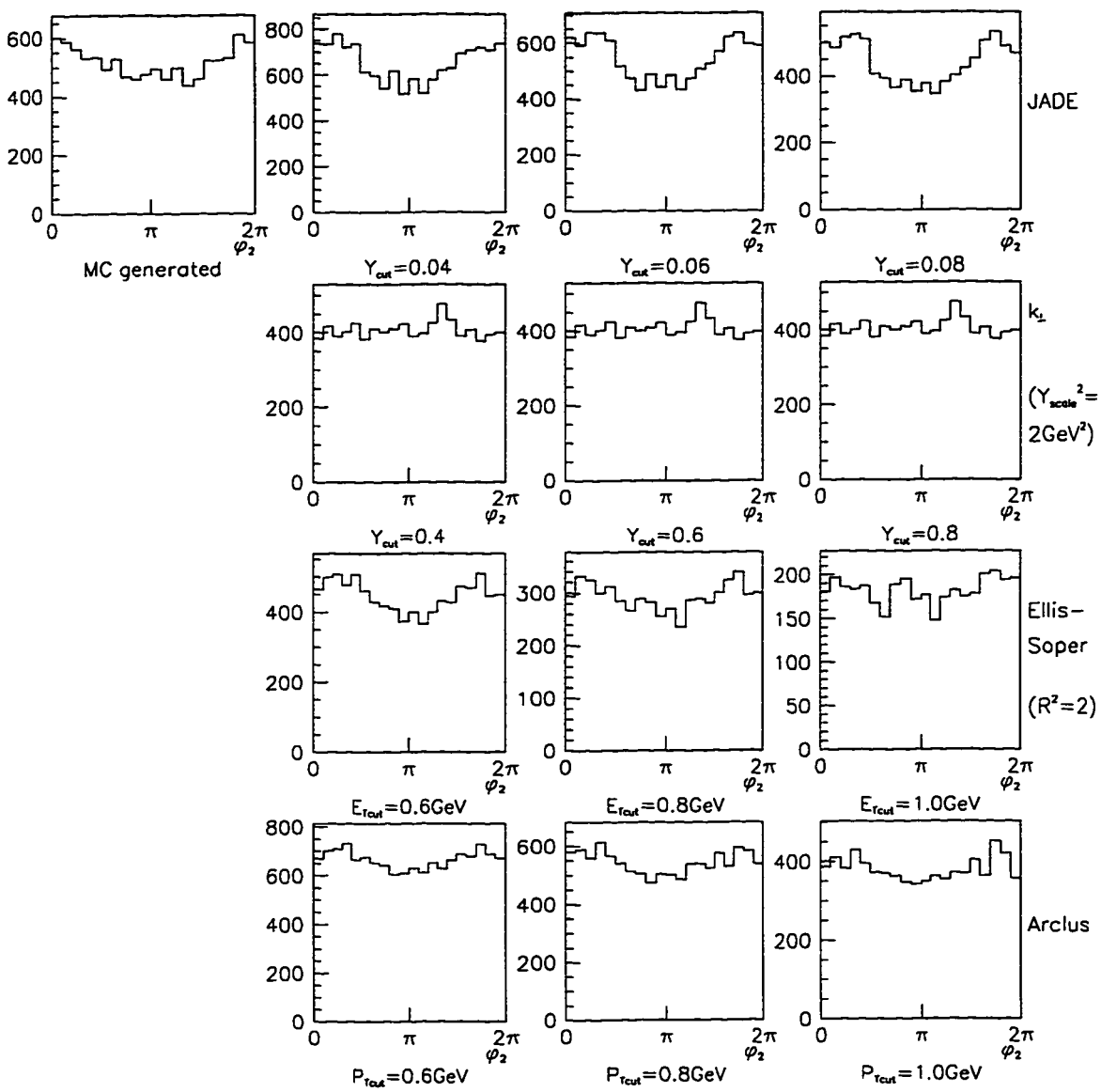

Figure 3.16: The azimuthal distributions of the transverse momentum of the less energetic jet.

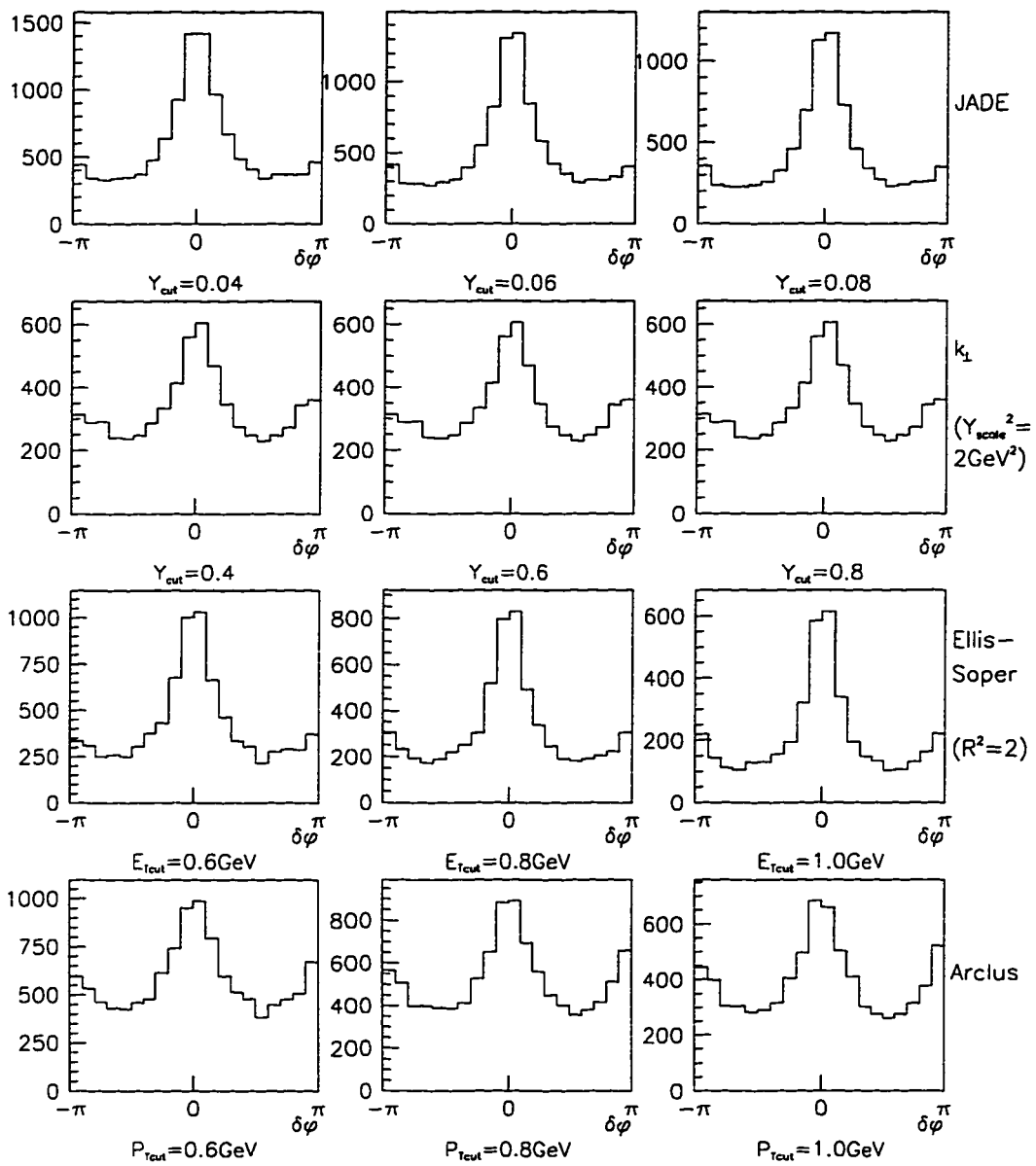

Figure 3.17: $\delta\phi = \phi_{parton} - \phi_{jet}$ for 2-parton events that are reconstructed as 2 jets.

for the modified JADE algorithm and the algorithm designed by Ellis and Soper. The reason that the $k_\perp$ algorithm does not reproduce the parton angular distribution well is probably due to the fact that in the Breit frame many very energetic particles detected in a fixed-target experiment are transformed to tracks carrying low energy and thus are identified as target remnants.

Using the modified JADE algorithm, Y_{cut} does not affect the ϕ distribution much. From the comparison of the jet separation angle distributions, $Y_{cut} = 0.04$ is better than larger Y_{cut} values. For experiments with larger center of mass energy, some P_T cut or large invariant mass cut can be used to help improve the purity of our 2-jet event sample. Using larger E_{Tcut}, the Ellis-Soper algorithm is able to select cleaner hard scattering events but the number of events surviving is significantly decreased. Using the E665 Monte Carlo data, $E_{Tcut} = 0.6\,GeV$ is better than other E_{Tcut} values for the momentum and jet separation angle distributions. For experiments of higher energy, this algorithm with higher E_{Tcut} is preferred.

In the remainder of this dissertation we will only consider the modified JADE algorithm at the E665 standard resolution cut $Y_{cut} = 0.04$ and the Ellis-Soper algorithm with $E_{Tcut} = 0.6\,GeV$. This cut is a compromise between good statistics and a clean sample. We will compare the results of these two very different algorithms in chapter 6.

Chapter 4

EXPERIMENT E665 AT FERMILAB

Fermilab experiment E665 was a fixed target muon scattering experiment with the highest energy available at the time. The E665 detectors resided in the New Muon Lab at the end of Fermilab's fixed target muon beamline [43].

4.1 Muon Beam

The muon beam is shown schematically in Figure 4.1. It has a total length of approximately 1.5 *km*.

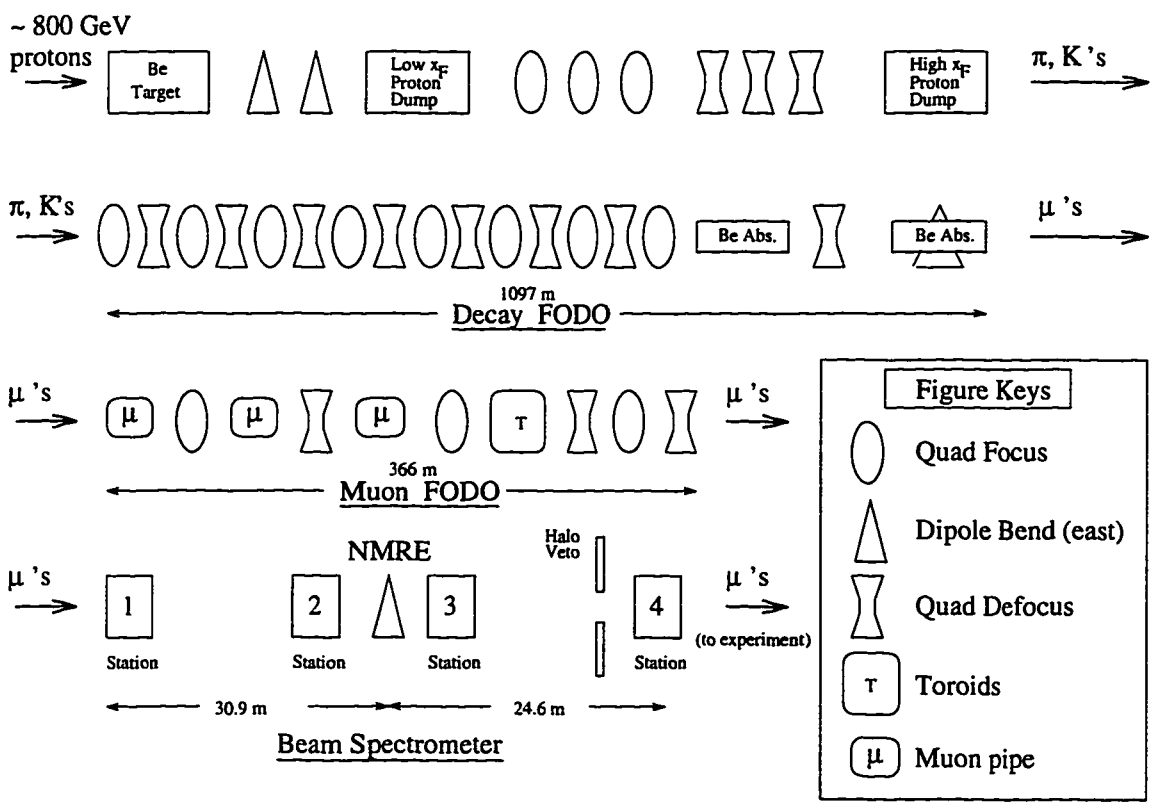

Figure 4.1: NM beam line, including the beam spectrometer

The proton beam extracted from the Fermilab Tevatron impinged on a target of $48.5\,cm$ of beryllium. Transmitted protons were separated from the secondary hadrons and were dumped in the absorbers. The pions (and kaons) were momentum selected and transported in a Focussing-Defocussing (FODO) channel. About 5% of the secondaries decayed to produce muons which remained in the FODO. The hadrons which did not decay were absorbed in a $11\,m$ long beryllium absorber, leaving only the muons to enter a second FODO channel in which the "halo" muons were reduced and then into the beam spectrometer. The incident muon flux could reach $> 2\times10^8$ muons per Tevatron cycle (59 seconds) in which the proton extraction lasted for 23 seconds (a spill). The final muon beam during the Fermilab fixed-target-run of 1991 (Run91) had a transverse size of approximately $4\,cm$ in Z and $6\,cm$ in Y direction, with an average energy approximately $470\,GeV$ and average intensity about 10^6 muons/sec.

The muon beam also preserves the $53.1MHz$ RF structure of the accelerator resulting in muons spaced at $18.8\,ns$ (an RF bucket) apart with a jitter of less than $1ns$. However about 20% of the occupied RF buckets contain more than one muon. These events can be identified both at the trigger level and at offline reconstruction.

An extensive discussion about the muon beam line can be found in reference [44]).

4.2 Beam Spectrometer

The beam spectrometer (as depicted in Figure 4.1) provided a fast trigger when a useful beam muon entered the experiment and the necessary information to reconstruct the muon momentum and trajectory. Four stations of six proportional multiwire chambers (PBT) with $1\,mm$ wire spacing and different orientations and a dipole magnet (NMRE) with $3\,mrad$ bend gave precise reconstruction of the beam track with angular resolution of about $10\,\mu rad$ and momentum resolution of $\Delta p/p \simeq 8\times10^{-6}p$ (corresponding to $2\,GeV$ uncertainty for a $500\,GeV$ track). Each station was equipped with scintillation counter hodoscopes (SBT) for the fast beam trigger and masking the hits in the PBT chambers.

4.3 Target

This thesis is based on the Run91 data. The target is assembled as in Figure 4.2. The length of the active target material was nominally $1m$ for the liquid targets: H_2 and D_2. Longer targets would gain significantly more statistics for muon cross-

section measurements, but the increased probability of secondary interactions is a disadvantage for hadron studies.

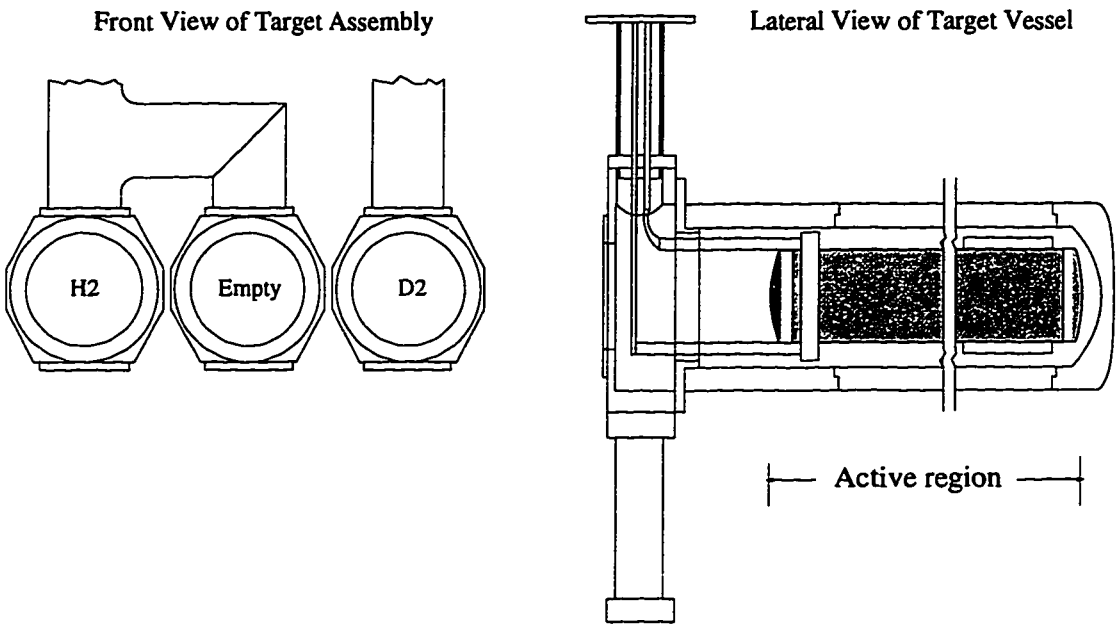

Figure 4.2: Cryogenic Liquid Target of E665 Run91

4.4 *E665 Forward Spectrometer*

4.4.1 Charged Track Detectors

Charged particle trajectories were determined by proportional and drift chambers in conjunction with two superconducting dipole magnets with opposite polarity, focussing at the absorber steel.

A vertex drift chamber (VDC) system was placed immediately downstream of the target inside the CERN Vertex Magnet (CVM). It provided precise measurements of low momentum tracks and improved vertex reconstruction. The 56 proportional multiwire chambers and DC planes achieved a momentum resolution of $\Delta p/p = 2 \times 10^{-5} p$, or 1.0% at $500\,GeV$ for forward tracks that spanned the whole length of the spectrometer. CVM was run with $\int \vec{B} \cdot d\vec{l} = 4.3\,Tm$ (Tesla-meters) and gave a 1.293 GeV transverse momentum kick. The Chicago Cyclotron Magnet (CCM) gave a 2.019 GeV kick in the opposite direction (-6.7 Tm). This configuration improved our momentum resolution as well as the resolution of scattering angles.

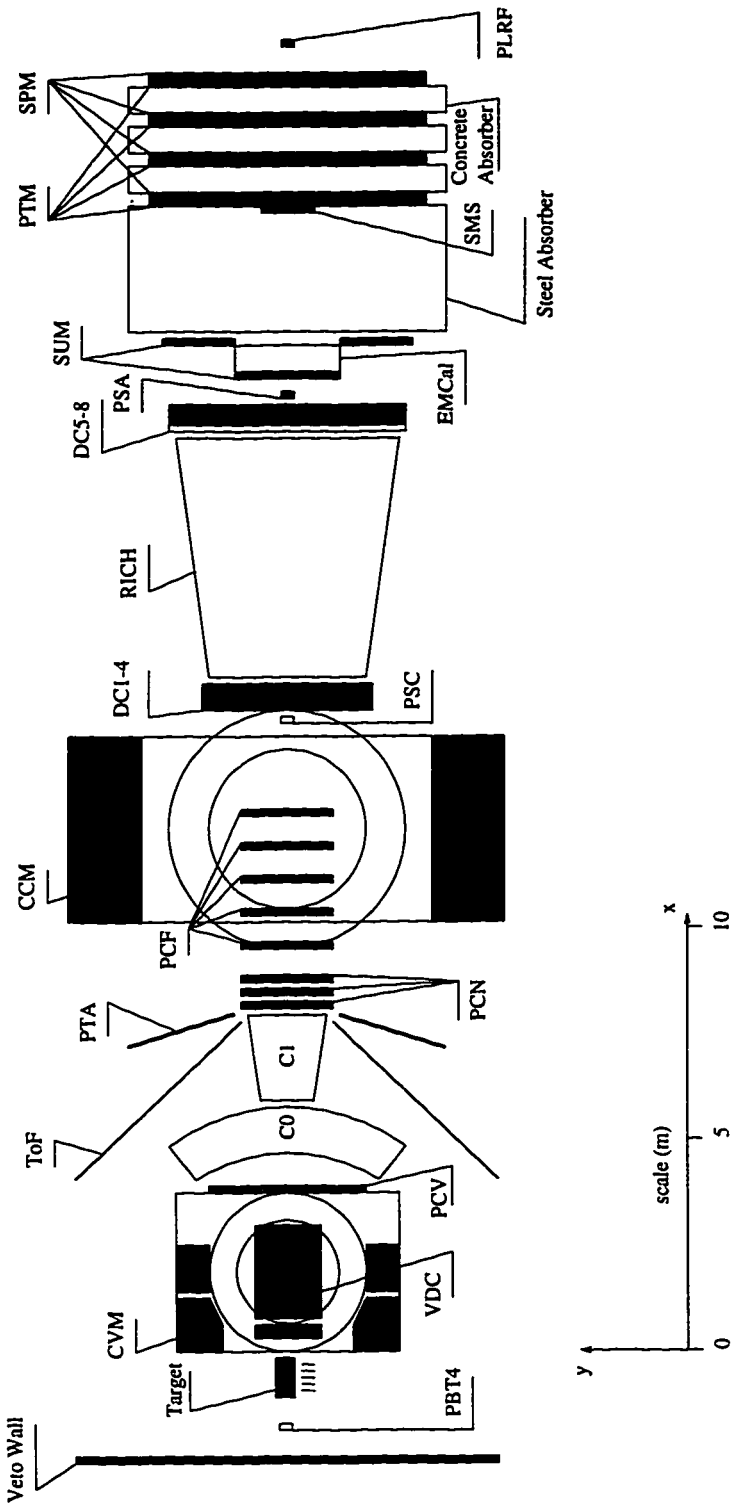

Figure 4.3: E665 forward spectrometer

4.4.2 Muon Detectors

Downstream of the forward spectrometer was a 3 m steel absorber (about 18 interaction lengths and about 170 radiation lengths) which stopped all particles but muons. Four layers of muon detectors (proportional tubes + scintillator), separated by concrete absorbers that stopped shower particles, provided accurate information of muon tracks. Various hodoscopes were used to provide fast beam trigger signals and veto halo muons.

4.4.3 Calorimeter

Photon detection and energy measurement was provided by an electromagnetic calorimeter. The EM calorimeter material is lead and the detectors are proportional planes with cathode pad read-outs. There are twenty planes of one radiation length thick $3m \times 3m$ lead plates interspersed with twenty wire chamber planes. The chambers have alternately Y and Z wires with 1 cm wire spacing. In four of the planes at about the shower maximum the wires are read-out individually in the 1 m region around the center of the detector and in pairs in the outer regions. The cathode planes were split into 1188 pads, and read out as towers summed over all planes. The pad size is $4\,cm \times 4\,cm$ in the central 1 $m \times$ 1 m of the detector, $8\,cm \times 8\,cm$ between $0.5\,m$ and 1 m from the center, and 16 $cm \times$ 16 cm in the outer region. The output of the cathode pads is summed by electronics external to the calorimeter. This keeps the speed of the output pulses as fast as possible ($400\,ns$ gate widths for the prototype).

The energy resolution is $\sigma_E = 38\%\sqrt{E}$, where the energy E is in units of GeV [46]. The spatial resolution using the individually read-out anode wires is 0.3 cm per plane. A spatial resolution of about 0.5 cm can be reached in the case of isolated photons or electrons. Separation of shower centers greater than 4 or 5 cm apart is possible. Although spatial resolutions depend on energy, it is also possible to separate π_0/γ up to about 100 GeV.

Chapter 5

DATA SELECTION AND CHARACTERISTICS

This analysis is based on the Run91 data of E665 which was collected in the year 1991.

5.1 Event Selection

To ensure the data only consist good DIS samples, the following selection criteria were adopted.

5.1.1 Beam Selection

- The reconstructed momentum is between 350 and 650 GeV.
- The run number must be between 21350 and 22080 or between 22120 and 22450 for which the chamber efficiencies are high (see page 185 of reference [46]).
- One and only one in-time beam track. This simplifies the reconstruction of the primary muon-muon vertex.
- Number of hits to reconstruct a beam track is at least 10. Unused PBT hits is less than 19, and at least 6 hits from 7 SBT scintillators. These criteria ensure the accuracy of the momentum measurement.
- The χ^2 probability of the beam track is greater than 0.001.
- The beam passed through the target fiducial region. This could be checked by extrapolating the track in a straight line from the most downstream beam station (PBT4) to the upstream and downstream ends of the target ($X = -13\,m$ and $-12\,m$). On both ends, the transverse position of the beam track has to be within 4.6 cm of the longitudinal target axis. This ensures the beam traverses the full length of the target material.

5.1.2 Scattered Muon Selection

- The reconstructed momentum is greater than $100\,GeV$. This makes the muon mismatch probability negligible and reduces the radiative corrections. It also reduces muon multiple scattering in the hadron absorber.

- Muon energy loss ν is greater than $100\,GeV$, and the fractional error of the reconstructed ν is less than 0.05, i.e. $\delta\nu/\nu < 0.05$. The ν cut also eliminates the straight-through beam track contamination.

- The scattered muon tracks have a total of 10 more more hits and at least 2 hits in the PTM. This ensures a long lever arm, hence good resolution.

- No hits on SMS or SSA (trigger small angle veto signal), SVS (triggers large angle veto signal) and PSA. These criteria ensure a larger scattering angle and also avoid most detectors' central dead regions.

- The χ^2 probability of the scattered muon tracks must be greater than 0.001.

- The primary vertex must be reconstructed in the target fiducial region. This eliminates the scatterings out side the target. Due to the smearing effect, we loosen this cut on x position of the vertex by half a meter at each end of the target to $[-13.5m,\ -11.5m]$.

A example of how well x_{Bj} is measured in E665 data can be demonstrated using muon-electron scattering events. A μe event can be isolated using the following cuts:

- Same criteria for incoming beam and the scattered muon tracks.

- One and only one negative track found in forward spectrometer that can be fitted to the primary vertex. The χ^2 probability of this track has to be greater than 0.01, and its energy should be greater than 85% ν.

- The negative fitted track should create an energy cluster within $5\,cm$ of its position in the calorimeter. This ensures that it is an electron track.

- No unphysical kinematics nor unphysical track momenta.

- Q^2 is greater than $0.1\,GeV^2$

The x_{Bj} distribution shows a clear peak with the fit to a Gaussian giving a mean at $(5.450 \pm 0.005) \times 10^{-4}$. Using the Particle Data Group (PDG) values of $m_e = 0.51099906 \pm 0.00000015\,MeV$, and $m_p = 938.27231 \pm 0.00028\,MeV$, we obtain for μe scattering (up to radiative corrections) $x_{Bj} = m_e/m_p = 5.446170 \times 10^{-4}$ We conclude that our measurement of the variables at the lepton vertex is very precise.

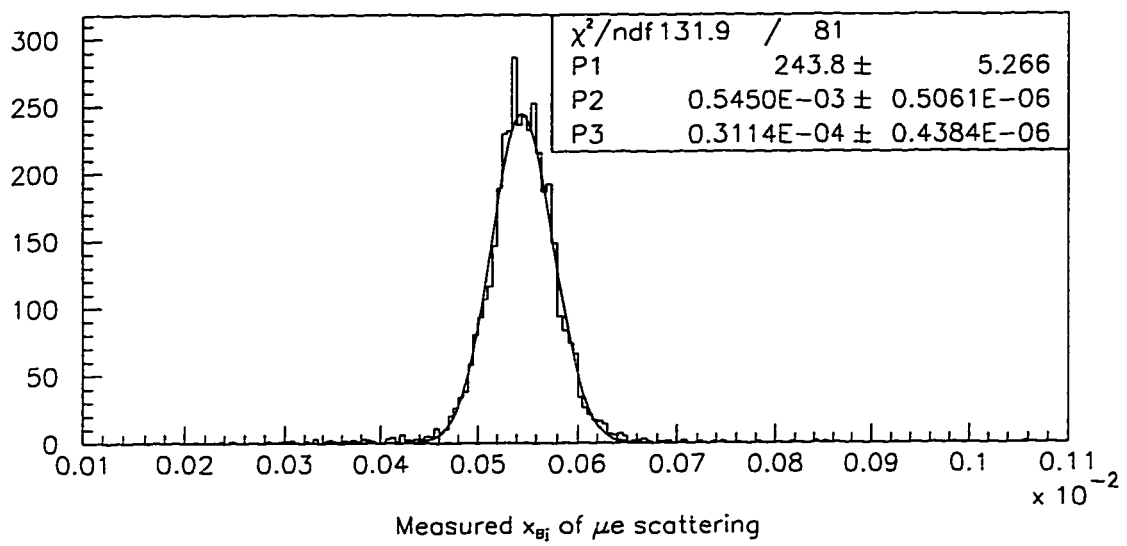

Figure 5.1: Measured x_{Bj} of μe scattering events.

5.1.3 Kinematics Cuts

$$
\begin{aligned}
Q^2 &> 3\,GeV^2 \\
W &> 15\,GeV \\
\delta Q^2/Q^2 &< 0.02 \\
\delta\nu/\nu &< 0.05 \\
x_{Bj} &< 0.003 \\
0.1 < y_{Bj} &< 0.85
\end{aligned}
$$

5.1.4 Additional Event Cuts

- Only one muon track in the forward spectrometer. Although this requirement also eliminates decays of hadrons into muons, it eliminates the possibility of confusing the decay muon with the scattered muon. Only 5.6% of the total reconstructed events had decays to muons, according to a study of 3000 Monte Carlo events (see page 68 of reference [45]).

- No unphysical kinematics nor unphysical particle parameters.

- There is at least one fully reconstructed charged hadron track attached to the primary muon vertex. The number of final particles of any event has to be greater than 3. This also reduce the radiative DIS events.

- Total visible energy E_{total} is in the range of $0.3 < E_{total}/\nu < 1.1$, which limits the missing energy.

5.1.5 Radiative Cuts

Radiative cuts are event cuts to reduce the contamination of the radiative DIS events.

Muon Bremsstrahlung

The muons in a deep inelastic scattering may also radiate a photon before or after the gauge boson is exchanged (see Figure 5.2). This results in the following two problems.

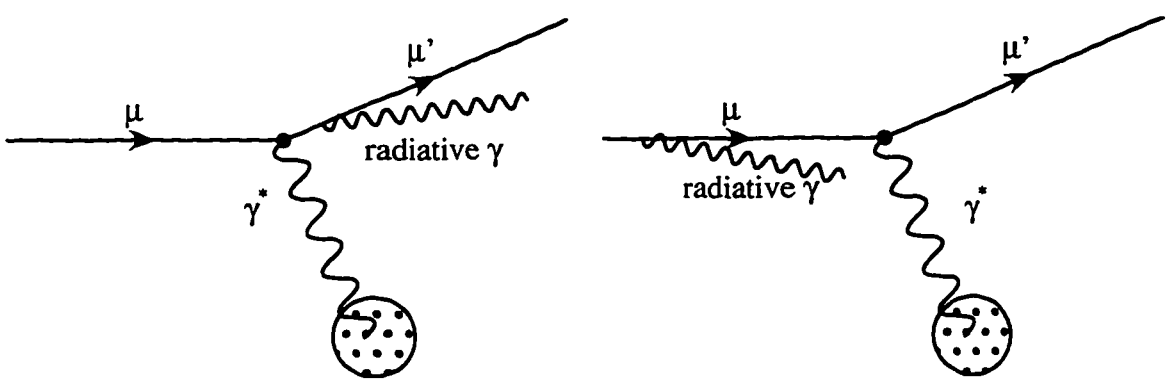

Figure 5.2: First order radiative events

1) The kinematics will be calculated incorrectly (see Figure 5.3). The energy of the virtual photon ν is calculated as the energy difference between the outgoing muon and the incoming muon. Therefore, if the scattered muon radiates an extra photon, the calculated ν will be the true ν + the energy of the radiative photon.

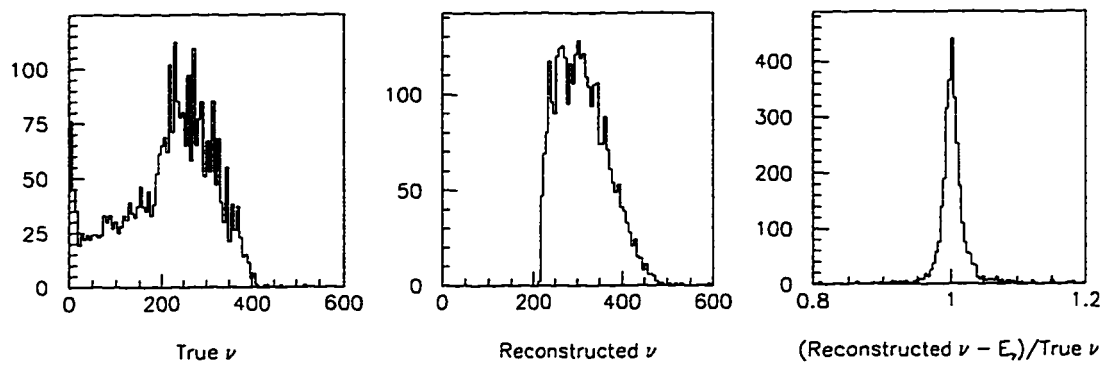

Figure 5.3: Reconstructed ν when the muon radiates a photon (after a cut of 200 GeV^2 on the reconstructed ν of Monte Carlo data). The miss-reconstructed value in ν is centered around the energy of the radiative photon E_γ.

2) The radiated photon tends to be soft or collinear with the muon. This may alter the azimuthal angle distribution. See Figure 5.5 for the angles between the radiative photon and beam track and also the scattered muon track for the Monte Carlo data which satisfied the same event cuts discussed above. In comparison, the closest angles of the reconstructed photons in the non-radiative Monte Carlo events are plotted assuming the photons are the decay products of π^0's which decayed at the primary vertex.

In order to minimize the contamination of the radiative events, we require:

- No photon cluster of energy is greater than 0.4ν. According to Monte Carlo studies, this rejects approximately 14.5% of the radiative events, but only about 3.2% of the non-radiative events.

- No photon cluster is within 0.0025 radians with respect to the beam track, or 0.005s radian with respect to the scattered muon track in the lab frame. This further reduces the Monte Carlo radiative events by another 32.1%, while rejecting only about 6.0% of clean DIS events.

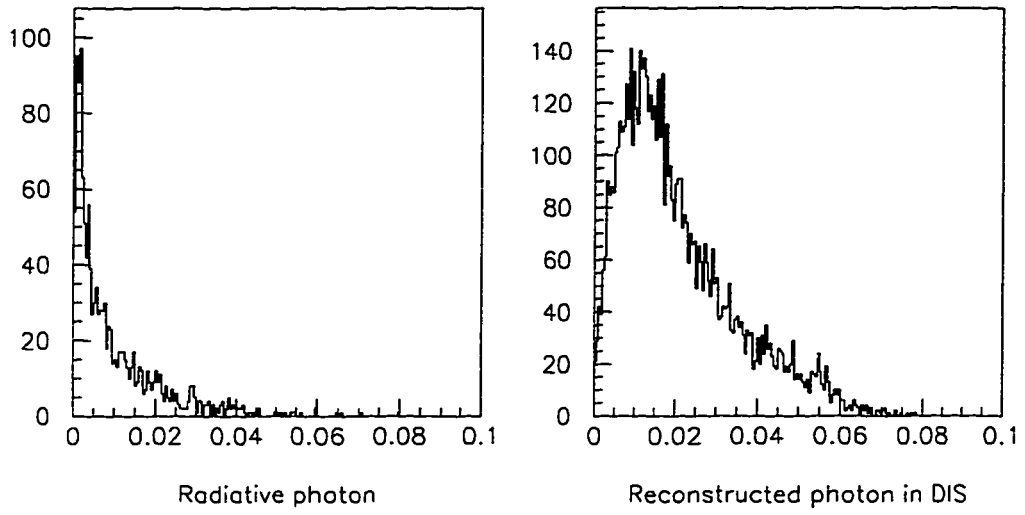

Figure 5.4: The closest angle between the reconstructed photons and the beam track in a Monte Carlo event.

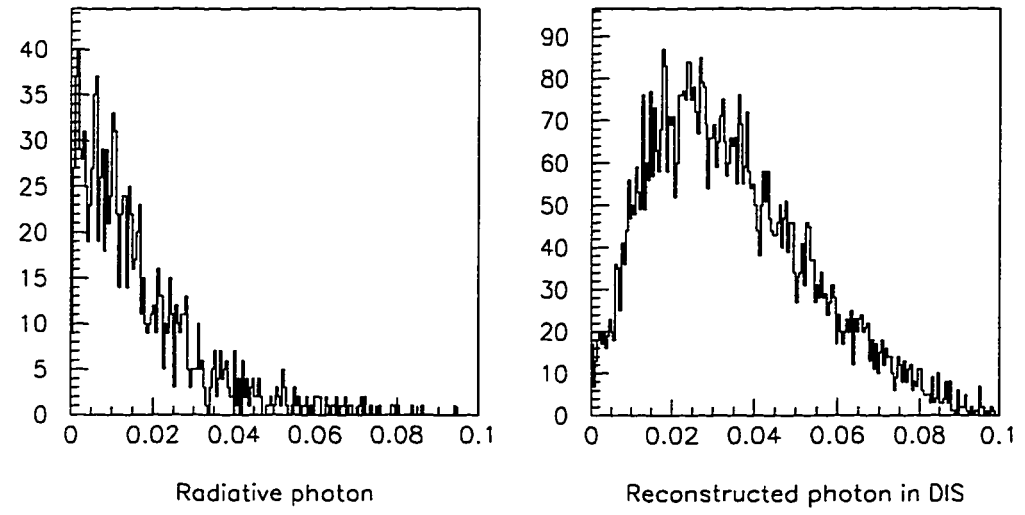

Figure 5.5: The closest angle between the reconstructed photons and the scattered muon track in a Monte Carlo event.

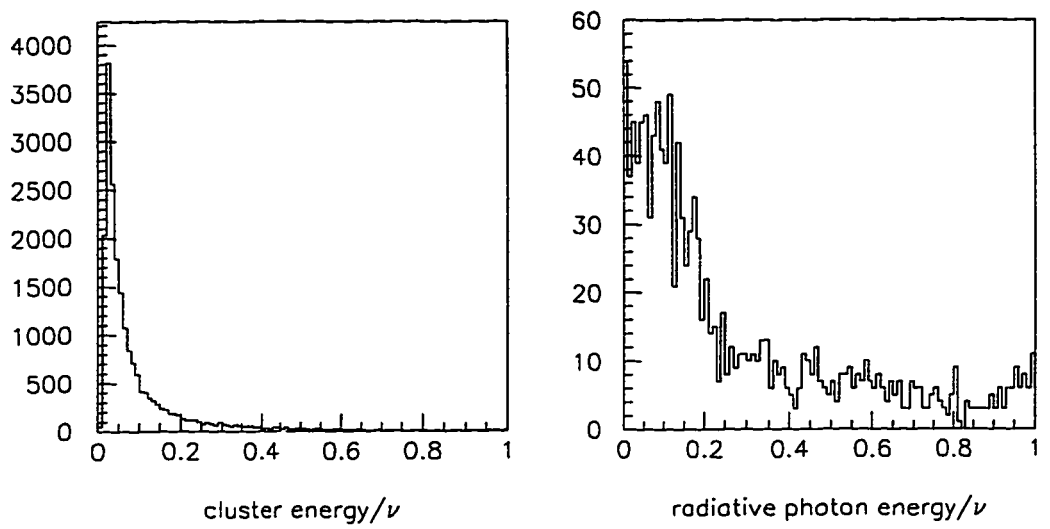

Figure 5.6: The photon energy in comparison to the reconstructed ν in non-radiative DIS events and in radiative events respectively.

- The total photon energy deposited in the calorimeter $E_{cal}/\nu < 0.5$

Here the so-called photon clusters have passed the photon selection, which will be addressed in the next section. Before these cuts, about 16.6% of the total Monte Carlo jet sample consisted of radiative events. After these radiative cuts, about half of the radiative events are removed.

Among the remaining events, the transverse momentum of the photon clusters is plotted in Figure 5.7. The following requirement further reduces the radiative events by about 33%, while only rejecting about 2% of clean DIS events. After all these cuts about 8% of the remaining MC events contained radiative photons. These radiative photons have low energies and low transverse momenta, and therefore do not affect our final analysis significantly.

- No calorimeter cluster with transverse momentum p_T which satisfies $(p_T - 0.2\,GeV)/\theta_\mu > 2\,GeV$, where θ_μ is the angle between the photon momentum and the muon track in CMS.

Correction to the Jet Azimuthal Distribution for Radiative Events

After collecting particles into jets, the influence of the remaining radiative events is very small. A bin-to-bin correction for the jet azimuthal distribution will be made to

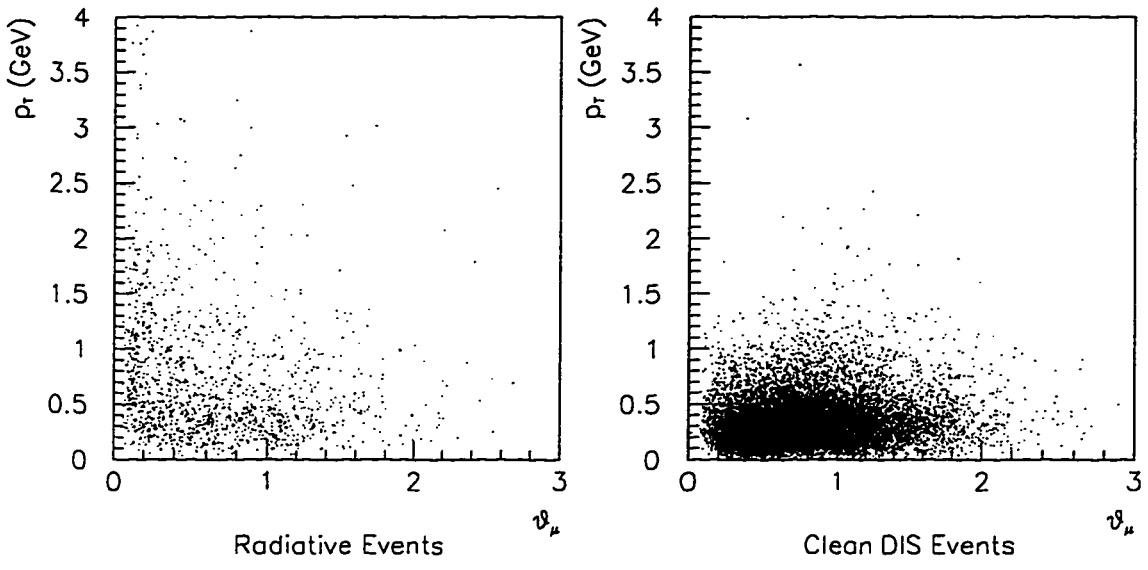

Figure 5.7: The photon cluster's transverse momentum p_T vs. the angle between the photon track and the muon tracks θ_μ in CMS.

the experimental data.

5.2 Charged Track Selection

- Only final particles. Do not count both the parent particle and its daughter particle.

- For track reconstruction a minimum of 3 hits is required, and χ^2 probability has to be greater than 0.01. This ensures a better reconstruction of the track momentum.

- No partially reconstructed close tracks. If the distance between a track and its closest vertex is less than $1.0\,cm$, it is called "fitted", if not it is called "close". This also removes most ghost tracks, or random collection of hits, which could be hits left over from the previous event. Since the ghost tracks are random, the chance for them to be attached to a vertex is small. The likelyhood that in addition a PCF or DC hit is associated with this vertex is almost zero.

- Other standard E665 track cuts

$$\begin{aligned} D &< 5.0\sigma \\ \delta P/P &< 0.05 \end{aligned}$$

  where D is the minimum distance of approach to the vertex, σ is the error, and P is the track momentum. These cuts effectively eliminate most close tracks.

A pion mass (139.56995 MeV) is assigned to every detected charged particle. A Monte Carlo study showed that charged kaons, electrons and protons actually represent 6.8%, 4.1% and 1.5% of the charged particle sample, respectively (see page 72 of reference [45]). Therefore Monte Carlo corrections for the true masses are reasonably small.

5.2.1 Calibration using K_s^0 Mass Measurement

We measured the K_s^0 mass using the same data sample with looser x_{Bj} and y_{Bj} cuts. The branching ratio of $K_s^0 \to \pi^+ + \pi^-$ is $68.61 \pm 0.28\%$.

The following cuts were used to obtain a clean sample of K_s^0:

- There exists a secondary vertex which has two and only two fitted forward tracks with opposite charges. This vertex is not attached to any other charged track. The topology reassembles a neutral particle decaying into two oppositely charged particles.

- The two tracks satisfy the requirement discussed in this session.

- The momentum sum of the two forward tracks has to be consistent with the direction of the vertex position. In other words, if we compute the K_s^0 momentum orientation θ_K and ϕ_K using the primary muon-muon vertex as the origin, and we also compute the orientation of the 3-vector momentum θ_p and ϕ_p by summing up the momentum of the two forward tracks, we require:

$$\begin{aligned} |\theta_K - \theta_p| &< 20^\circ \\ |\phi_K - \phi_p| &< 20^\circ \end{aligned}$$

- We further require that the K_s^0 vertex be outside the target in order to avoid multiple scattering in the target.

- If both tracks are assigned with the electron mass, the invariant mass has to be greater than $0.1\,GeV$. This eliminates the contribution of photon conversion: $\gamma \rightarrow e^+e^-$.

We assign a pion mass to each track and calculate the pair invariant mass which is plotted in Figure 5.8. A very narrow peak in the plot is obviously due to the K_s^0

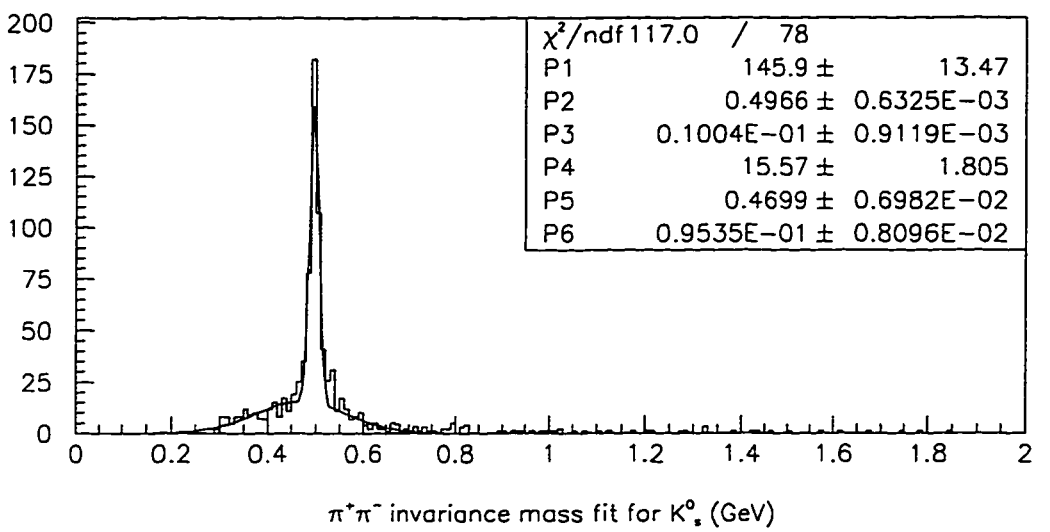

Figure 5.8: $\pi^+\pi^-$ invariant mass distribution for events satisfying the K_s^0 vertex topology. P1,...,P6 are fit parameters for a sum of two Gaussians.

signal. The background could be due to other neutral particle decays and inaccuracy in momentum measurement. A sum of two Gaussians is used to fit the data. Fit parameters P1,P2 and P3 are the normalization, mean and sigma of the sharp peak, respectively. P4, P5, and P6 are the corresponding parameters for the background. The fitted mean is $496.6 \pm 0.6\,MeV$, which is about $1\,MeV$ lower than the value published by the PDG for the neutral kaon ($497.672 \pm 0.031\,MeV$ [48]). It is suggested in reference [51] that this mass shift came from the a shift of $0.40 \pm 0.14\%$ lower in the B field of the CCM. We can calibrate our momentum measurement of charged tracks to better agree with the PDG value. If we scale all the momenta by 1.003 and repeat the same analysis, we find the fitted mean to be $497.7 \pm 0.6\,MeV$, in excellent

agreement with PDG. From now on, a scaling factor 1.003 will be used to correct all the charged track momenta.

5.3 Calorimeter Photon Cluster Selection

The dominant "noise" source in Run91 came from the beam energy loss in the calorimeter. About 20% of the beam triggers have at least one cluster, concentrated in the central beam spot, which is about $10\,cm$ high and $25\,cm$ wide. Of these beam-induced clusters, 99% have energy less than $5\,GeV$. Therefore, we have to remove these low energy clusters. On the other hand, see Figure 5.9, the calorimeter responds poorly to momenta of around $5\,GeV$. According to a Monte Carlo study [45], 16% of

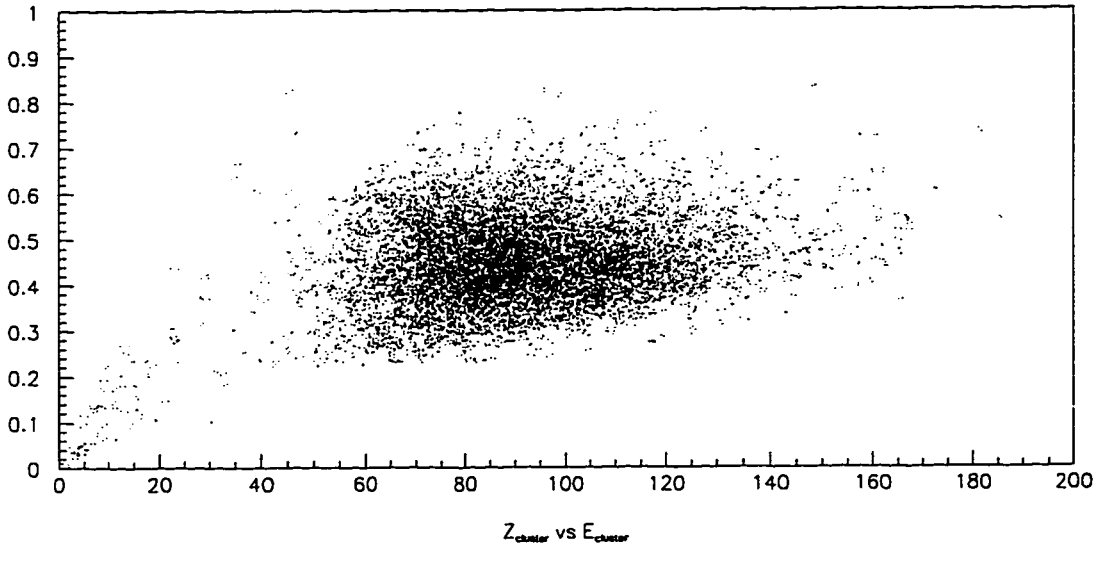

Figure 5.9: Poor response to low energy electron track in μe scattering events. $Z_{cluster} = E_{cluster}/E_{calibration}$. $E_{calibration} = (\nu + P)/2$ where P is the energy of the electron track.

all photons from pion decays have energy less than $5\,GeV$ and would be cut from the analysis. Because of the low momentum, the final jet momentum distribution using Monte Carlo data with and without this energy cut showed no statistical difference [45].

The Calorimeter also responds to charged tracks, especially to electrons and positrons. Therefore, for a cluster to be called a photon, there must not be a charged track within a minimum distance.

In conclusion, the following requirements are used to select photons:

- The Y and Z coordinates of the cluster have to be in the range of $[-1.5\,m, 1.5\,m]$ (inside the calorimeter).
- Cluster energy $E_{cluster} \geq 5\,GeV$.
- No track within 5, 7, $10\,cm$ for the inner ($Y, Z \in [-0.5\,m, 0.5\,m]$), middle ($Y, Z \in [-1.0\,m, -0.5\,m) \cup (0.5\,m, 1.0\,m]$) and outer ($Y, Z \in [-1.5\,m, -1\,m) \cup (1.0\,m, 1.5\,m]$) regions [45].

5.3.1 Calorimeter Cluster Energy ($E_{cluster}$) Parameterization

The energy of all the calorimeter clusters that survived the photon cuts are corrected using A. Kotwal's $E_{cluster}$ Parameterization (Appendix D of reference [46]).

If we define run number $NRUN$, then the run dependence $RUNDEP$ shall be calculated as:

$$
\begin{aligned}
21600 > NRUN > 21000 \quad &: \quad RUNDEP = 1.121 - 0.0002875 \times (NRUN - 21000) \\
22200 > NRUN > 21600 \quad &: \quad RUNDEP = 0.919 + 0.0003160 \times (NRUN - 21600) \\
22800 > NRUN > 22200 \quad &: \quad RUNDEP = 1.098 - 0.0004019 \times (NRUN - 22200) \\
E_{corrected} \quad &= \quad E_{cluster}/RUNDEP
\end{aligned}
$$

The corrected $E_{corrected} = E_{cluster}/B\sum A_n X_n$ where

$$
\begin{aligned}
X_0 &= 1.0 \\
X_1 &= E_{cluster} \\
X_2 &= e^{-(\frac{clusterY}{0.111})^2} \\
X_3 &= e^{-(\frac{clusterZ}{0.075})^2} \\
X_4 &= X_2 \times X_3 \\
X_5 &= X_1 \times X_4 \\
X_6 &= clusterY \times X_2 \\
X_7 &= clusterY^2 \times X_2
\end{aligned}
$$

$$
B = 1.21 - 0.0018 \times E_{cluster}
$$

$$
\begin{aligned}
A_0 &= 0.9626 \\
A_1 &= 0.00239 \\
A_2 &= -0.4674 \\
A_3 &= -0.5756 \\
A_4 &= 0.2906 \\
A_5 &= -0.00183 \\
A_6 &= 0.8945 \\
A_7 &= -10.1.
\end{aligned}
$$

The unit of energy is GeV and the unit of distance is m. Most of the position and run dependencies of $E_{cluster}$ have been removed by this correction.

5.4 Final Event Characteristics

There are a total of 15155 events surviving all the cuts. The characteristics of these events are plotted in Figure 5.10.

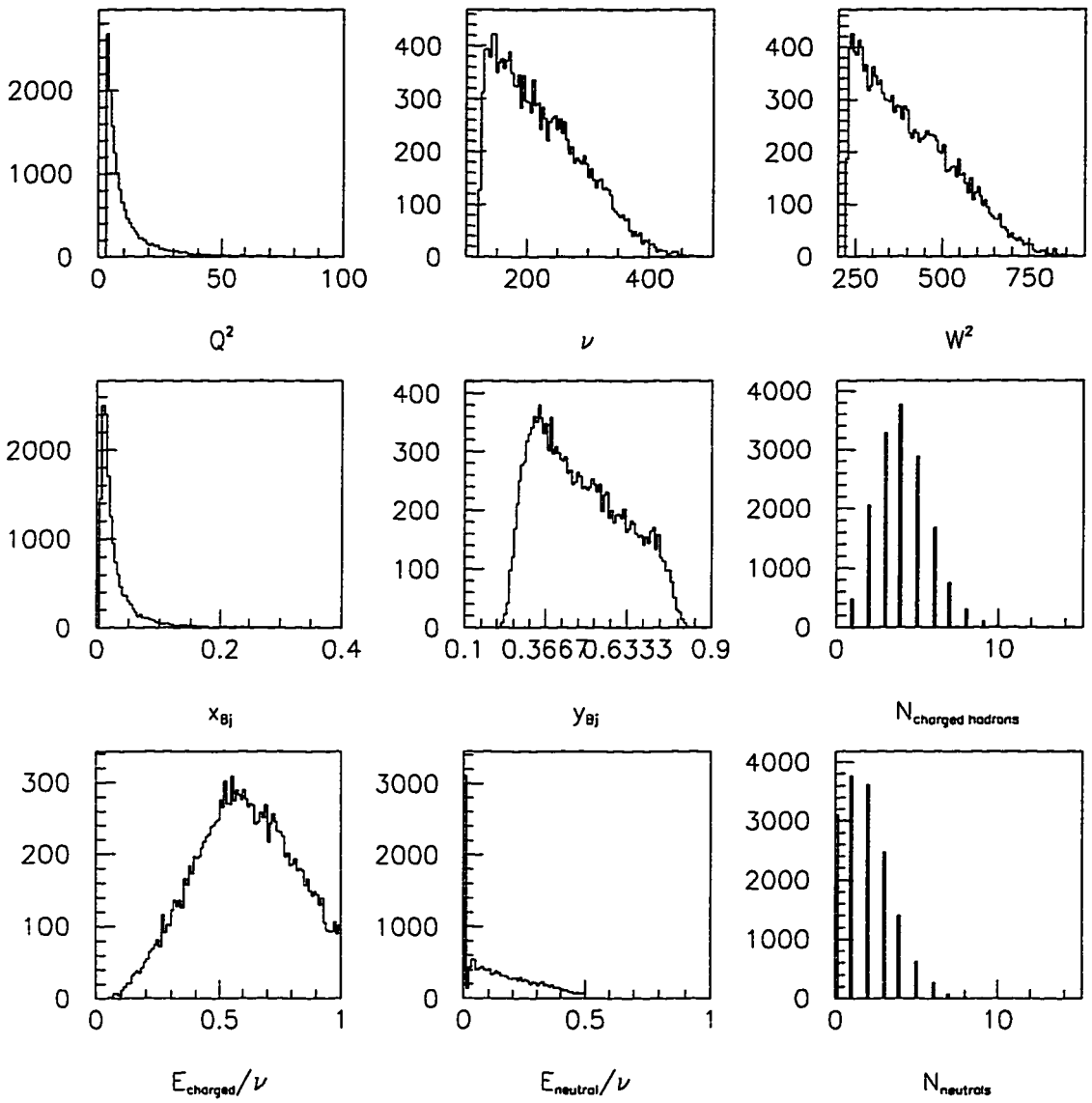

Figure 5.10: Kinematics distribution of final event sample.

Chapter 6

RESULTS AND ANALYSIS

The first order QCD process of a DIS event can be described in Figure 6.1. A lepton with momentum k_1 radiates a virtual photon with momentum q which scatters off a quark with momentum p in the target and produces two outgoing partons with momenta p_a and p_b. Figure 6.2 describes the same event in the lab. Only the momenta of the final hadrons can be measured in reality. These hadrons form one or more jets. From the study of the jet algorithms we know that hadron jets can reproduce the underlying parton transverse momenta and azimuthal distributions fairly well. Therefore, by measuring the jet azimuthal angle we are able to study the parton azimuthal distribution in the perturbative QCD process of Figure 6.1.

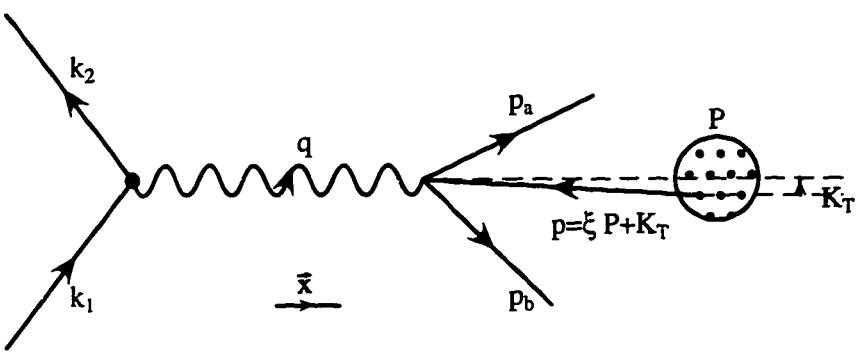

Figure 6.1: Variables in the parton world.

This chapter presents the characteristics of the uncorrected jets identified in the E665 Run91 data using the modified JADE and the Ellis-Soper algorithms. The data corrections used and the corrected jet azimuthal distributions are described in detail. The azimuthal asymmetry is also compared with the theoretical predictions. All the data used in this chapter have passed all the selection criteria described in Chapter 5. They are all presented in the center of mass frame of the virtual photon and the target (CMS).

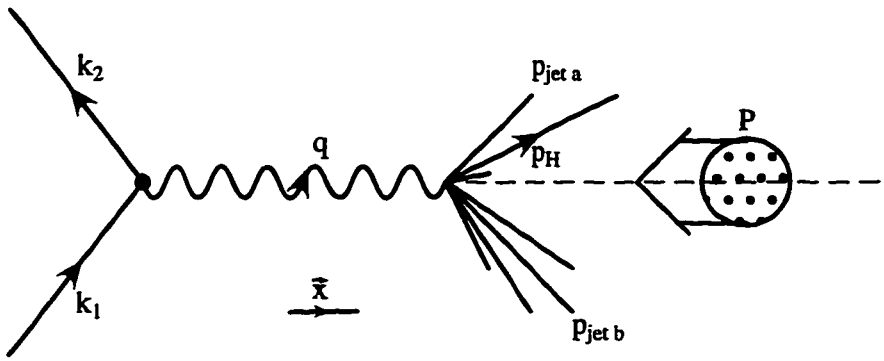

Figure 6.2: Variables that can be measured.

6.1 Observed Jet Properties of the Uncorrected Data

Various jet properties of 2-jet events using the modified JADE and Ellis-Soper algorithms are plotted in Figure 6.3 to 6.11. As discussed in Chapter 3, we choose $Y_{cut} = 0.04$ for JADE and $E_{Tcut} = 0.6\,GeV$ at $R^2 = 2$ for the Ellis-Soper algorithm. Corresponding distributions using $Y_{cut} = 0.08$ and $E_{Tcut} = 1.0\,GeV$ are also plotted for comparison. They will be used later to study the uncertainty in the algorithms. The data shown in these figures have not been corrected. Data corrections and uncertainties will be discussed in the next section.

Figure 6.3 shows the jet rate of the experimental data. For the MC events which includes the first order QCD matrix elements the 1-parton event rate is 60.6% and the 2-parton event rate is 39.4% after going through the selection discussed in Chapter 5. We only plotted the rates of 1-jet events (shown by solid circles [1]) and the rates of 2-jet events (in open squares). These two do not add up to 100% because of the existence of the events with three or more jets reconstructed. The modified JADE algorithm yields more events with multiple jets at lower Y_{cut}. As the Y_{cut} increases, the particles in the third jet merge with the first two jets and the particles in the second jet merge into the first jet. This causes the 1-jet rate to increase and the event rate of multiple jets to decrease. For the jets reconstructed by using the Ellis-Soper algorithm in each event, with the increase of E_{Tcut} more jets are eliminated as part of the target remnant. Only those jets with the highest transverse energy can survive. Therefore, for a given event the number of selected jets decreases.

Figure 6.4 and 6.5 plot the momentum ratio P_2/P_1 of the two jets in 2-jet events,

[1] A spline fit is used to connect the data points.

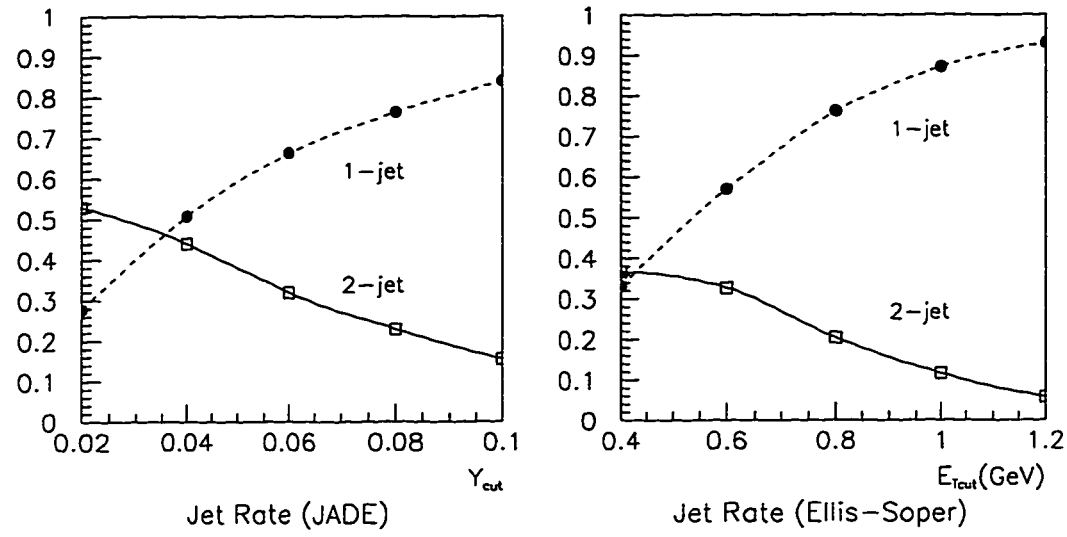

Figure 6.3: Uncorrected jet rate identified by two algorithms: dashed line, 1-jet event rate; solid line, 2-jet event rate.

where $P_1 > P_2$. In the data we observed with both algorithms, the production rate of events with two jets of similar energy or momentum is much less than the production rate of events where one jet is much more energetic than the other. This result agrees with the prediction of the Monte Carlo (see discussion in Section 3.3.4). For the Ellis-Soper algorithm, the jet momenta is less asymmetrical, because this algorithm intentionally preserves jets with higher energies.

As shown in Figure 6.6 and 6.7, in 2-jet events the two jets reconstructed by both algorithms are well separated in CMS. This is very important. In events with two jets very close to each other there is more ambiguity in separating the particles and therefore a larger possibility of particle misassignment between the two jets. This can affect the transverse momenta and the directions of both jets. From these two plots, we clearly see that these ambiguous events fail the selection criteria of both algorithms. This is also true for the MC events.

The transverse momentum distributions of both jets in 2-jet events are shown in Figure 6.8 and 6.9. There is a lower threshold in the transverse momenta of the jets identified by the Ellis-Soper algorithm. The threshold results from the E_{Tcut}'s of 0.6 GeV and 1 GeV.

The distributions of the azimuthal angles of both jets in 2-jet events are shown in Figure 6.10 and 6.11. The uncorrected data clearly show an asymmetry in the

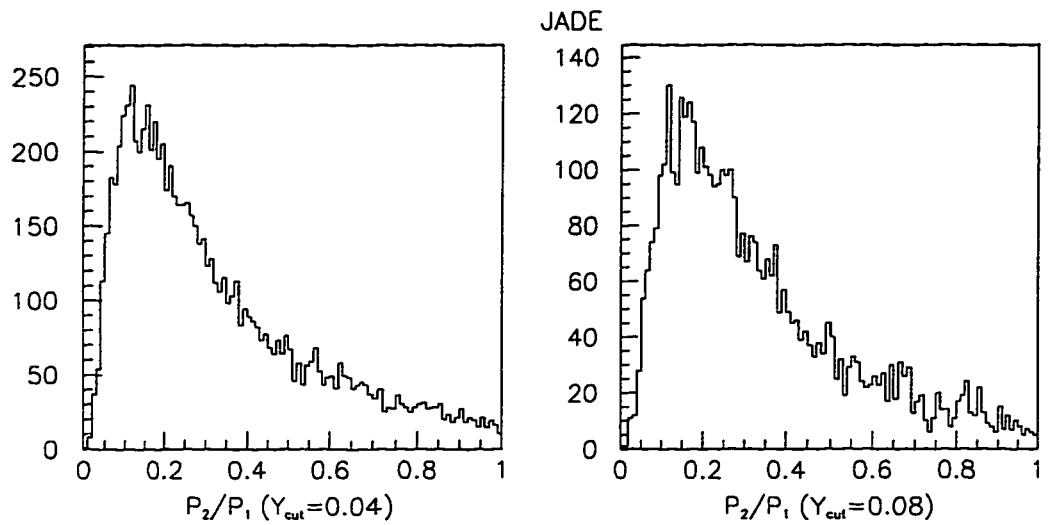

Figure 6.4: The distribution of the uncorrected jet momentum ratio in 2-jet events identified by the modified JADE algorithm, where 1 is the highest momentum jet.

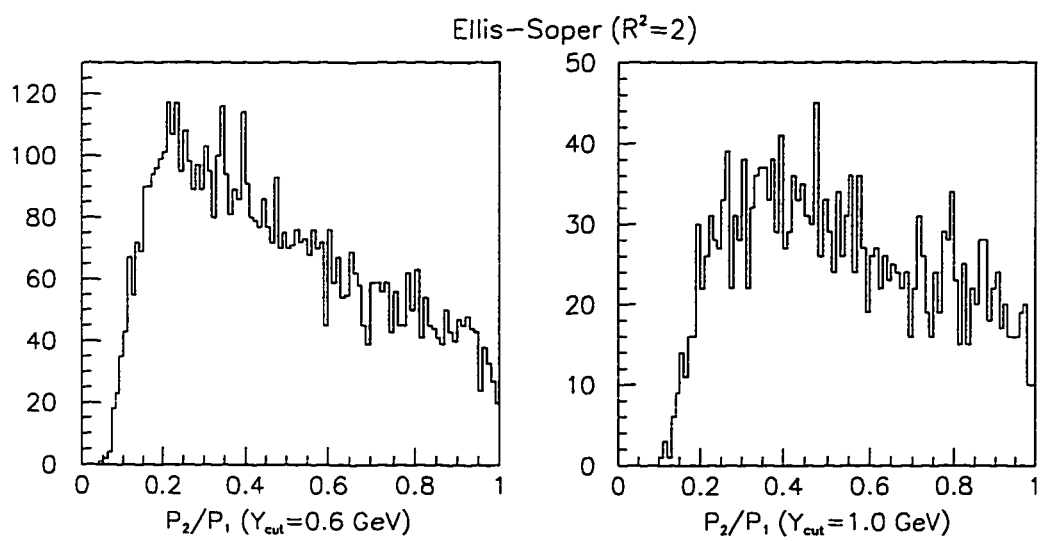

Figure 6.5: The distribution of the uncorrected jet momentum ratio in 2-jet events identified by the Ellis-Soper algorithm at $R^2 = 2$, where 1 is the highest momentum jet.

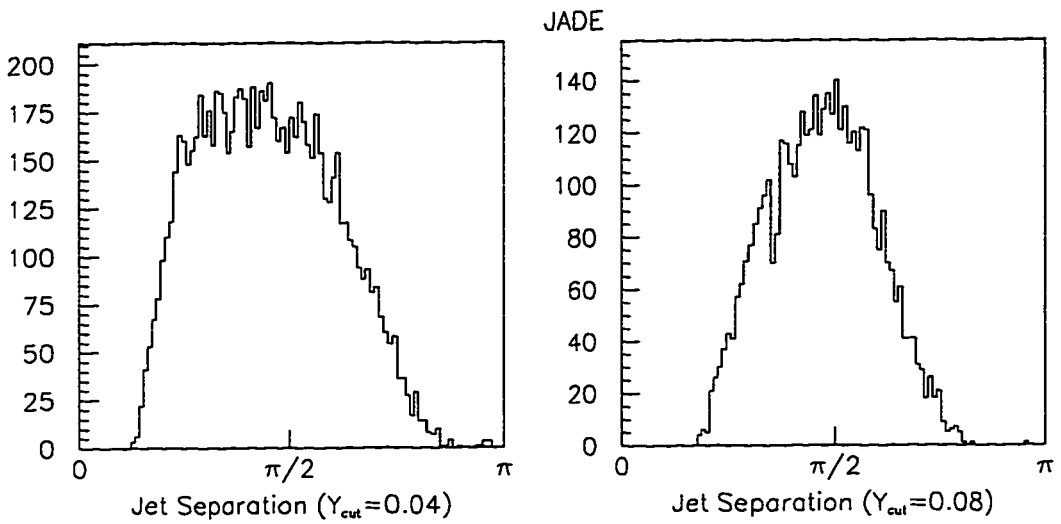

Figure 6.6: Uncorrected spatial separation angle between the two jet axes in 2-jet events in CMS identified by the modified JADE algorithm.

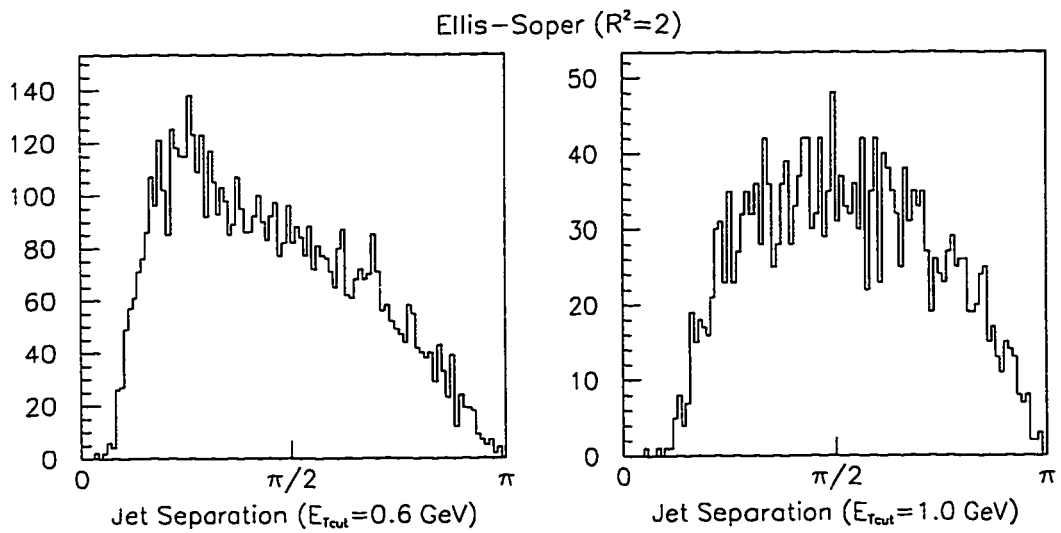

Figure 6.7: Uncorrected spatial separation angle between the two jet axes in 2-jet events in CMS identified by the Ellis-Soper algorithm at $R^2 = 2$.

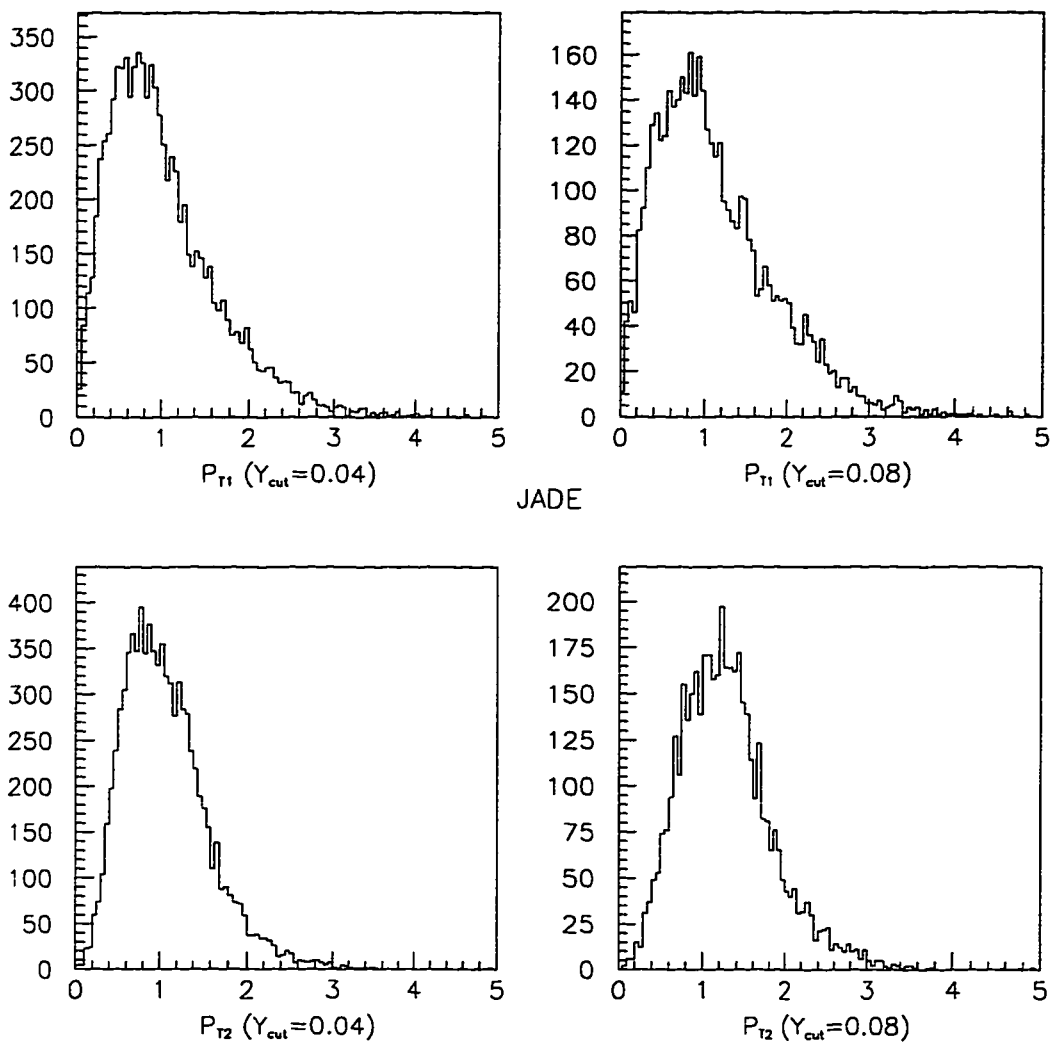

Figure 6.8: The uncorrected transverse momentum distribution in 2-jet events reconstructed by the modified JADE algorithm, where P_{T1} (P_{T2}) is the transverse momentum of the more (less) energetic jet.

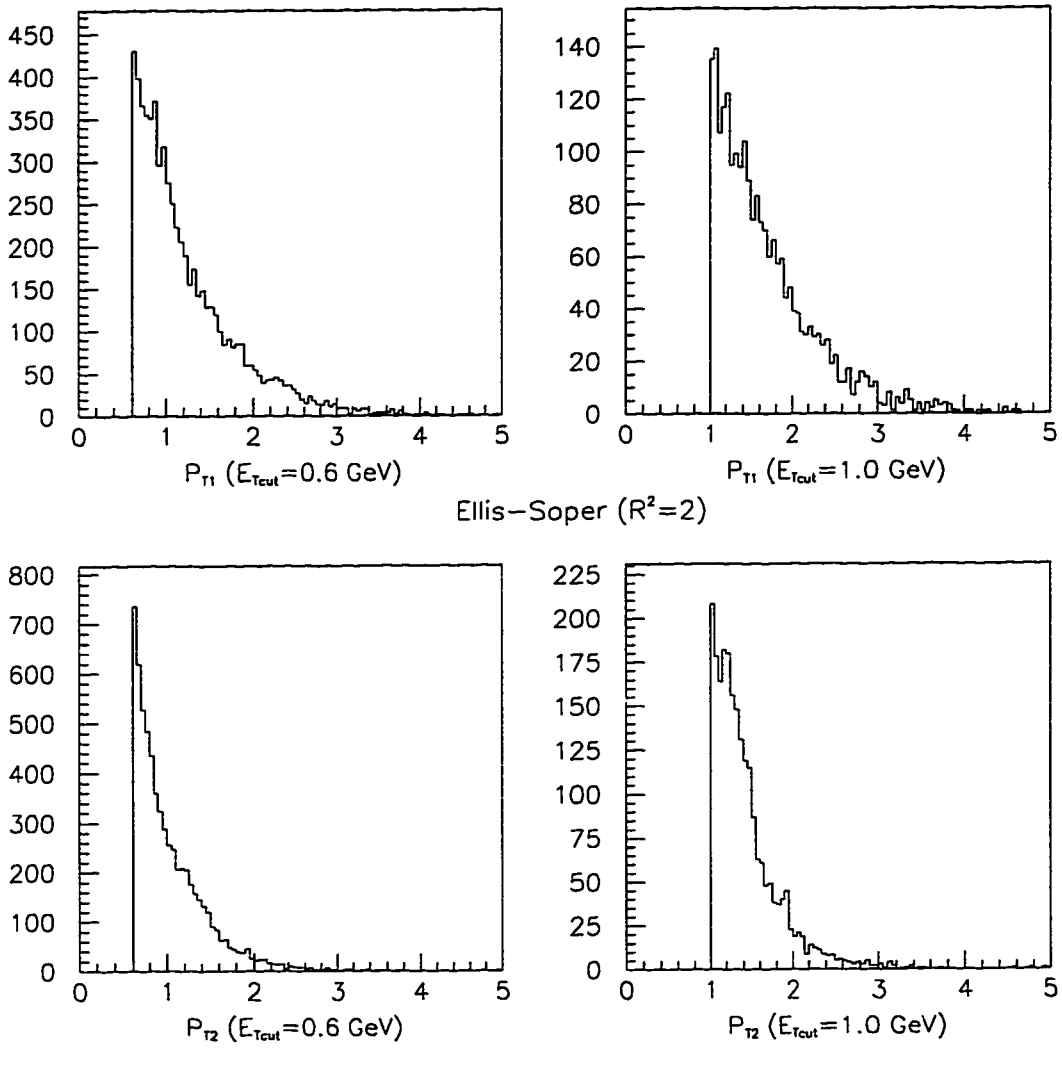

Figure 6.9: The uncorrected transverse momentum distribution in 2-jet events reconstructed by the Ellis-Soper algorithm at $R^2 = 2$, where P_{T1} (P_{T2}) is the transverse momentum of the more (less) energetic jet.

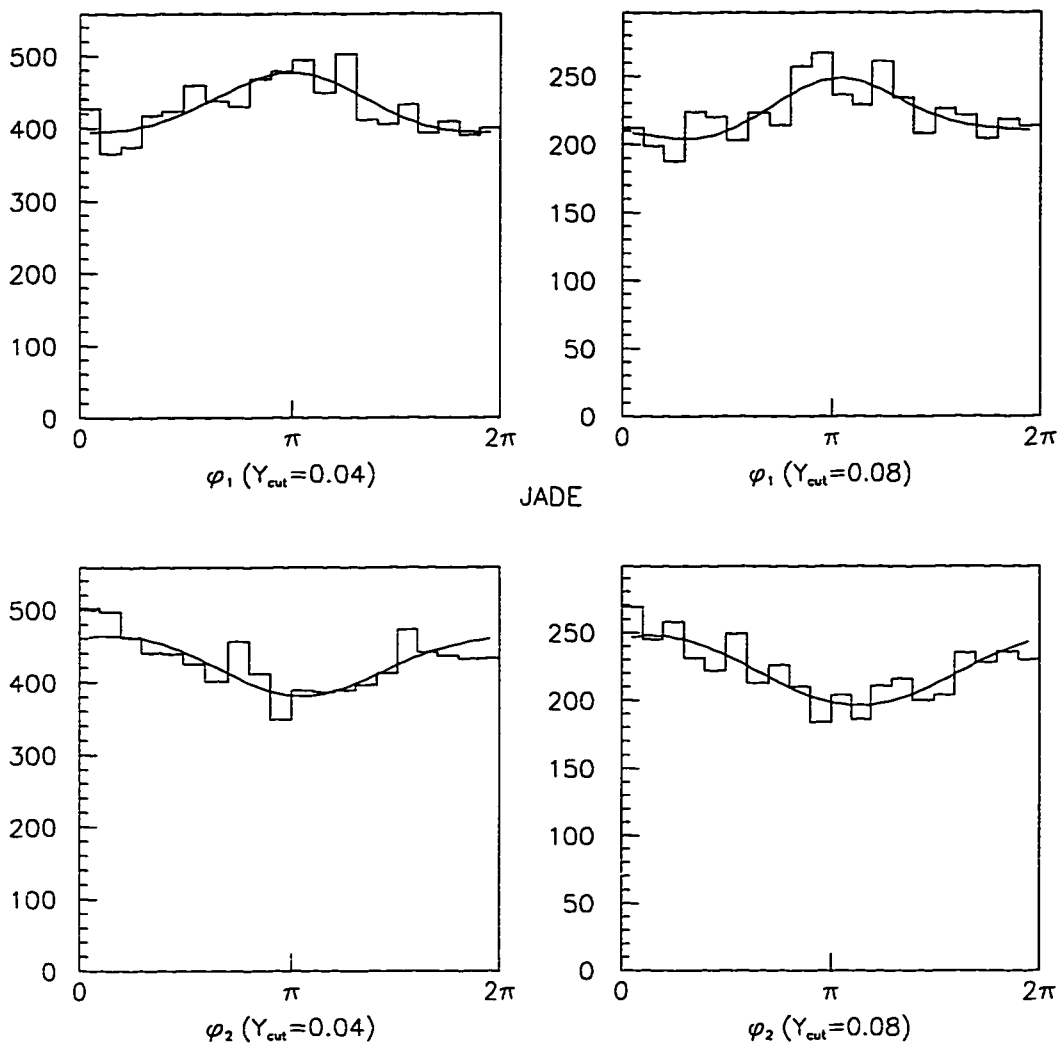

Figure 6.10: The uncorrected azimuthal distribution in 2-jet events reconstructed by the modified JADE algorithm. ϕ_1 is the azimuthal angle of the jet with larger energy and ϕ_2 is the azimuthal angle of the other jet.

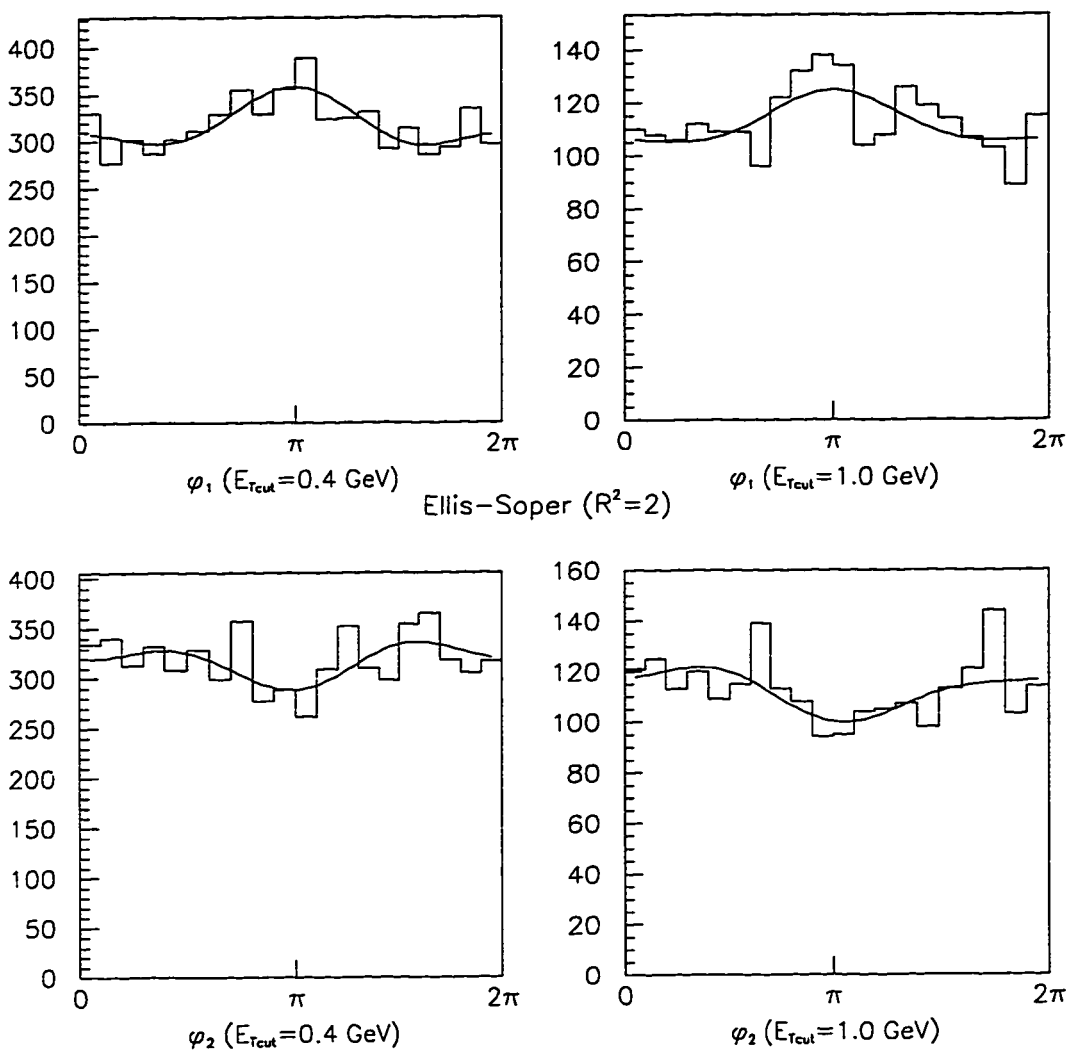

Figure 6.11: The uncorrected azimuthal distribution in 2-jet events reconstructed by the Ellis-Soper algorithm at $R^2 = 2$. ϕ_1 is the azimuthal angle of the jet with larger energy and ϕ_2 is the azimuthal angle of the other jet.

distributions of the azimuthal angle ϕ. The distribution of ϕ_1, which is the azimuthal angle of the more energetic jet, populates more around π, while the distribution of ϕ_2, which is the azimuthal angle of the less energetic jet, populates more around 0 and 2π (the opposite direction), regardless of the value of its transverse momentum. This measured azimuthal asymmetry agrees well with the theoretic prediction. The corresponding parton azimuthal distributions in the MC events can be found in Figure 3.15 and Figure 3.16. The azimuthal distributions in Figure 6.10 and 6.11 have been fit to the function $A + Bcos\phi + Ccos2\phi + Dsin\phi$ in solid lines (see Section 6.3.1 for details).

6.2 Data Correction and Systematic Uncertainty

This section describes the two major corrections to the data for the azimuthal angular distribution and their uncertainties. These uncertainties and the uncertainty due to the jet algorithms will be combined and treated as systematic errors. The statistical error can be easily obtained.

6.2.1 Acceptance Correction and Its Uncertainty

Monte Carlo (MC) data generated from a series of physics event generators, namely Lepto, Jetset, and Gamrad are used to correct for acceptance. The MC data without going through the detector simulation and pattern recognition are referred as the "Truth" data, and the MC data reconstructed from the detected hits with the standard E665 Run91 detector simulation are referred as the "Reconstructed" data. The jets obtained from the "Truth" data using the appropriate algorithms are simply called "MC Truth Jets", while the jets obtained from the "Reconstructed" data are called "MC Reconstructed Jets". The ratio between the distributions of these two jet samples is used to correct the experimental data.

$$\frac{\text{MC Truth Jets}}{\text{MC Reconstructed Jets}} = \text{Acceptance Correction Factor.}$$

The acceptance losses are mainly due to the fact that low momentum particles or large angle tracks can not be detected in the forward spectrometer and low energy photon clusters have poor calorimeter response[2]. Because the energy of these tracks or clusters are low this correction is small. In Figure 6.12 to 6.15 the correction

[2] In selecting calorimeter clusters, we require the energy to be greater than 5 GeV. See Section 5.3.

factors of the azimuthal distributions of the jets reconstructed are shown for the two algorithms.

In part (a) of these figures, each solid point represents the "MC Truth Jet" ϕ distribution and each dashed point represents the "MC Reconstructed Jet". The statistical error shown is given by $1/\sqrt{N}$, where N is the number of events. The ratios of "MC Truth Jet" to "MC Reconstructed Jet" distributions, or the correction factors, are shown in part (b), on the right side of the corresponding ϕ distribution. The errors shown in part (b) are calculated assuming no correlations. That is,

$$\delta(\frac{N_1}{N_2}) = \sqrt{(\frac{1}{N_2}\delta_1)^2 + (\frac{N_1}{N_2^2}\delta_2)^2}$$

for any distribution of N_1/N_2, where N_1 and N_2 are the respective number of events and δ_1 and δ_2 are the corresponding statistical uncertainties.

The detector simulation uses experimentally measured efficiencies for all the detectors. Detailed studies of different chambers and calorimeter efficiencies used in the simulation are discussed in references [52] and [46]. In particular, a summary of the detector efficiencies are given in the table "Measured global chamber efficiencies for various run blocks" in [46].

As shown in figures 6.12 to 6.15, the acceptance correction factors are consistent with unity to within statistical errors.[3] Therefore, these correction factors are not applied to the experimental data in order to avoid increasing the bin to bin statistical fluctuations.

6.2.2 Radiative Correction and Its Uncertainty

The angular cuts[4] used to remove the radiative events may also affect the jet ϕ distributions. The correction can be obtained from the ratio of the jet distribution using non-radiative DIS MC data and the corresponding distribution using all MC data with these angular cuts.

$$\frac{\text{MC Non-radiative Jet(before angular cuts)}}{\text{"All" MC Jet(with cuts)}} = \text{Radiation Correction Factor.}$$

[3] Incorrect modeling of the detectors introduces incorrect acceptance correction. Because the efficiency for most chambers is greater than 95%, we have studied the acceptance uncertainty by randomly "dropping" 5% of the final detected particles. The change in the ϕ distribution is smaller than the statistical uncertainty. Therefore, the acceptance uncertainty is negligible.

[4] See Section 5.1.5

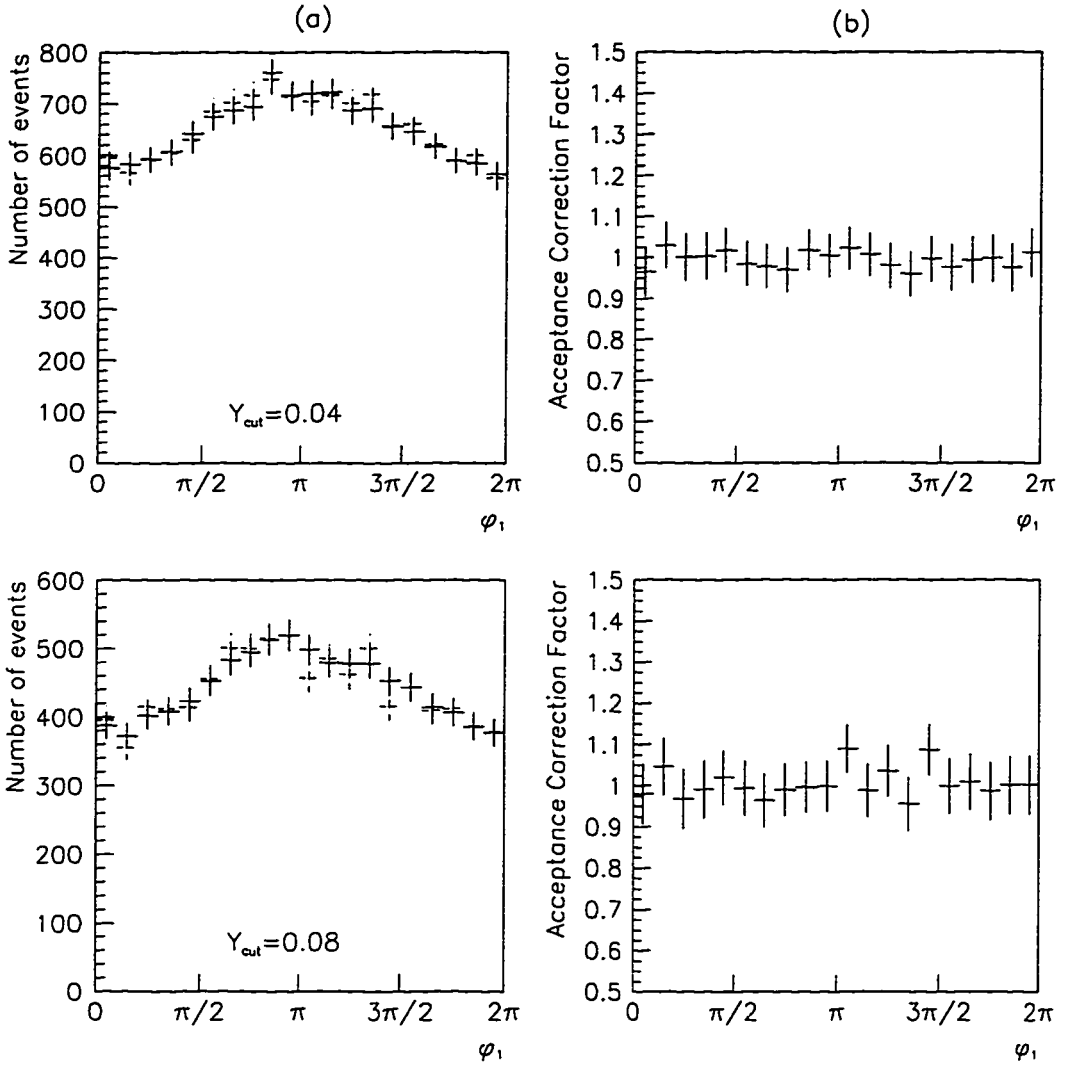

Figure 6.12: The acceptance corrections for the azimuthal angle ϕ_1 of the more energetic jet reconstructed by the modified JADE algorithm. (a) Solid and dashed distributions represent "MC Truth Jet" and "MC Reconstructed Jet", respectively. (b) The acceptance correction factors.

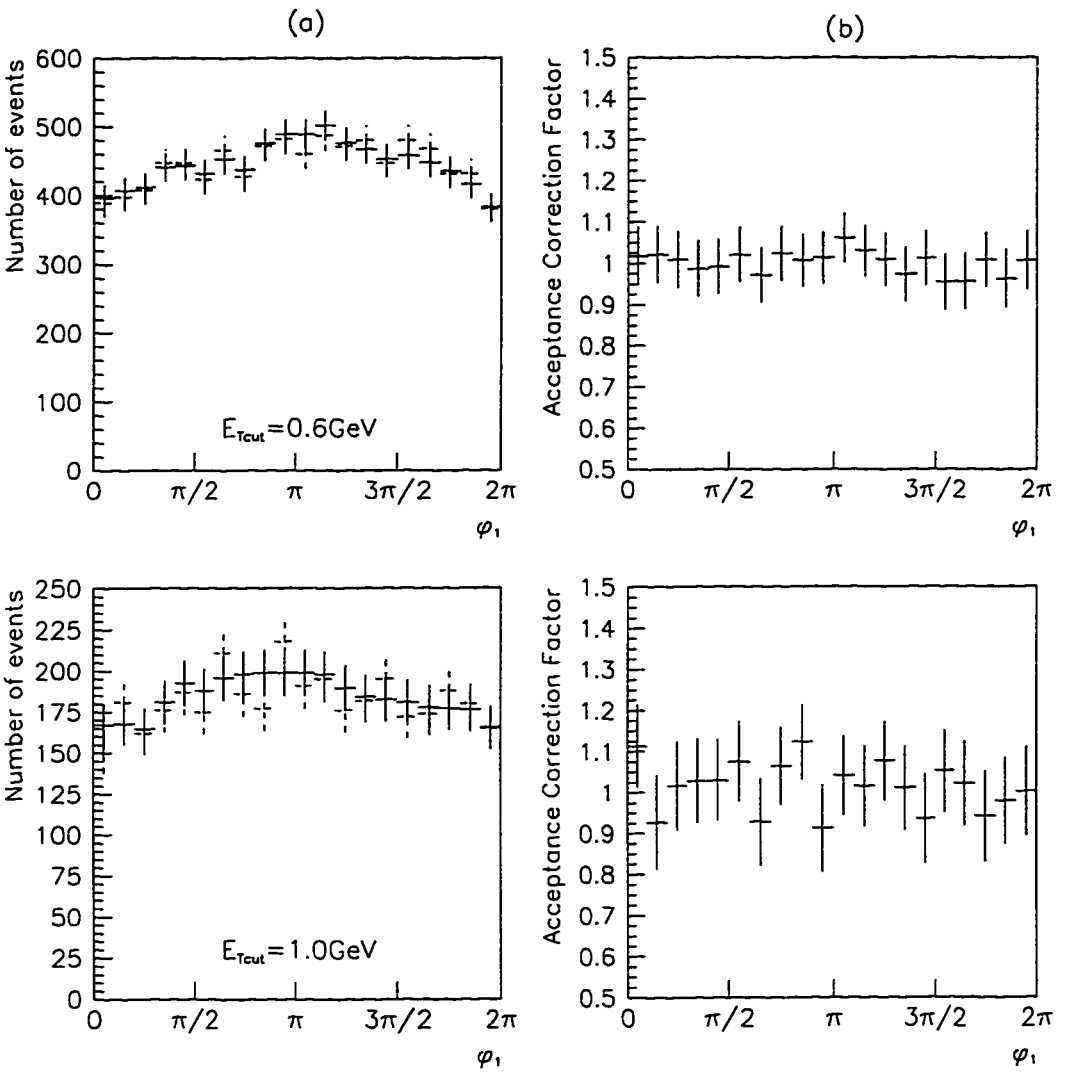

Figure 6.13: The acceptance corrections for the azimuthal angle ϕ_1 of the more energetic jet reconstructed by the Ellis-Soper algorithm at $R^2 = 2$. (a) Solid and dashed distributions represent "MC Truth Jet" and "MC Reconstructed Jet", respectively. (b) The acceptance correction factors.

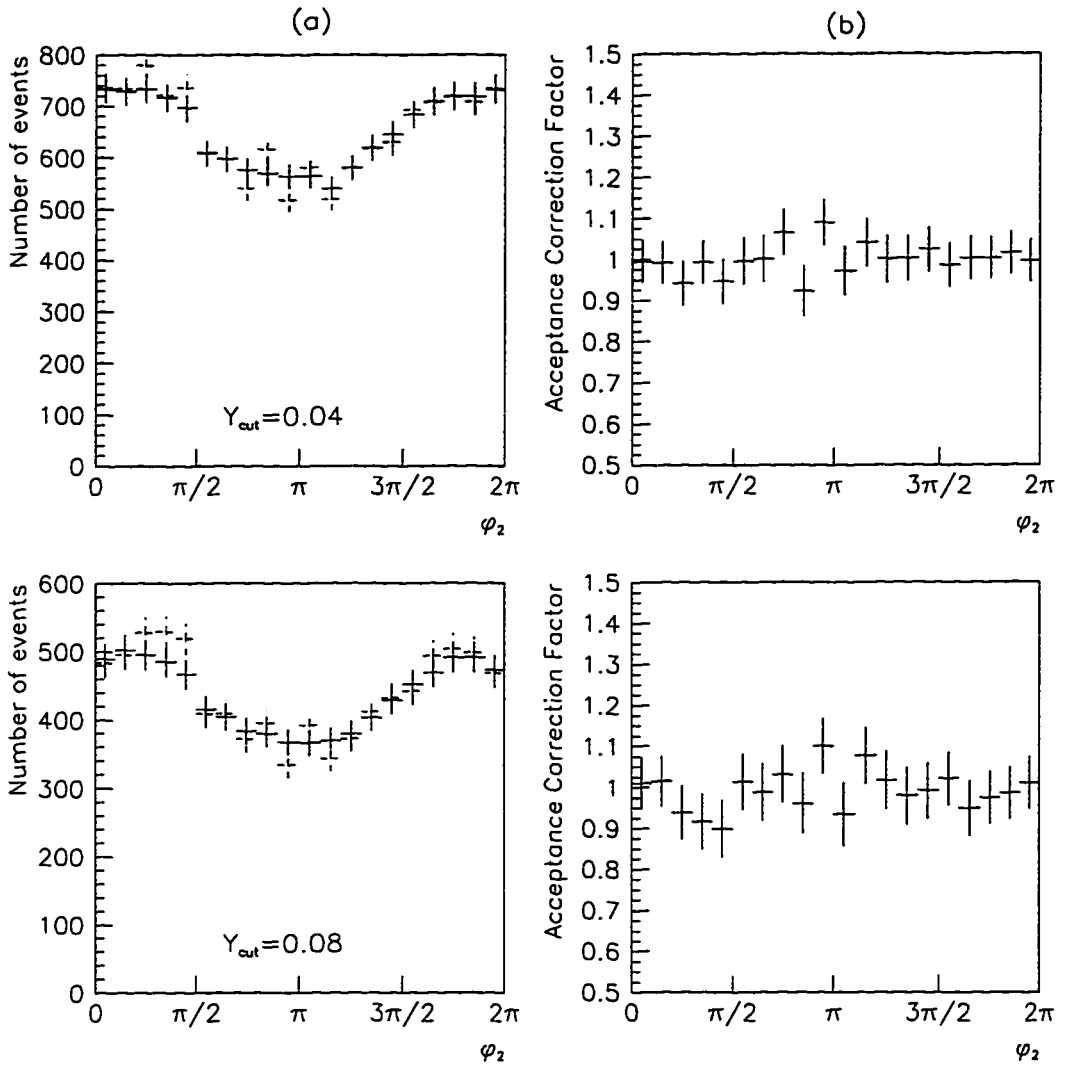

Figure 6.14: The acceptance corrections for the azimuthal angle ϕ_2 of the less energetic jet reconstructed by the modified JADE algorithm. (a) Solid and dashed distributions represent "MC Truth Jet" and "MC Reconstructed Jet", respectively. (b) The acceptance correction factors.

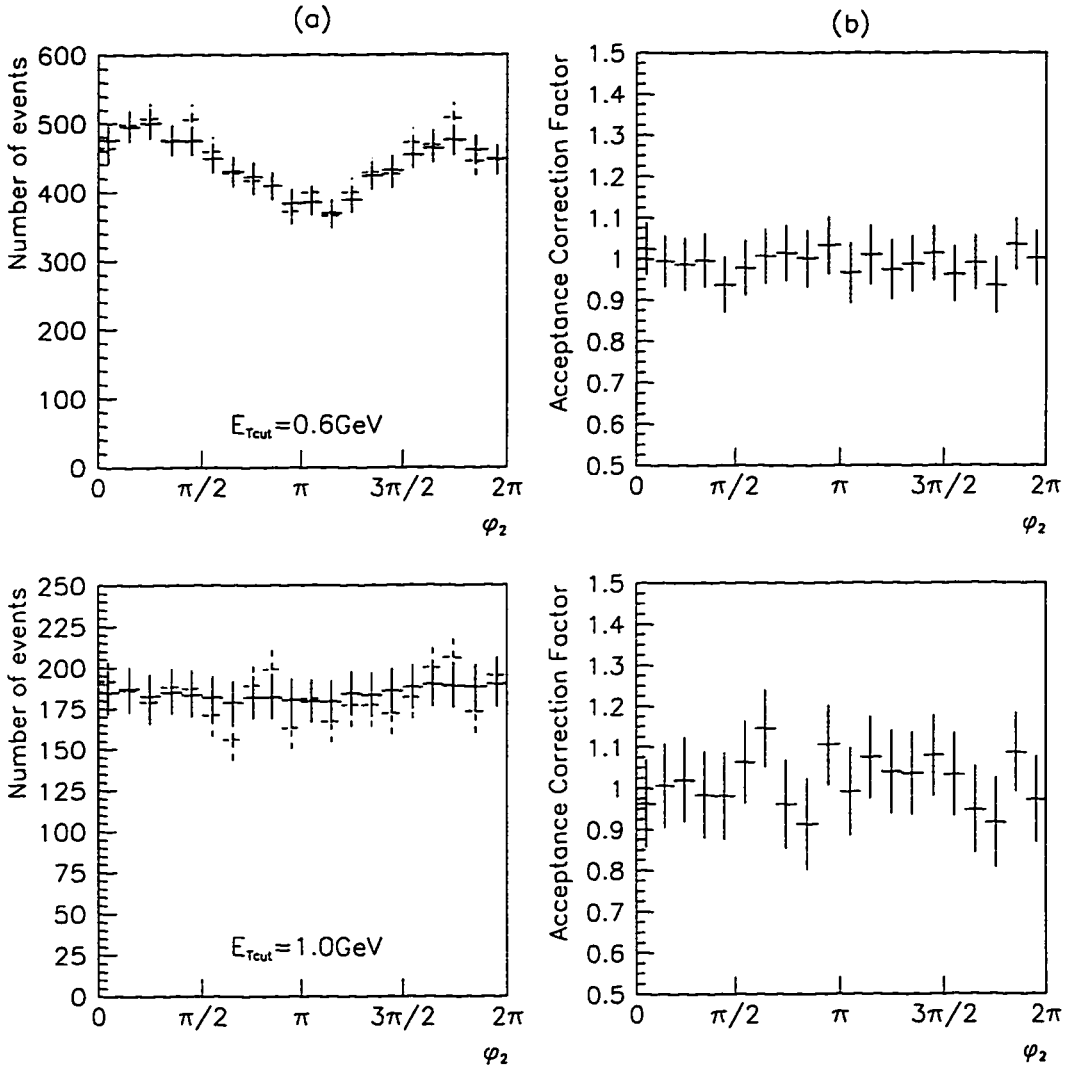

Figure 6.15: The acceptance corrections for the azimuthal angle ϕ_2 of the less energetic jet reconstructed by the Ellis-Soper algorithm at $R^2 = 2$. (a) Solid and dashed distributions represent "MC Truth Jet" and "MC Reconstructed Jet", respectively. (b) The acceptance correction factors.

Here, "All" means a mixture of both non-radiative DIS events and radiative events. The radiative corrections for both algorithms are plotted in Figure 6.16 to 6.19.

The jet azimuthal distribution of the MC non-radiative events without the angular radiative cuts are plotted in part (a) of these figures together with that of all the MC events that survive all the cuts. The correction factor which is the ratio of these two distributions is plotted in part (b). The statistical uncertainty of each bin is shown as an error bar.

As we see, the angular cuts tend to reduce the asymmetry in the jet azimuthal distributions. A fit of the correction factors shown in Figure 6.20 and 6.21 to the function $A + Bcos\phi + Ccos2\phi + Dsin\phi$ is used. This function determines bin-by-bin radiative correction factors to the experimental data.

6.2.3 Uncertainty in the Jet Algorithms

We have plotted earlier the ϕ distributions of the jets reconstructed by the two algorithms using different resolution cuts. The absolute fractional differences of the normalized distributions by two different cuts are plotted in Figure 6.22 and 6.23.

The average difference $\langle\Delta\rangle$ is summarized in Table 6.1. Again, ϕ_1 represents the azimuthal angle of the more energetic jet and ϕ_2 represents the other jet. Due to the lack of enough data, this algorithm dependent uncertainty is statistical in nature. Especially for the Ellis-Soper algorithm, the relatively larger uncertainty comes mainly from the lower statistics.

Table 6.1: Average difference $\langle\Delta\rangle$ of the algorithms.

Algorithm	Cuts	$\langle\Delta\rangle$ in ϕ_1	$\langle\Delta\rangle$ in ϕ_2
JADE	$Y_{cut} = 0.04$ and 0.08	3.2%	3.2%
Ellis-Soper	$E_{Tcut} = 0.6$ and 1.0 GeV ($R^2 = 2$)	6.3%	7.4%

6.3 Jet Azimuthal Asymmetry

6.3.1 Azimuthal Distribution of the Corrected Jets

The corrected azimuthal angular distributions ϕ_1 and ϕ_2 in 2-jet events are shown in Figure 6.24 and 6.25. The more energetic jet populates more around π and the less

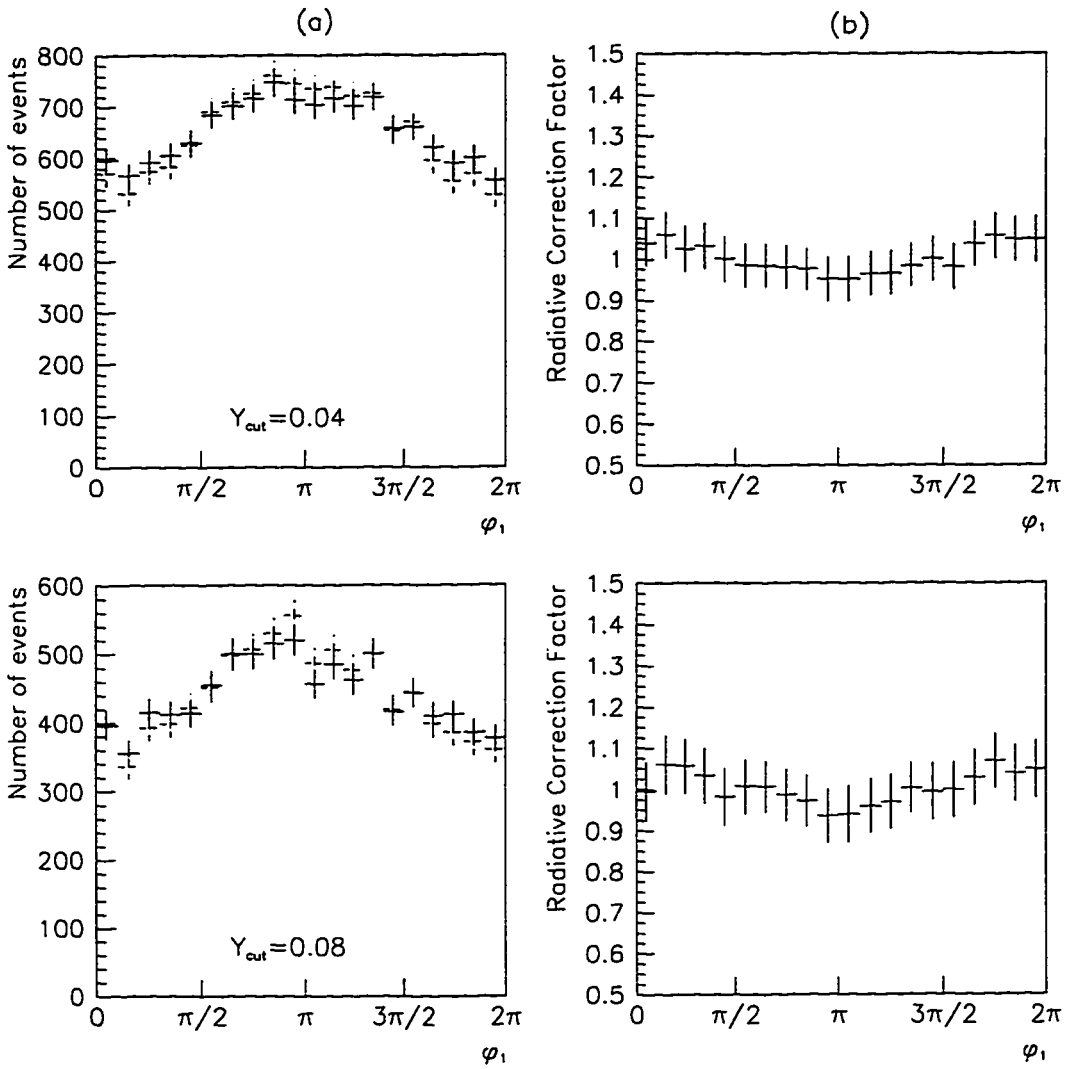

Figure 6.16: The radiative corrections for the azimuthal angle ϕ_1 of the more energetic jet reconstructed by the modified JADE algorithm. (a) Solid and dashed distributions represent "MC Non-radiative Jet" and "All MC Jet", respectively. (b) The radiative correction factors.

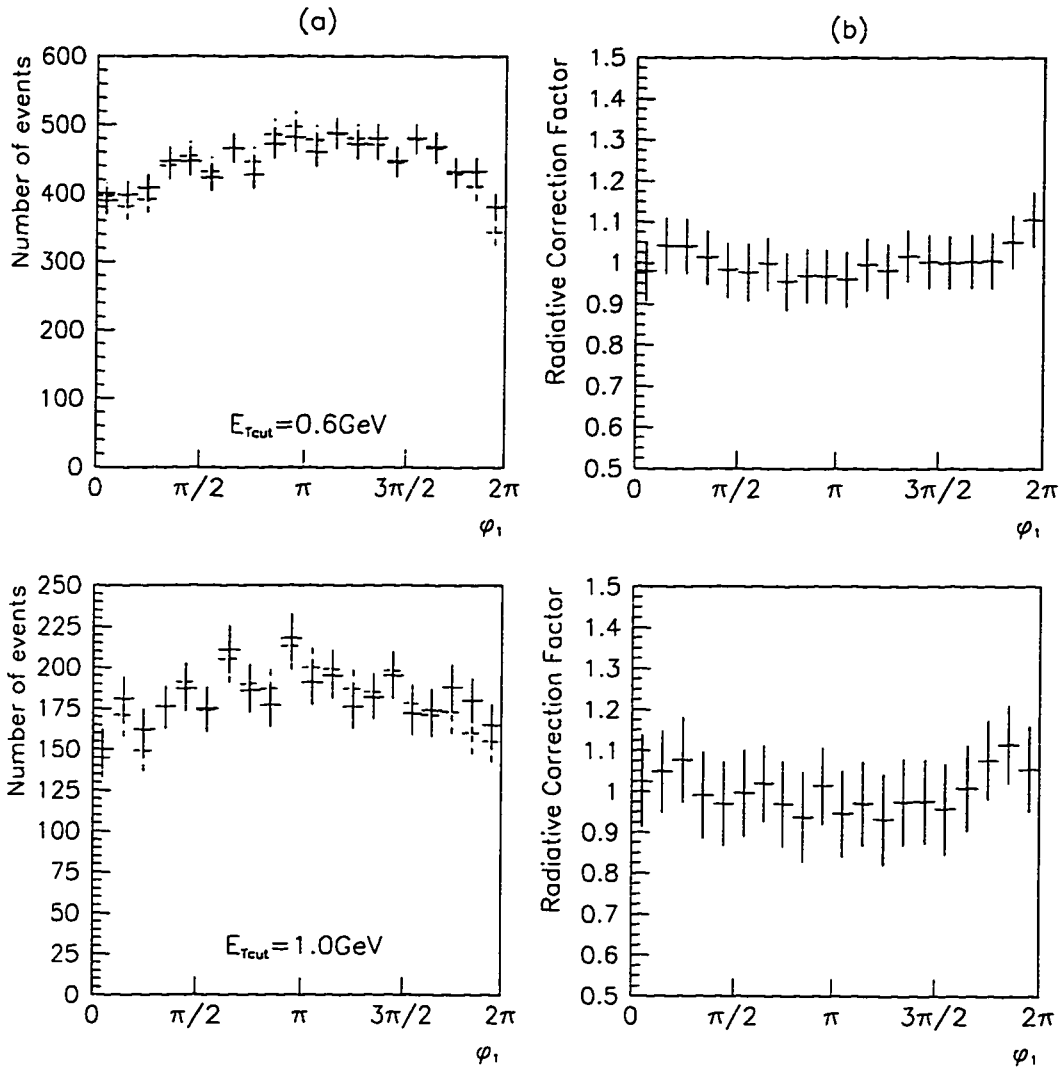

Figure 6.17: The radiative corrections for the azimuthal angle ϕ_1 of the more energetic jet reconstructed by the Ellis-Soper algorithm at $R^2 = 2$. (a) Solid and dashed distributions represent "MC Non-radiative Jet" and "All MC Jet", respectively. (b) The radiative correction factors.

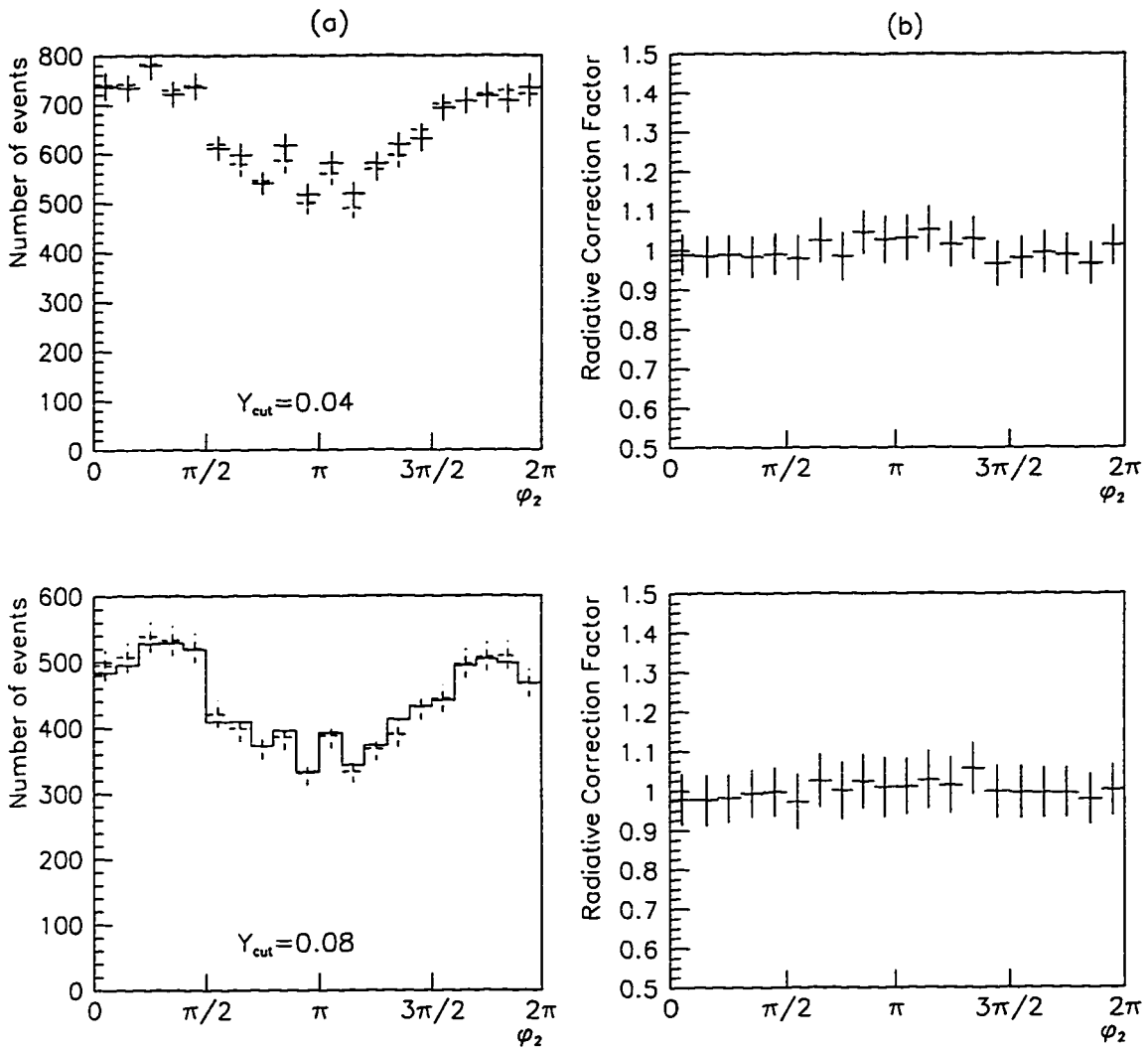

Figure 6.18: The radiative corrections for the azimuthal angle ϕ_2 of the less energetic jet reconstructed by the modified JADE algorithm. (a) Solid and dashed distributions represent "MC Non-radiative Jet" and "All MC Jet", respectively. (b) The radiative correction factors.

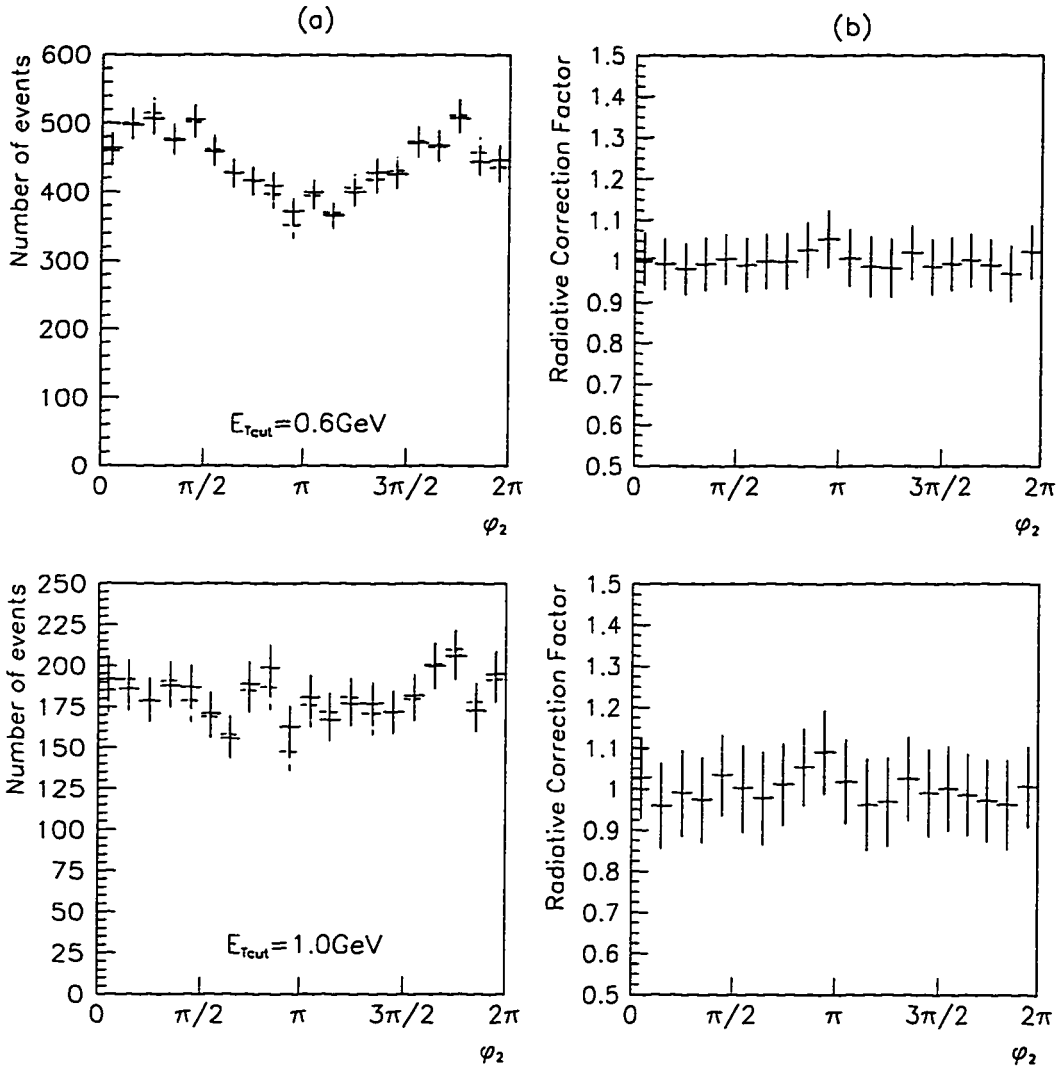

Figure 6.19: The radiative corrections for the azimuthal angle ϕ_2 of the less energetic jet reconstructed by the Ellis-Soper algorithm at $R^2 = 2$. (a) Solid and dashed distributions represent "MC Non-radiative Jet" and "All MC Jet", respectively. (b) The radiative correction factors.

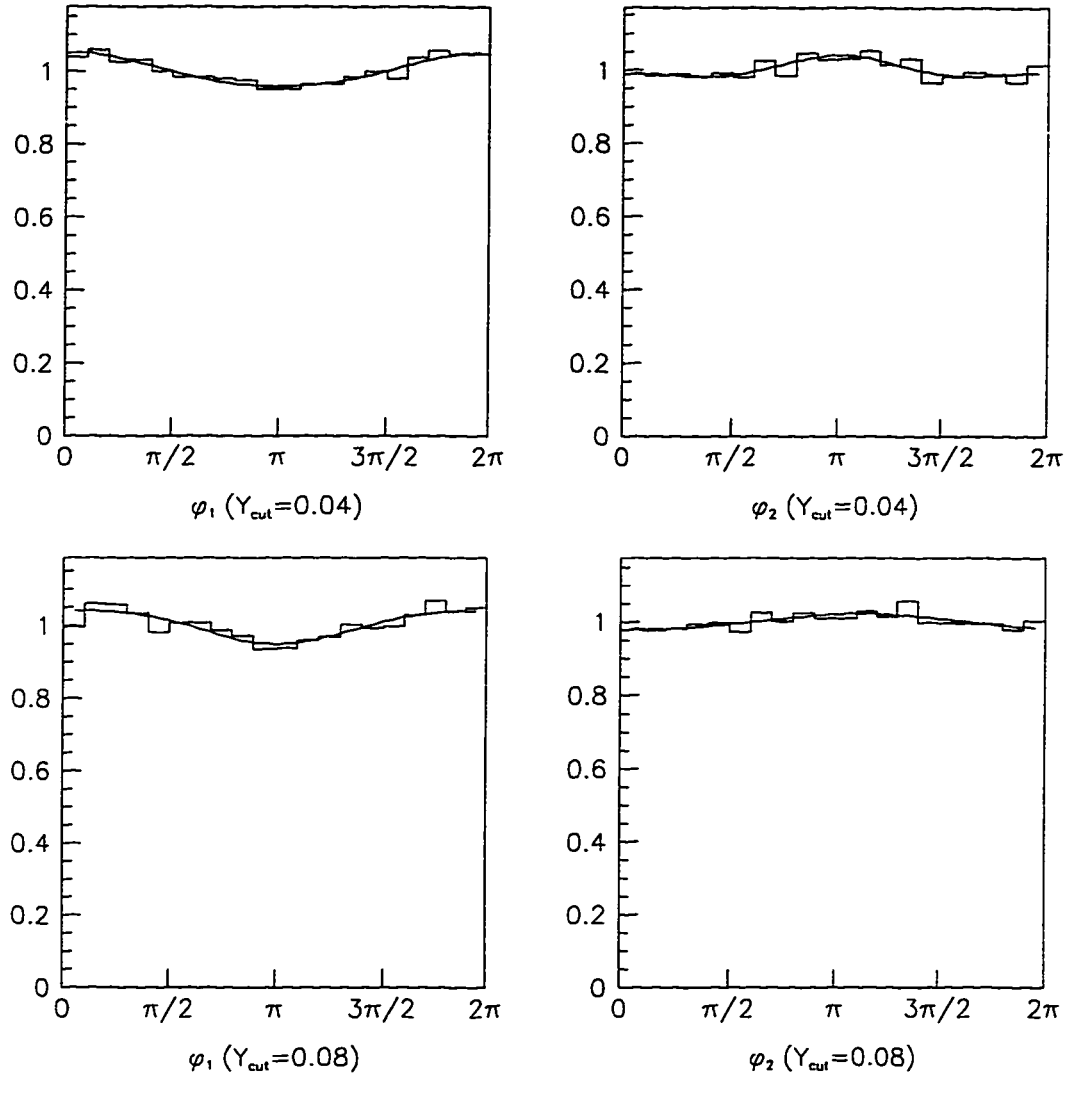

Figure 6.20: The radiative corrections fit to the function $A+Bcos\phi+Ccos2\phi+Dsin\phi$ for 2-jet events identified by the modified JADE algorithm, where ϕ_1 and ϕ_2 are the azimuthal angles of the more and the less energetic jet, respectively.

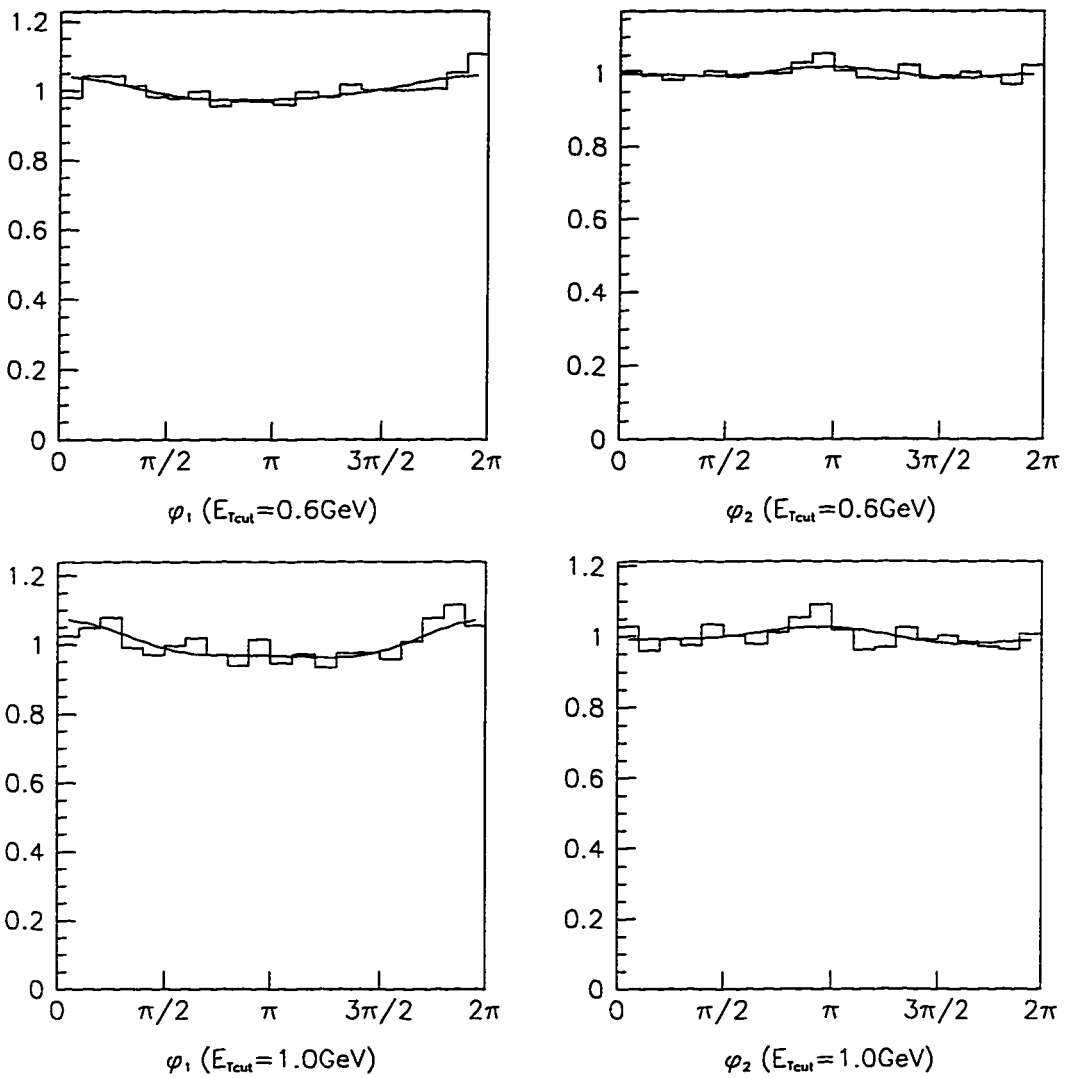

Figure 6.21: The radiative corrections fit to the function $A+Bcos\phi+Ccos2\phi+Dsin\phi$ for 2-jet events identified by the Ellis-Soper algorithm at $R^2 = 2$, where ϕ_1 and ϕ_2 are the azimuthal angles of the more and the less energetic jet, respectively.

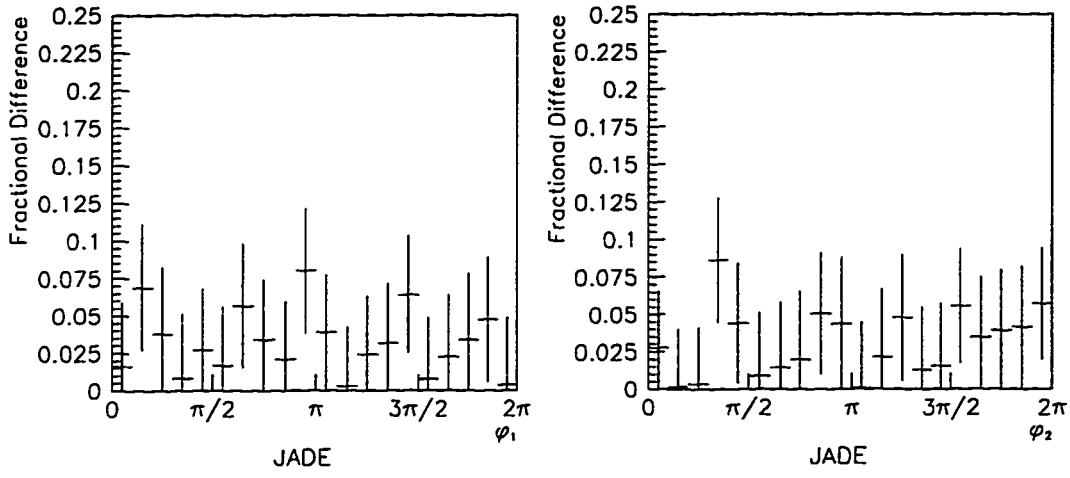

Figure 6.22: The uncertainty of the jet azimuthal distributions due to different resolution cuts used ($Y_{cut} = 0.04$ and 0.08) in the modified JADE algorithm.

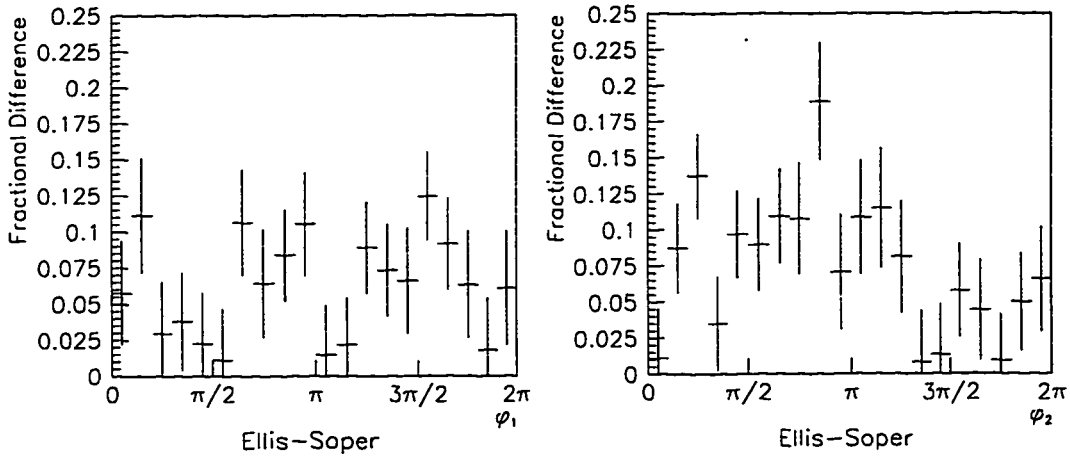

Figure 6.23: The uncertainty of the jet azimuthal distributions due to different resolution cuts used ($E_{Tcut} = 0.6\,GeV$ and 1.0 GeV) in the Ellis-Soper algorithm.

energetic jet populates more around 0 or 2π. This is expected by the perturbative QCD calculation. It also agrees with the Monte Carlo simulated parton azimuthal distributions in Figure 3.15 and 3.16. Unless otherwise stated all data presented from now on are corrected for radiative effects.

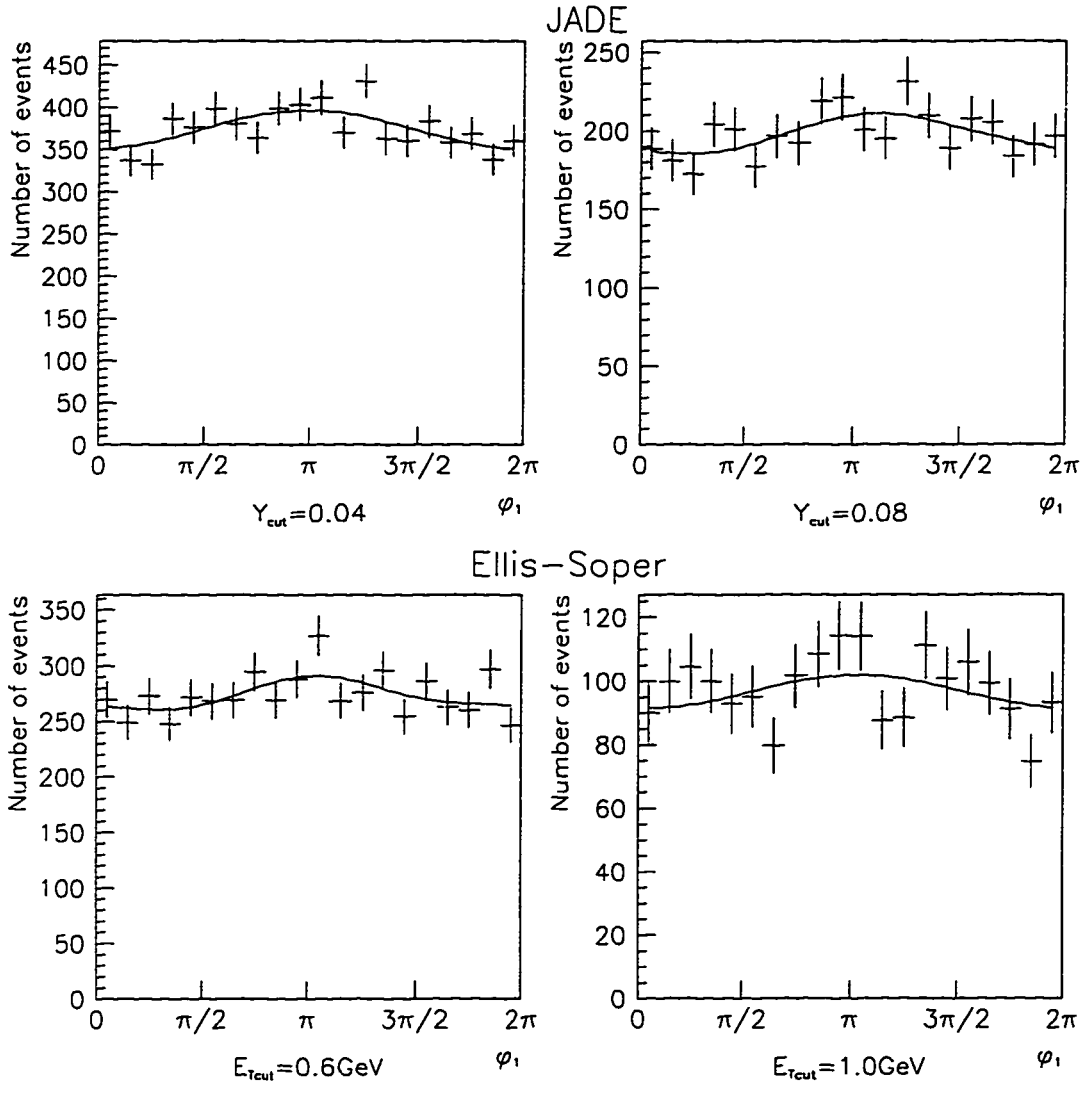

Figure 6.24: The corrected azimuthal distribution ϕ_1 of the more energetic jet in 2-jet events.

In order to calculate the average value of $cos\phi$, each histogram is fit to a general

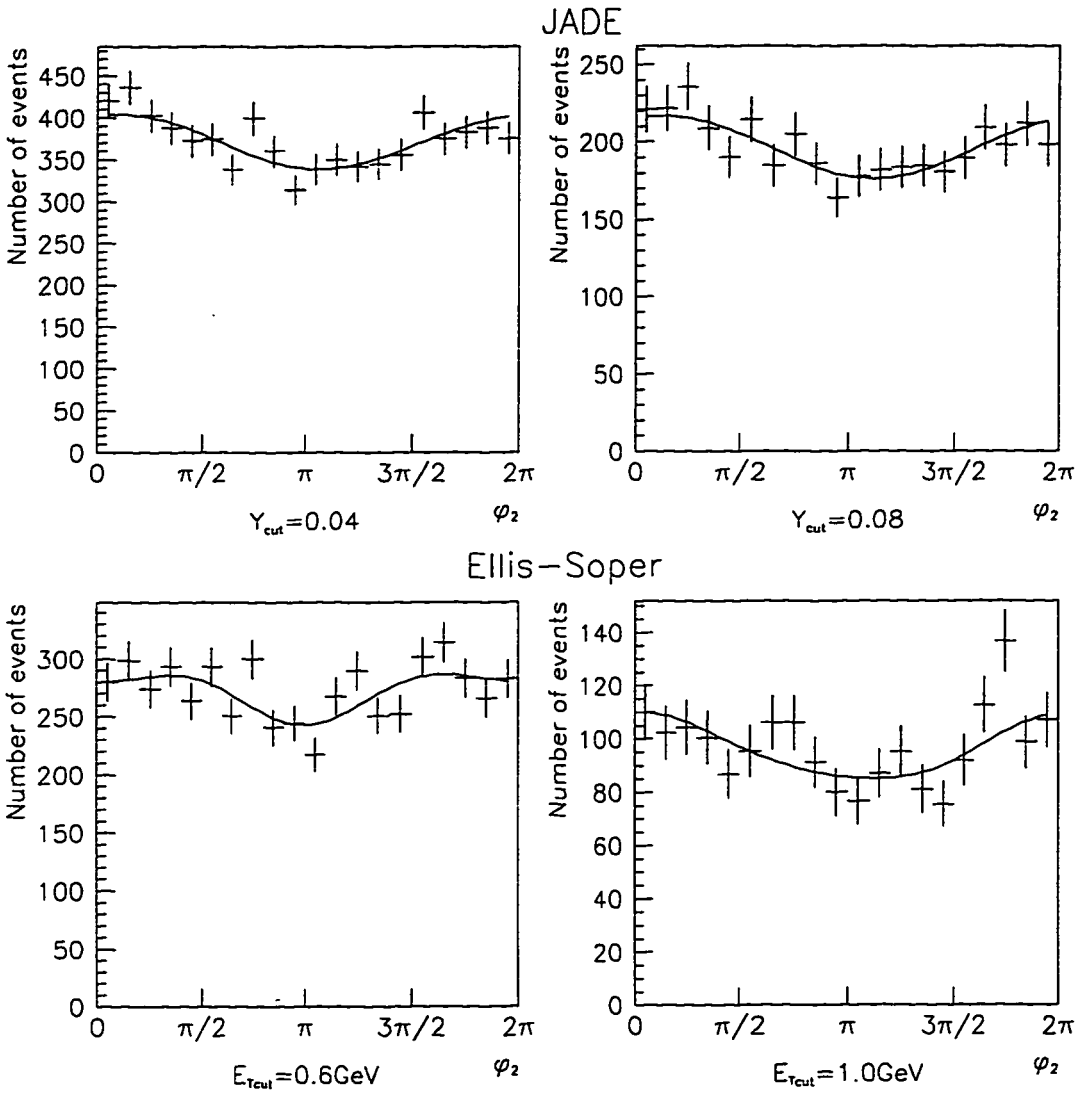

Figure 6.25: The corrected azimuthal distribution ϕ_2 of the less energetic jet in 2-jet events.

function of the form

$$\frac{d\sigma}{dx\,dy\,dz dP_T^2\,d\phi} = f(\phi) = A + B cos\phi + C cos2\phi + D sin\phi. \qquad (6.1)$$

The terms A through D are related to the absorption cross sections of longitudinal and transverse virtual photons [50]. The $cos\phi$ term arises from the real part of the longitudinal-transverse interference, while the $sin\phi$ term arises from the imaginary part. The right-left interference causes the $cos2\phi$ term. Using Eq. 6.1 we have

$$\langle cos\phi \rangle = \frac{\int f(\phi) cos\phi\, d\phi}{\int f(\phi)\, d\phi} = \frac{B}{2A}.$$

The results are shown in Table 6.2.

Table 6.2: $\frac{B}{2A}$ obtained from the fits of data shown in Figure 6.24 and 6.25.

Algorithm	Cuts	$\langle cos\phi_1 \rangle$	$\langle cos\phi_2 \rangle$
JADE	$Y_{cut} = 0.04$	-0.030 ± 0.008	0.043 ± 0.008
	$Y_{cut} = 0.08$	-0.028 ± 0.011	0.047 ± 0.011
Ellis-Soper	$E_{Tcut} = 0.6\,GeV$	-0.025 ± 0.009	0.034 ± 0.009
$(R^2 = 2)$	$E_{Tcut} = 1.0\,GeV$	-0.027 ± 0.016	0.062 ± 0.016

We see that the $\langle cos\phi \rangle$ of the jets obtained from these two different algorithms are the same within errors. The final measured azimuthal asymmetry including all the uncertainties are shown in Table 6.3.

6.3.2 Theoretical Prediction of the Jet Azimuthal Asymmetry

Let us compare this result with the QCD prediction in more detail. Using empirical approximation, the transverse momentum of jet can represent the parton transverse momentum. In the first order QCD process $p+q \rightarrow p_a + p_b \rightarrow p_j + X$, we can measure

$$x_{Bj} = \frac{Q^2}{2P \cdot q} = \frac{Q^2}{2M\nu},$$
$$z_j = \frac{P \cdot P_j}{P \cdot q} = \frac{E_{j(lab)}}{\nu},$$

Table 6.3: Final $\langle cos\phi_1 \rangle$ and $\langle cos\phi_2 \rangle$ with systematic and statistical uncertainties.

JADE	$Y_{cut} = 0.04$	$\langle cos\phi_1 \rangle = -0.030 \pm 0.008(stat) \pm 0.001(sys)$ $\langle cos\phi_2 \rangle = 0.043 \pm 0.008(stat) \pm 0.002(sys)$
	$Y_{cut} = 0.08$	$\langle cos\phi_1 \rangle = 0.028 \pm 0.011(stat) \pm 0.001(sys)$ $\langle cos\phi_2 \rangle = 0.047 \pm 0.011(stat) \pm 0.002(sys)$
Ellis-Soper	$E_{Tcut} = 0.6\,GeV$ $R^2 = 2$	$\langle cos\phi_1 \rangle = -0.025 \pm 0.009(stat) \pm 0.002(sys)$ $\langle cos\phi_2 \rangle = 0.034 \pm 0.009(stat) \pm 0.003(sys)$
	$E_{Tcut} = 1\,GeV$ $R^2 = 2$	$\langle cos\phi_1 \rangle = -0.027 \pm 0.016(stat) \pm 0.002(sys)$ $\langle cos\phi_2 \rangle = 0.062 \pm 0.016(stat) \pm 0.005(sys)$

while the corresponding parton variables in the calculations are

$$\begin{aligned} x &= \frac{Q^2}{2p \cdot q}, \\ z &= \frac{p \cdot p_a}{p \cdot q}. \end{aligned}$$

The relations between these variables are

$$\begin{aligned} x &= \frac{x_{Bj}}{\xi}, \\ z &= z_j - \frac{2x}{Q^2}\vec{K}_T \cdot \vec{P}_j, \end{aligned}$$

where $\vec{K}_T$ is the intrinsic transverse momentum of the struck quark. If K_T is neglected[5] $z_j = z$.

As we discussed in Chapter 2, for first order QCD events,

$$\langle cos\phi \rangle = \frac{\int d\sigma^{(1)} cos\phi}{\int d\sigma^{(1)}} \tag{6.2}$$

$$\int d\sigma^{(1)} cos\phi = \frac{8\alpha_s\alpha^2}{3Q^2}\frac{(2-y)\sqrt{1-y}}{y}\int_{x_{Bj}}^1 \frac{dx}{x}\sum_j Q_j^2(A_j + B_j + C_j), \tag{6.3a}$$

$$\int d\sigma^{(1)} = \frac{4\alpha_s\alpha^2}{3Q^2}\frac{1}{y}\int_{x_{Bj}}^1 \frac{dx}{x}\sum_j Q_j^2(A'_j + B'_j + C'_j), \tag{6.3b}$$

[5] As long as $x\vec{K}_T \cdot \vec{P}_j \ll Q^2$, the approximation used in this section is good.

where[6]

$$
\begin{aligned}
A_j &= A(x,z)F_j(\frac{x_{Bj}}{x},Q^2)D_j(\frac{z_H}{z},Q^2),\\
B_j &= B(x,z)F_j(\frac{x_{Bj}}{x},Q^2)D_j(\frac{z_H}{z},Q^2),\\
C_j &= C(x,z)F_j(\frac{x_{Bj}}{x},Q^2)D_j(\frac{z_H}{z},Q^2),\\
A'_j &= A'(x,y,z)F_j(\frac{x_{Bj}}{x},Q^2)D_j(\frac{z_H}{z},Q^2),\\
B'_j &= B'(x,y,z)F_j(\frac{x_{Bj}}{x},Q^2)D_j(\frac{z_H}{z},Q^2),\\
C'_j &= C'(x,y,z)F_j(\frac{x_{Bj}}{x},Q^2)D_j(\frac{z_H}{z},Q^2).
\end{aligned}
$$

By forming hadronic jets, we are summing over the contributions of all the hadrons in the jets. Namely, we can simplify the fragmentation function D. So for jet j, we have

$$\int_{z_H}^1 \frac{dz}{z} D(\frac{z_H}{z},Q^2)\mathcal{F}(x,y,z,Q^2) \longrightarrow \mathcal{F}(x,y,z_j,Q^2).$$

So the expression of $\langle cos\phi \rangle$ has A, B, C in the numerator and A', B', C' in the denominator. When x is not too small, the quark distribution functions are much larger than the gluon distribution function, so C and C' can be neglected. On the other hand, C can be either positive or negative, so its contribution to the integral is much smaller.

Let us see how the coefficients A, B, A' and B' behave. Figure 6.26 plots A, B, A' and B' and their dependences on x and z. Clearly, we expect an asymmetry in the jet ϕ distribution. A is negative and B is positive. But for larger values of z, $|A| > B$ and it produces a negative asymmetry. Figure 6.27 plots $A+B$ and $A'+B'$ and their dependences on x and z. $A+B$ is negative at high z and positive at low z.

From Eq. 2.4 we obtain $B(z) = -A(1-z)$. Therefore, we expect $A+B<0$ for $z > 0.5$ so $\langle cos\phi \rangle > 0$ while for $z < 0.5$, $A+B > 0$, so $\langle cos\phi \rangle < 0$. Further, from Figure 6.27 we note that $A'+B'$ increases rapidly as $z \to 1$ or 0. Therefore, even though $|A+B|$ increases as $z \to 1$ or 0, the asymmetry does not peak at $z = 1$ or 0.

Note again, $z = z_j$ is the fractional energy carried by the jet. Just as we discussed, we observe that the jet with larger energy ($z > 0.5$ in a 2-jet event) has a negative $\langle cos\phi \rangle$ and the jet with smaller energy ($z < 0.5$) has a positive $\langle cos\phi \rangle$. From the plot

[6] See Eqs. 2.4 and 2.17.

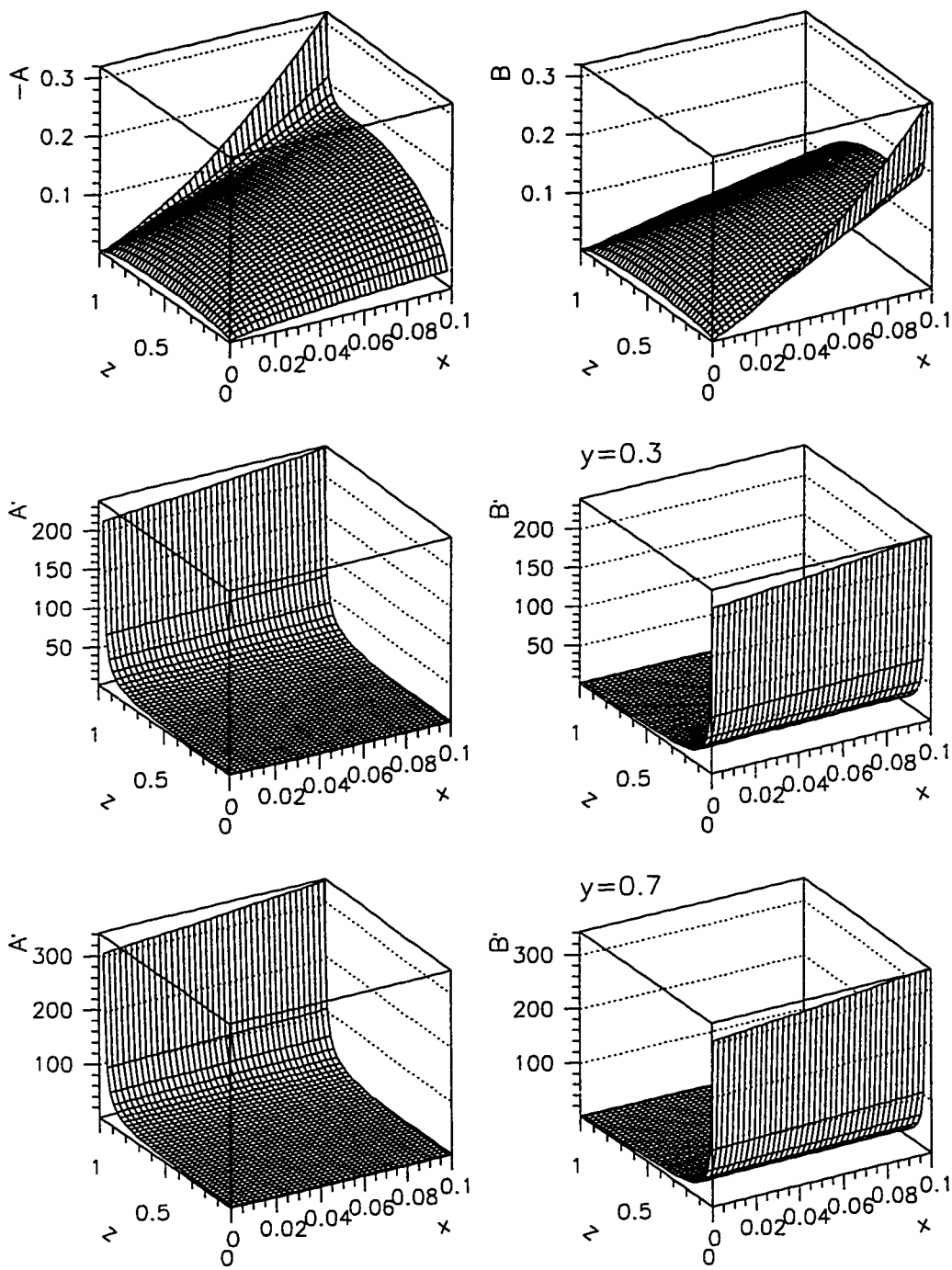

Figure 6.26: The x and z dependence of A, B, A' and B'.

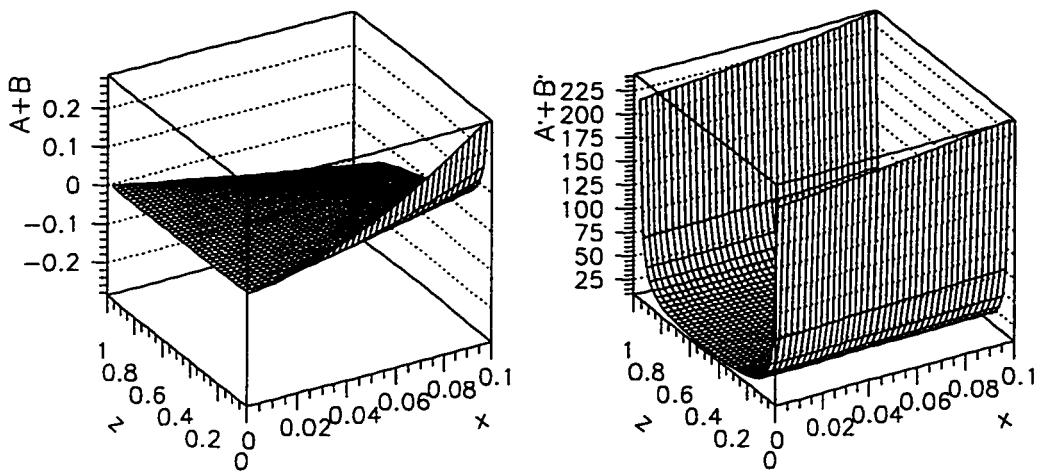

Figure 6.27: $A + B$ and $A' + B'$ and their x, z dependences.

of $\langle cos\phi \rangle$ vs. z, Figure 6.28[7], we see a significant z dependence of the asymmetry. $\langle cos\phi \rangle$ goes from positive to negative as z goes from 0 to 1, consistent with the above arguments.

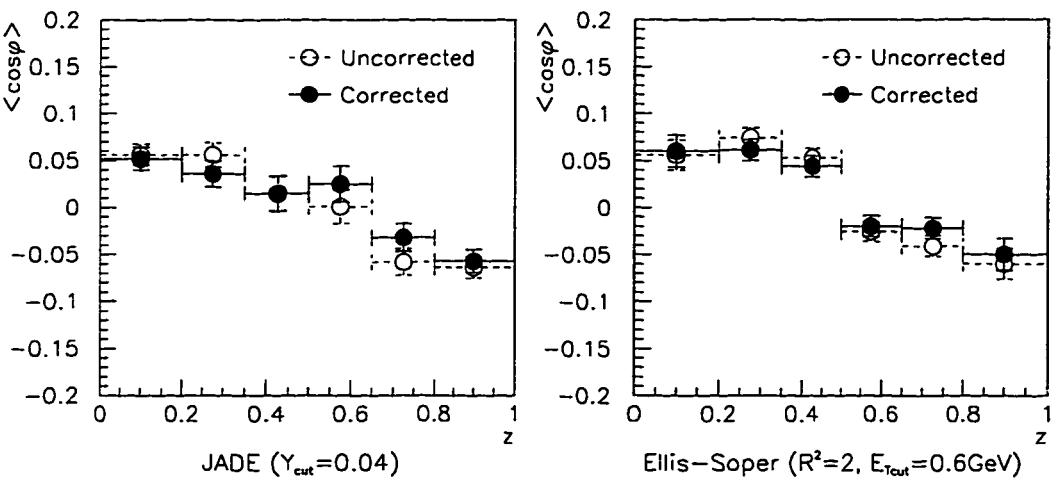

Figure 6.28: The z dependence of jet $\langle cos\phi \rangle$ in 2-jet events.

We conclude that the jet azimuthal distribution has a simpler relation with the corresponding parton distribution than the hadron azimuthal distribution does. The

[7] Here z is computed as E/E_{total}, where E is the energy of a jet and E_{total} is the total energy observed in the two jets.

qualitative behavior of the azimuthal asymmetry can be easily extracted in the theoretical calculation to compare with the experimental observation. We observe that the jet azimuthal asymmetry depends on the fractional energy carried by the jet. $\langle cos\phi \rangle > 0$ for jets with larger energy and $\langle cos\phi \rangle > 0$ for jets with smaller energy in 2-jet events. This is in good agreement with the perturbative QCD calculation.

6.3.3 Minimize the K_T effect

To minimize the K_T contribution, we can select events with small total transverse momentum. But first let us estimate how big is this intrinsic K_T.

Simple Estimation of K_T

The average K_T can be estimated by comparing the total transverse momentum in the Monte Carlo data with the measured value. To conserve momentum, the transverse momentum before the collision (the intrinsic transverse momentum K_T) and after (the total transverse momentum of the final hadrons) must be the same.

The E665 Monte Carlo physics generator assumes for the K_y and K_z distributions two independent Gaussians of the form[8] $G(x) \propto e^{-\frac{x^2}{\sigma^2}}$ both having width $\sigma = 0.44\,GeV$ (Lepto variable PARL(3)). $K_T = |\vec{K_T}| = \sqrt{K_y^2 + K_z^2}$ should have the distribution

$$\begin{aligned} f(K_T) = \frac{dN}{dK_T} &= \int_{-\infty}^{\infty} dK_y G(K_y) G(K_z(K_T, K_y)) \left| \mathcal{J}_{K_z}^{K_T} \right| \\ &\propto \frac{K_T}{\sigma^2} e^{-\frac{K_T^2}{\sigma^2}}, \end{aligned} \tag{6.4}$$

where $\mathcal{J}_{K_z}^{K_T} = \frac{\partial K_z(K_T, K_y)}{\partial K_T}$ is the Jacobian. This leads to

$$\langle K_T^2 \rangle = \sigma^2, \tag{6.5}$$

$$\langle K_T \rangle = \frac{\sqrt{\pi}}{2}\sigma. \tag{6.6}$$

Figure 6.29 shows the distribution of $\sqrt{K_y^2 + K_z^2}$ in our MC data. The histogram in this figure is the MC input and the solid line is a fit to Eq. 6.4. The fit gives $\sigma = 0.4300 \pm 0.0006\,GeV$ which is slightly different from the input of $0.44\,GeV$. However, these events have survived various experiment cuts.

---

[8] The standard Gaussian distribution function is given by $G(x) = \frac{1}{\sqrt{2\pi}\sigma} e^{-\frac{x^2}{2\sigma^2}}$

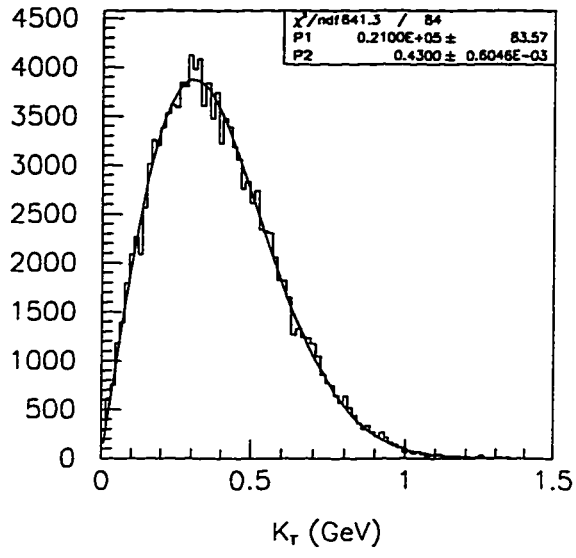

Figure 6.29: Monte Carlo input for the K_T distribution. P1 and P2 are fit parameters to $f(K_T) = P1 K_T e^{-\frac{K_T^2}{P2^2}}$. P1 is a normalization factor and P2 = σ.

If we assume that the real K_T is also a two-dimensional Gaussian distribution given by Eq. 6.4, and our Monte Carlo produces an accurate simulation for the detectors, we can estimate the value of K_T by comparing the transverse momentum distribution in the Monte Carlo data with the experimental data. Since momentum must be conserved, the total P_T is just K_T plus some missing transverse momenta. Assuming the transverse momentum distribution due to fragmentation is also Gaussian, we can fit the p_T distribution of the individual detected particles (Figure 6.30). By doing this we obtain $\sigma = 0.3665 \pm 0.0033\, GeV$ for the experimental data and $\sigma_{MC} = 0.3981 \pm 0.0034\, GeV$ for the Monte Carlo data.

We define the total transverse momentum in an event $P_{Ttotal} = |\sum \vec{p}_T|$. The same fit to the distributions of the P_{Ttotal} is plotted in Figure 6.31. The Gaussian widths for the P_{Ttotal} are $\sigma_{tot} = 0.686 \pm 0.014\, GeV$ for the experimental data and $\sigma_{totMC} = 0.6335 \pm 0.0094\, GeV$ for the Monte Carlo data. The Monte Carlo input for K_T is $\sigma_{K_TMC} = 0.4300 \pm 0.0006\, GeV$ as shown in Figure 6.29. We can estimate the real K_T by using:

$$\begin{aligned} \sigma^2_{K_TMC} + N_{miss}\sigma^2_{MC} &= \sigma^2_{totMC}, \\ \sigma^2_{K_T} + N_{miss}\sigma^2 &= \sigma^2_{tot}, \end{aligned}$$

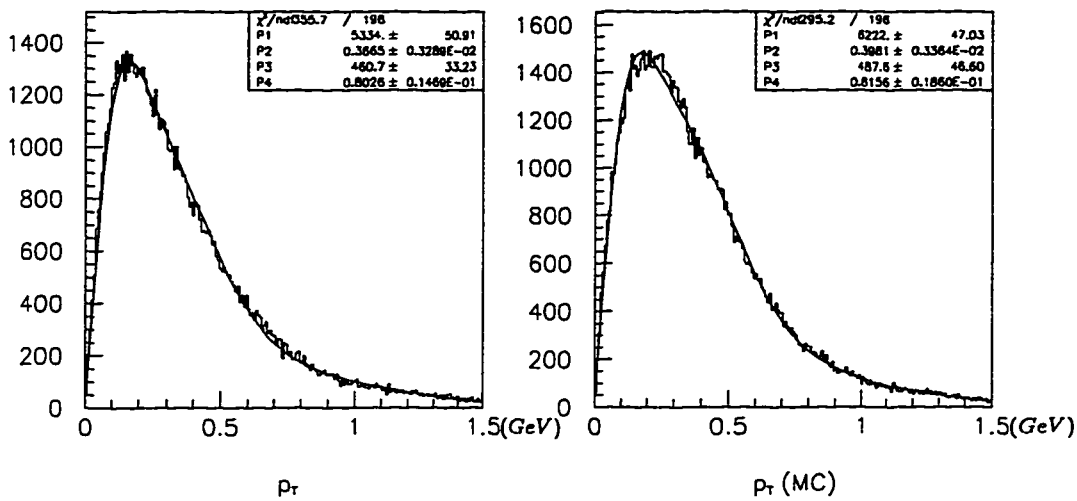

Figure 6.30: The p_T distributions of the individual final particles (each particle is one entry). The curves are fit to a sum of two 2-dimensional Gaussians. P2 and P4 are the widths of the two Gaussians and P1 and P3 are the normalization factors.

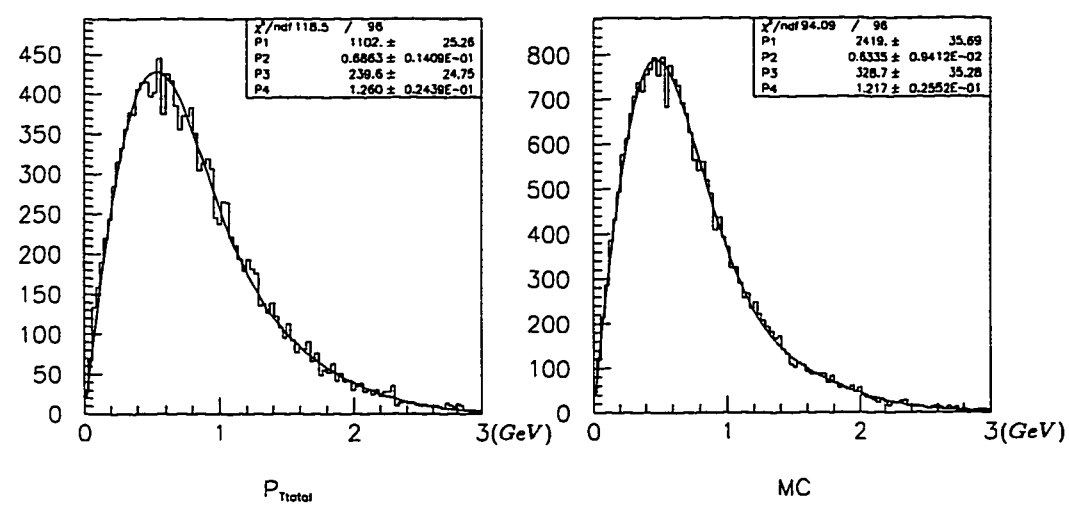

Figure 6.31: The P_{Ttotal} distributions (each event has one entry). fit to a sum of two 2-dimensional Gaussians. P2 and P4 are the widths of the two Gaussians and P1 and P3 are the normalization factors.

where N_{miss} is the average number of the missing particles in an event. The result is

$$\sigma_{K_T} = 0.536^{+0.032}_{-0.027} GeV.$$

This is in excellent agreement with the result obtained by J. Conrad [45] by using earlier E665 data: $\langle K_T^2 \rangle = 0.27 \pm 0.04 GeV^2$.

Azimuthal asymmetry with smaller K_T

Since the asymmetry introduced by the intrinsic transverse momentum derived by Cahn (see reference [20]) is proportional to K_T/Q, we can select events with the total transverse momentum $|\sum \vec{p}_T|/Q < 0.3$ to effectively minimize this K_T contribution. The distribution of $|\sum \vec{p}_T|/Q$ for all events is plotted in Figure 6.32.

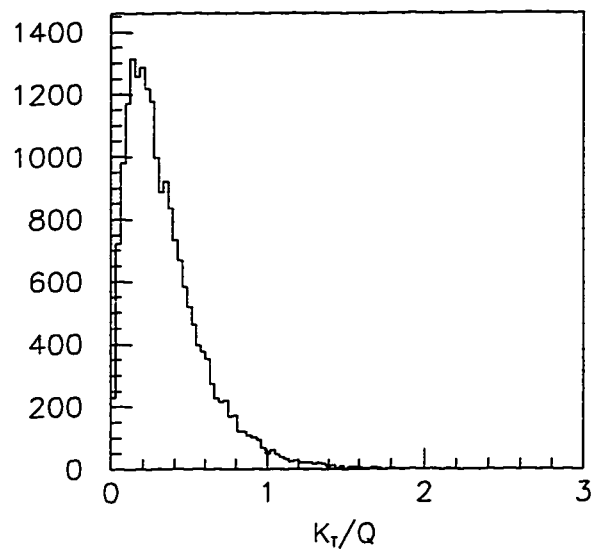

Figure 6.32: The distribution of K_T/Q, where $\vec{K}_T$ is estimated as $\sum \vec{p}_T$ in an event.

At the same time, the difference between the parton z and the jet z_j, $2x\vec{K}_T \cdot \vec{P}_j/Q^2$, will be small. Thus the jets are able to represent partons more accurately. The ϕ distributions of the smaller K_T events are plotted in Figure 6.33 and 6.34.

We have fit the distributions to the function in Eq. 6.1. From the values of B and A obtained in the fit, we can calculate $\langle cos\phi \rangle = B/2A$. The results are summarized in Table 6.4.

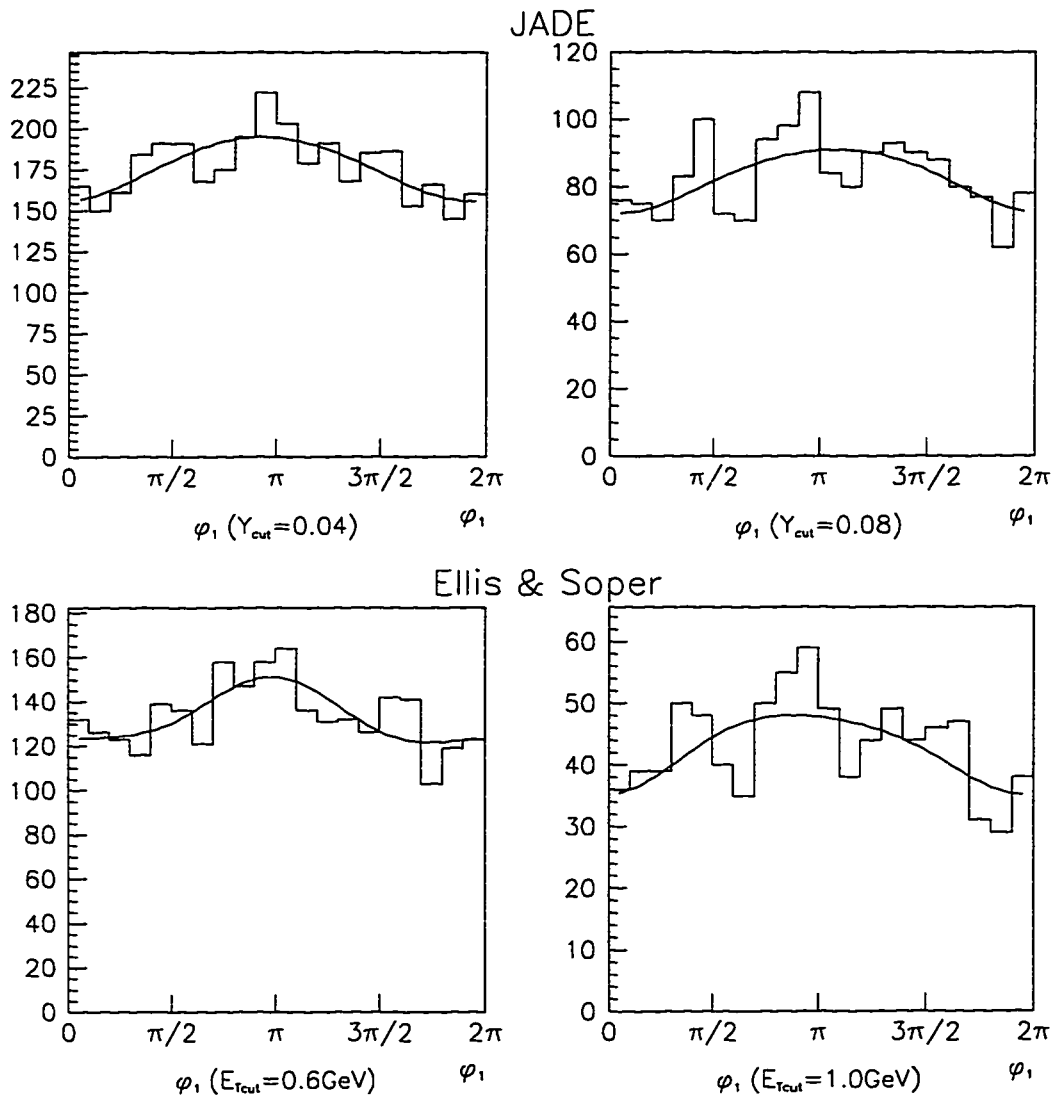

Figure 6.33: The corrected azimuthal distribution ϕ_1 of the more energetic jet in 2-jet events with $K_T/Q < 0.3$, where $\vec{K}_T$ is estimated as $\sum \vec{p}_T$ in an event.

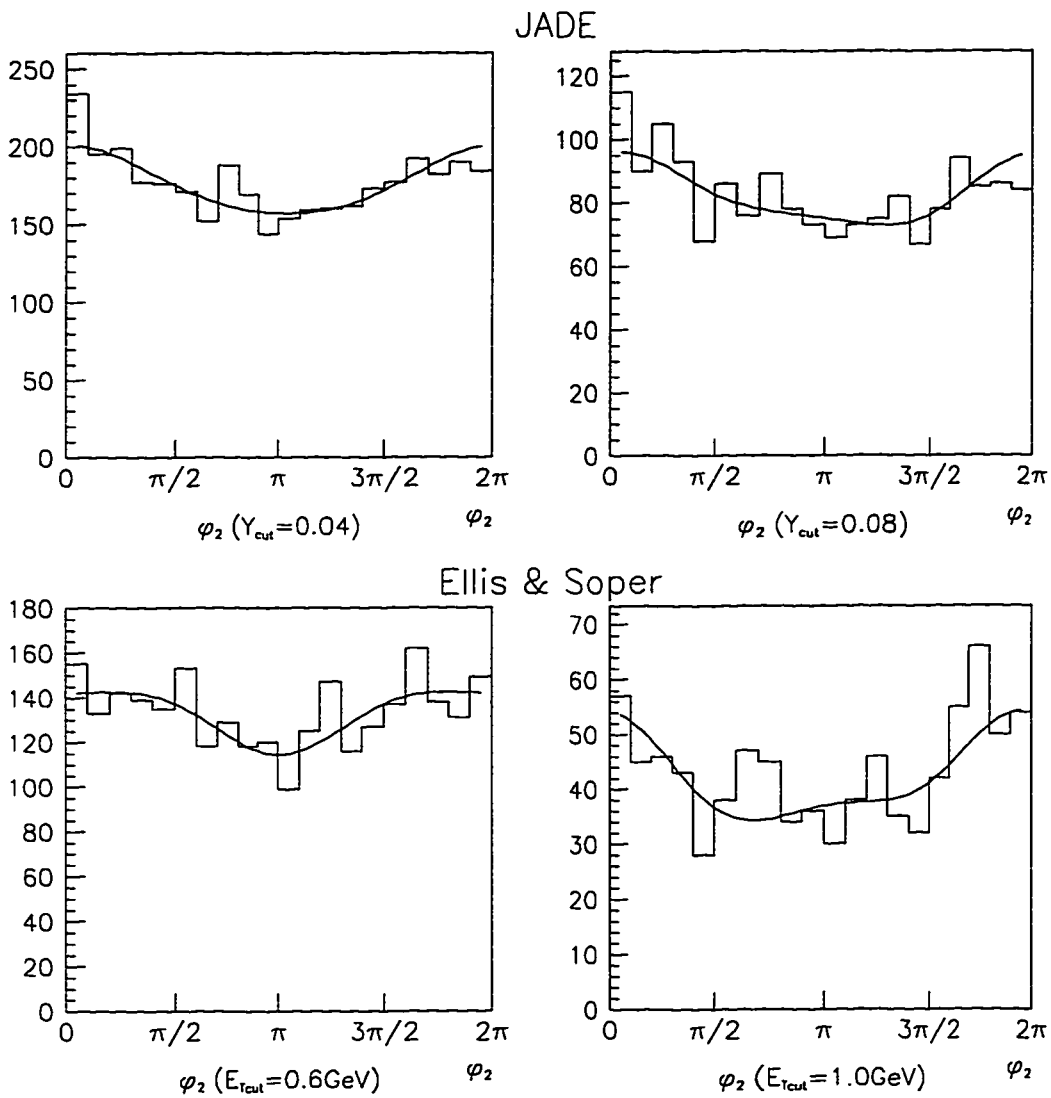

Figure 6.34: The corrected azimuthal distribution ϕ_2 of the less energetic jet in 2-jet events with $K_T/Q < 0.3$, where $\vec{K}_T$ is estimated as $\sum \vec{p}_T$ in an event.

Table 6.4: $\langle cos\phi \rangle$ obtained for $|\sum \vec{p}_T|/Q < 0.3$ data.

Algorithm	Cuts	$\langle cos\phi_1 \rangle$	$\langle cos\phi_2 \rangle$
JADE	$Y_{cut} = 0.04$	-0.054 ± 0.012	0.061 ± 0.012
	$Y_{cut} = 0.08$	-0.056 ± 0.017	0.063 ± 0.018
Ellis-Soper	$E_{T cut} = 0.6\,GeV$	-0.052 ± 0.014	0.052 ± 0.014
$(R^2 = 2)$	$E_{T cut} = 1.0\,GeV$	-0.074 ± 0.024	0.102 ± 0.040

The algorithms give values which agree very well. Although the statistics are low for the small K_T events, we observe a slight increase in the asymmetry. This is very interesting and worth further investigation.

6.4 Azimuthal Asymmetry of Final State Hadrons

The asymmetry is also reflected in the z_H dependence of the hadron ϕ distribution, where z_H is the fractional energy carried by the hadron. This is understandable since a hadron with large z_H is more likely formed from the hadronization of a parton with larger z. As shown in the hadron azimuthal distribution in Figure 6.35, the ϕ distribution is quite flat when $z_H < 0.2$. The asymmetry increases with z_H, although at $z_H > 0.8$ the asymmetry is not clear due to the low statistics. This phenomenon has been investigated in many other publications as we mentioned in Chapter 2.

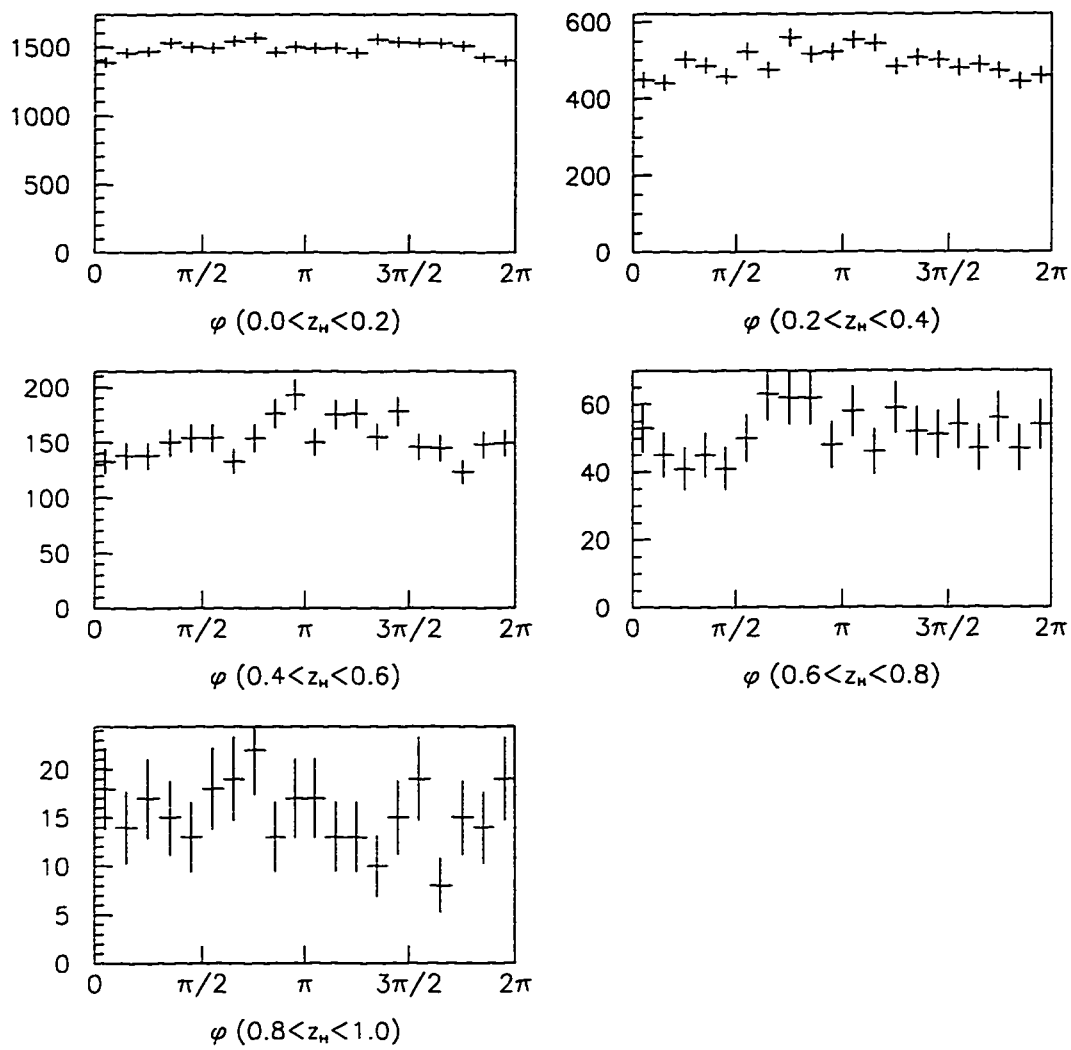

Figure 6.35: The uncorrected semi-inclusive azimuthal hadron distribution for various z_H ranges.

Chapter 7

CONCLUSIONS

In summary, the jet transverse momentum distribution is a good representation of the underlying parton transverse momentum distribution. Jet azimuthal asymmetry can be predicted in first order QCD calculations. Measuring the jet azimuthal asymmetry in events with two forward jets provides a test of perturbative QCD. Such an experimental study has not been performed in the past.

In this thesis, we examined the final hadronic jets in muon Deep Inelastic Scattering events in order to help us understand the dynamics of the partons within the nucleon. The data were collected during run 91 of the experiment E665 at Fermilab. The azimuthal angle between the jet and the leptonic plane in the center of mass frame of the 2-jet events is measured. An asymmetry is observed for the jet azimuthal distribution. This asymmetry has a strong dependence on the fractional energy of the jet. This is in good agreement with perturbative QCD calculations.

Different jet algorithms as well as their ability to reproduce the parton characteristics were studied extensively by using the E665 Monte Carlo data. The results demonstrate that the modified JADE and the new algorithm designed by Ellis and Soper can reveal the jet structure in lepton deep inelastic scattering experiments at moderate center of mass energy. These two algorithms were used in our experimental data analysis. For experiments with higher energy, the Ellis-Soper algorithm allows cleaner 2-jet events to be identified and thus help us to better understand the first order QCD process. With higher E_{Tcut}, this new algorithm can successfully suppress the contribution of the soft interactions. It can also be used to identify multiple jets in events with higher order QCD hard interactions.

In an independent analysis, we have estimated that the intrinsic transverse momentum in the nucleon is $\langle K_T^2 \rangle = 0.536^{+0.032}_{-0.027}\, GeV$. This intrinsic transverse momentum has also an affect on the jet azimuthal distributions.

In conclusion, the jet data from Experiment E665 is consistent with the perturbative QCD prediction for azimuthal asymmetry. We expect our current understanding regarding jet distributions, jet algorithms and intrinsic transverse momentum will be

further clarified by future experiments which have more data and higher center of mass energy, for example, at HERA.

BIBLIOGRAPHY

[1] C.M. Hoffman it et al., "High-Energy Muon Inelastic Scattering", Physical Review Letters, 22, pp659, March 1969.

[2] B.D. Bieterle *et al.*, "Muon-proton Inelastic Scattering, $|q^2|$ less than 1.2 $(GeV/c)^2$", Physical Review Letters, 23, pp1187, Nov. 1969.

[3] Landau and Lifshitz, "Quantum Electrodynamics - Course of Theoretical Physics 4", 1982.

[4] D. Perkins, "Introduction to High Energy Physics", pp32.

[5] "Lepton & Quark Full Listings", Physical Review, D50, pp1397, Aug. 1st. 1994.

[6] W.K.H. Panofsky, "Low q^2 electrodynamics, elastic and inelastic electron (and muon) scattering", International Conference on High-Energy Physics, 14th, Vienna 1968.

[7] M. Breidenbach it et al., "Observed Behavior of Highly Inelastic Electron-Proton Scattering" Physical Review Letters, 23, pp935, October 1969.

[8] J.D. Bjorken, "Asymptotic Sum Rules at Infinite Momentum" Physical Review, 179, pp1547, March 1969.

[9] R.P. Feynman, "Very High-Energy Collisions of Hadrons" Physical Review Letters, 23, pp1415, December 1969.

[10] R.L. Jaffe, "Deep Inelastic Scattering with application to Nuclear Targets", Los Alamos workshop on Relativistic Dynamics and Quark-Nuclear Physics, 1985.

[11] J. Kuti and V.F. Weisskopf, "Inelastic Lepton-Nucleon Scattering and Lepton Pair Production in the Relativistic Quark-Parton Model" Physical Review D4, pp3418, 1971.

[12] C.G. Callan and D.J. Gross, "High-energy Electroproduction and the Constitution of The Electric Current", Physical Review Letters, 22, pp156, January 1969.

[13] E.M. Riodan *et al.* SLAC-PUB-1634, 1975.

[14] G. 't Hooft, "Renormalization of Massless Yang-Mills Fields", Nuclear Physics B33, pp173, 1971.

[15] G. 't Hooft, "Renormalizable Lagrangians for Massive Yang-Mills Fields", Nuclear Physics B35, pp167, 1971.

[16] G. 't Hooft, "Regularization and Renormalization of Gauge Fields", Nuclear Physics B44, pp189, 1972.

[17] D.J. Gross and F.A. Wilczek, "Ultraviolet Behavior of Non-Abelian Gauge Theories", Physical Review Letters, 30, pp1343, 1973.

[18] H.D. Politzer, "Reliable Perturbative Results for Strong Interactions?", Physical Review Letters, 30, pp1346, 1973.

[19] H. Georgi and H.D. Politzer, "Clean Tests of Quantum Chromodynamics in μp Scattering", Physical Review Letters, 40, pp3, 1978.

[20] R.N. Cahn, "Azimuthal Dependence in Leptoproduction: A Simple Parton Model Calculation", Physics Letters, 78B, pp269, 1978.

[21] R.N. Cahn, "Critique of Parton-model Calculations of Azimuthal Dependence in Leptoproduction", Physics Review, D40, pp3170, 1989.

[22] J. Chay, S. D. Ellis, and W. J. Stirling, "Azimuthal asymmetry in lepton-proton scattering at high energies", Physical Review, D45, pp46, Jan. 1992.

[23] M. Arneodo *et al.*, "Measurement of Hadron Azimuthal Distributions in Deep Inelastic Muon Proton Scattering", Zeitzchrift Für Physik C34, pp277, 1987.

[24] D. M. Jansen, Doctoral dissertaion "Transverse Momentum and the Energy Flow of Charged Hadrons Produced in 490 GeV/c Deep Inelastic Muon Scattering", 1991.

[25] M. D. Baker, Doctoral dissertaion "Azimuthal Asymmetry and Transverse Momentum of Hadrons in Deep Inelastic Muon Scattering at 490 GeV", Dec. 1992.

[26] S.D. Drell, D.J. Levy, and T.M. Yan, "Theory of Deep-Inelastic Lepton-Nucleon Scattering and Lepton-Pair Annihilation Processes. I", Physical Review, 187, pp2159, 1969.

[27] V. Hedberg, G. Ingelman, C. Jacobsson and L. Jonsson, "Study of Jet Reconstruction Algorithms for deep-inelastic events at HERA", Zeitzchrift Für Physik C63, pp49, 1994

[28] G. Thompson, N.A. McCubbin, J.V. Morris and D.P.C. Sankey "Jet Finding in the Breit frame", Journal of Physics, G19, no.10, pp1575, 1993.

[29] G. Ingelman, LEPTO — The Lund Monte Carlo for Deep Inelastic Lepton-Nucleon Scattering.

[30] T. Sjöstrand, JETSET Physics and Manual,

[31] H. Georgi and J. Sheiman, "Transverse-momentum distributions in lepton-hadron scattering from quantum chromodynamics", Phsical Review D20, pp20, 1979.

[32] G. Hanson *et al.*, "Evidence for Jet Structure in Hadron Production by e^+e^- Annihilation", Physical Review Letters, 35, pp1609, 1975.

[33] W. Bartel *et al.*, JADE Collaboration, Zeitzchrift Für Physik C33, pp23, 1986.

[34] Hermann Hessling, "On particle-like jets", DESY 95-069, eprint hep-th/9504297, 1995.

[35] S. Catani it et al., "New clustering algorithm for multijet cross sections in e^+e^- annihilation" Physics Letter B269, pp432, 1991.

[36] S. Catani it et al., "The $k_\perp$-clustering algorithm for jets in deep inelastic scattering and hadron collisions.", Physics Letter B285, pp291, 1992.

[37] S. D. Ellis, D. E. Soper, "Successive combination jet algorithm for hadron collisions", Physics Review, D48, pp3160, 1993.

[38] S. D. Ellis, J. Huth, N. Wainer, K. Meier, N. Hadley, D. Soper, and M. Greco, "Research Directions for the Decode", Proceedings of the Summer Study, Snowmass, Colorado, 1990.

[39] L. Lönnblad, Zeitzchrift Für Physik C58, pp471, 1993.

[40] M. Bengtsson, T. Sjöstrand, Zeitzchrift Für Physik C37, pp465, 1988.

[41] L3 Collaboration, "Studies of Events Structure and Comparisons with QCD Models at the Z0 Resonance", CERN-PPE/92-50, 1992.

[42] B. Andersson and G. Gustafson, Zeitzchrift Für Physik C3, pp223, 1980.

[43] A. Malensek and J.G. Morfin, "The Tevatron Muon Beam: a High Intensity Beam with Well-Defined Polarization", Fermilab Technical Report TM 1193 2966.0, July 1983.

[44] M.R. Adams et. al. (E665), "A Spectrometer for Muon Scattering at the Tevatron", Nuclear Instruments and Methods in Physics Research A291, 1990.

[45] J. Conrad, Doctoral dissertation, "A Study of the Q2 Dependence of the QCD Coupling Constant from the Transverse Momentum of Jets in Deep Inelastic Muon Scattering", pp72, 1992.

[46] A. Kotwal, Doctoral dissertation "Proton and Deuteron Structure Functions in Muon Scattering at 470 GeV", 1995.

[47] A. Kotwal, "Preliminary RUN90 calorimeter calibration using electron beam data", E665 memo AN181, March 1993.

[48] "Meson Full Listings", Physical Review, D50, pp1534, Aug. 1994.

[49] "Quantum Chromodynamics", Physical Review, D50, pp1298, Aug. 1994.

[50] A. Mendez, "QCD Predictions for Semi-Inclusive and Inclusive Leptoproduction", Nuclear Physics B145, pp199, 1978.

[51] S. Wolbers, "The E665 Energy Scale", E665 memo AN227, Sep. 1996.

[52] J. Ryan, Doctoral dissertation "Particles Production in Deep Inelastic Muon Scattering", Feb. 1991.

[53] P. N. Harriman, A. D. Martin, R. G. Roberts and W. J. Stirling, "Parton distributions extracted from data on deep-inelastic lepton scattering, prompt photon production and the Drell-Yan process", Physical Review D42, pp798, Aug. 1990.

Appendix A

E665 COLLABORATION - 90/91

T. Dreyer, M. Erdmann, J. Haas, M. Lenski, W. Mohr, G. Seigert, H.E. Stier, M. Wilhelm
Albert-Ludwigs-Universität Freiburg i. Br., Germany

D.F. Geesaman, H.E. Jackson, S. Kaufman,
T. Kirk, V. Papavassiliou, D. Potterveld, A. Zghiche
Argonne National Laboratory, Argonne IL USA

R.D. Kennedy, H.G.E. Kobrak, P. Madden, A. Salvarani, R.A. Swanson
University of California, San Diego, CA USA

E. Kinney
University of Colorado, Boulder, CO USA

B.R. Baller, J. Hanlon, H. Melanson,
H.E. Montgomery, J.G. Morfin, C. Salgado, S.A. Wolbers
Fermi National Accelerator Laboratory, Batavia, IL USA

J.M. Conrad, G.Y. Fang, A.V. Kotwal, D.G. Michael,
R.B. Nickerson, F.M. Pipkin, M.H. Schmitt, Richard Wilson
Harvard University, Cambridge, MA USA

M.R. Adams, D.A. Averill, T.J. Carroll, R.S. Guo,
C. Halliwell, D.E. Jaffe, S.R. Magill, D.W. Mcleod, T. McKibben
University of Illinois, Chicago, IL USA

A. Eskreys, J. Figiel, K. Olkiewicz, B. Pawlik, P. Stopa
Institute for Nuclear Physics, Krakow, Poland

P.L. Anthony, F.S. Dietrich
Lawrence Livermore National Laboratory, Livermore, CA USA

S. Aïd, S. Kunori, S. O'Day, E.J. Ramberg, A. Skuja, G.A. Snow
University of Maryland, College Park, MD USA

M.D. Baker, W. Busza, L. Osborne, J.J. Ryan
Massachusetts Institute of Technology, Cambridge, MA USA

I. Derado, V. Eckardt, H.J. Gebauer, D. Hantke, G. Jansco, A. Manz,
N. Schmitz, S. Soldner-Rembold, M. Vidal, W. Wittek
Max-Planck-Institut für Physik, Munich, Germany

H.M. Schellman, P. Spentzouris
Northwestern University, Evanston, IL USA

H.L. Clark, R.W. Finlay, K.H. Hicks
Ohio University, OH USA

A. Banerjee, K. A. Griffioen
University of Pennsylvania, Philadelphia PA USA

A.A. Bhatti, U. Bratzler, R. Davisson, W. Dougherty, D.M. Jansen,
Z. Jin, J.J. Lord, H.J. Lubatti, R.S. Perry, R. Wilkes, T. Zhao
University of Washington, Seattle, WA USA

H.M. Braun, H. Breidung, U. Ecker, R. Otten, A. Röser
University of Wuppertal, Wuppertal, Germany

S. K. Dhawan, V. Hughes, K.P. Schüler, H. Venkataramania
Yale University, New Haven, CT USA

VITA

Zhong Jin was born in Shanghai on May 31, 1969. She attended Fudan University from 1986 to 1990 where she majored in Physics. In January of 1990, she started her graduate studies at the University of Massachusetts at North Dartmouth. After receiving an M.S. in Physics in 1991, she entered the University of Washington where she obtained an M.S. in Physics (1994) and an M.S. in Electrical Engineering (1996).